

DISS. ETH NO. 19906

**New approaches towards understanding and forecasting induced
seismicity**

A dissertation submitted to

ETH ZURICH

for the degree of

Doctor of Sciences

presented by

CORINNE ELISABETH BACHMANN

dipl. natw. ETH

born 18.01.1982

citizen of

Zürich ZH and Feusisberg SZ

accepted on the recommendation of

Prof. Dr. Stefan Wiemer, examiner

Prof. Dr. Domenico Giardini, co-examiner

Dr. Jochen Woessner, co-examiner

Prof. Dr. Serge Shapiro, co-examiner

2011

Nothing will ever be attempted, if all possible objections must be first overcome.

– Samuel Johnson, *Rasselas*, 1759

Inhaltsverzeichnis

| | |
|--|------------|
| Zusammenfassung | IV |
| Summary | VII |
| 1 General Introduction | 1 |
| 1.1 EGS | 2 |
| 1.1.1 Basel | 6 |
| 1.1.2 Soultz-sous-Forêts | 7 |
| 1.2 Challenges of EGS | 9 |
| 1.2.1 ISHA | 9 |
| 1.2.2 Event-Size Distributions | 12 |
| 1.3 Quality Assessment of Seismic Networks | 12 |
| 1.4 Chapter Contents | 13 |
| References | 15 |
| 2 Statistical analysis of the induced Basel 2006 earthquake sequence: Introducing a probability-based monitoring approach for Enhanced Geothermal Systems | 19 |
| 2.1 Introduction | 21 |
| 2.2 Data | 27 |
| 2.3 Method | 30 |
| 2.3.1 Fitting the overall parameters of the sequence: b-values and duration | 30 |
| 2.3.2 Forecasting Models | 33 |
| 2.3.2.1 The Reasenberg & Jones model | 35 |
| 2.3.2.2 Epidemic Type Aftershock Models | 36 |
| 2.4 Modelling approaches | 37 |
| 2.4.1 Modelling results | 40 |
| 2.4.2 Performance evaluation | 41 |
| 2.4.3 Translating forecast rates to time-varying seismic hazard | 43 |
| 2.5 Discussion and Conclusion | 46 |

| | |
|---|------------|
| References | 55 |
| 3 Influence of pore pressure on the event size distribution of induced earthquakes | 61 |
| 3.1 Discussion | 62 |
| References | 76 |
| 4 Analysis of the Soultz-sous-Forêts seismicity induced by an injection test in 1993 | 81 |
| 4.1 Introduction | 83 |
| 4.2 Data | 84 |
| 4.2.1 Seismic Network | 84 |
| 4.2.2 Injections | 84 |
| 4.3 Analysis of the SSF Sequence | 89 |
| 4.3.1 Statistical parameters of the SSF sequence | 89 |
| 4.3.2 Forecasting of the seismicity rate | 95 |
| 4.3.2.1 ETAS and Shapiro Model | 95 |
| 4.3.2.2 Performance Evaluation | 97 |
| 4.3.2.3 Hazard Integration | 100 |
| 4.3.3 Seismogenic Index | 100 |
| 4.4 Conclusions | 102 |
| References | 103 |
| 5 Reliability of the Probability-Based Magnitude of Completeness Method | 107 |
| 5.1 Introduction | 108 |
| 5.2 Data | 113 |
| 5.3 Method | 115 |
| 5.4 Results | 119 |
| 5.4.1 Station detection sensitivity distribution | 119 |
| 5.4.2 Sensitivity to P and p_t | 121 |
| 5.4.3 Data Analysis – Removing data from a independent subnetwork | 124 |
| 5.4.4 Probability-based magnitude of completeness for Northern California – Our choice | 124 |
| 5.5 Discussion and Conclusion | 128 |
| 5.6 Data and Resources | 130 |
| References | 130 |
| 6 Conclusions | 133 |
| 6.1 Summary of Results | 134 |
| 6.1.1 Statistical analysis of fluid induced seismicity | 134 |

INHALTSVERZEICHNIS

| | |
|---|------------|
| 6.1.2 Analysis of the probability-based magnitude of completeness method | 137 |
| 6.2 Future Perspectives | 138 |
| References | 141 |
| List of Tables | 144 |
| List of Figures | 144 |
| Acknowledgements | 153 |
| Curriculum Vitae | 155 |

Zusammenfassung

Mit Hilfe Erweiterter Geothermischer Systeme ("Enhanced Geothermal Systems", EGS) ist es möglich, geothermische Energie an Orten zu nutzen, welche keine natürlichen Heisswasser-Reservoire im Untergrund vorweisen. Dazu wird ein Fluid, normalerweise Wasser, unter hohem Druck in den kristallinen Untergrund gepresst um Klüfte zu verbinden und dadurch ein Reservoir zu erzeugen. Ziel dieses Vorgehens ist es, die Zirkulation des Fluids im Untergrund zu ermöglichen, womit Wärme extrahiert werden kann. Diese wird entweder als Fernwärme genutzt oder in Elektrizität umgewandelt. Dieser Vorgang verursacht eine Vielzahl kleiner Erdbeben, induzierte Seismizität genannt. Das Ziel dieser Arbeit ist es, die Vorgänge besser zu verstehen, welche zu dieser Seismizität führen.

Während eines EGS-Projektes wird die induzierte Seismizität aufgezeichnet und fortwährend analysiert. Die seismische Aktivität wird dabei von einem Alarmsystem überwacht, welches vorbestimmte Massnahmen beinhaltet. In dieser Arbeit werden neue Wege vorgestellt, die aufgezeichnete Aktivität zu interpretieren. Es wird aufgezeigt, dass für die Vorhersage induzierter Seismizität Modelle gebraucht werden können, welche zur Vorhersage von Nachbebensequenzen entwickelt wurden. Die Beben werden dabei in Pseudo-Echtzeit analysiert und die Modelle fortlaufend angepasst. Die Gültigkeit der Modelle wird mit statistischen Tests überprüft, welche für globale Seismizitätsmodelle entwickelt wurden. Das Ziel dieser Arbeit ist ein neues,

wahrscheinlichkeitsbasiertes Alarmsystem zu konstruieren. Dieses basiert auf Seismizitätsraten, welche von den angepassten Modellen vorausgesagt werden. Das beste Modell dabei ist ein zusammengesetztes Modell, für welches die beitragenden Modelle unterschiedlich gewichtet werden.

Um die Grössenverteilung von Erdbeben zu beschreiben wird das Gutenberg–Richter Gesetz benutzt; die Anzahl der Beben wird gegeben durch: $\log N = a - bM$. Ein hoher Wert von b bedeutet, dass in einer Sequenz verhältnismässig viele kleine Beben auftreten. Eine neue Methode zur Kartierung der räumlichen Verteilung der b -Werte zeigt auf, dass induzierte Seismizität eine grosse Zeit- und Raumabhängigkeit der b -Werte aufweist. Um diese Beobachtung zu erklären, wird ein Modell eingeführt, welches die Evolution des Porendruckes simuliert und die Magnitude der simulierten Erdbeben anhand einer umgekehrt-proportionalen Beziehung zwischen dem b -Wert und dem Spannungsunterschied bestimmt. Anhand dieses Modells kann gezeigt werden, dass die beobachteten b -Werte mit dem Porendruck zusammenhängen. Hohe Drucke korrelieren mit hohen b -Werten, da bevorzugt kleine Beben induziert werden. In grösserer Entfernung zum Injektionspunkt nimmt der Porendruck ab, und b -Werte in der Grössenordnung des regionalen Wertes werden beobachtet. Dies führt dazu, dass die Wahrscheinlichkeit eines Erdbebens grösserer Magnitude mit der Distanz zunimmt.

Für jede statistische Analyse eines seismischen Datensatzes ist es wichtig zu wissen bis zu welcher Magnitude dieser vollständig ist. Unterhalb des Magnitudenschwellenwertes M_c werden nicht mehr alle Erdbeben vollständig erfasst. Dieser Schwellenwert wird gewöhnlich anhand der Abweichung der beobachteten Erdbebenverteilung vom Gutenberg–Richter Gesetz bestimmt. Eine neuere Methode bestimmt M_c basierend auf den Eigenschaften der Stationen eines seismischen Netzwerks. Diese Arbeit untersucht den Einfluss von unabhängigen Netzwerken, welche ihre Daten in das Hauptnetzwerk einleiten aber nicht unter den gleichen Bedin-

gungen Erdbeben triggern, auf den Magnitudenschwellenwert. Um den Einfluss von vernachlässigbaren Wahrscheinlichkeiten zu ermitteln, wird ein neuer Grenzwert eingeführt, welcher den minimalen Anteil einer Station an der Gesamtwahrscheinlichkeit, ein Erdbeben zu detektieren, bestimmt. Dies schließt Stationen von der Berechnung aus, welche einen unerheblichen Beitrag zur Gesamtwahrscheinlichkeit leisten, womit die Berechnung deutlich effizienter und zuverlässiger wird. Anhand des Beispiels des Nordkalifornischen Seismischen Netzwerks wird der Einfluss dieser Änderungen diskutiert; zudem werden Karten für dieses Netzwerk vorgestellt, welche 1) die Verteilung des Magnitudenschwellenwertes und 2) die Wahrscheinlichkeit, ein Erdbeben der Magnitude 1 oder 3 zu detektieren, zeigen.

Summary

Enhanced geothermal systems (EGS) allow the use of geothermal energy in places where the permeability in the underground is too low and thus, no natural reservoir is available. By injecting fluid at high pressures, fractures can connect, leading to an increase in the permeability and thus the stimulation of a geothermal reservoir. The goal is the circulation of a fluid to extract heat, which can then be used for district heating or electricity production. The connection of the fractures is associated with microseismicity – so called induced seismicity. The main objective of this thesis is to better understand the processes associated with this type of seismicity.

The seismicity induced by an EGS project is monitored in real time by a dense seismic network; a pre-defined alarm system describes the actions that have to be taken according to the recorded activity. This study presents new ways to interpret this recorded seismicity and to forecast the ongoing activity. I show that models that were originally introduced to forecast aftershock sequences, can be adapted to the settings of induced seismicity. This study presents pseudo-real-time updates of these models. Their performance is inspected with tests developed for global seismic models. The goal is to construct an improved alarm system, based on probabilities, for future EGS projects. The input for this alarm system are seismicity rates, forecast by a compound model, assembled by weighting the contributing models.

The Gutenberg–Richter law describes the event-size distribution of earthquakes: $\log N = a - bM$. A high value of b indicates an abundance of small magnitude events relative to large magnitude events. This study presents a novel approach of focus-centred spatial mapping of the b -value distribution, which allows detailed analysis of the spatial changes of b . Induced seismic sequences show a highly variably spatio-temporal pattern of the b -value. A model, simulating the pore pressure diffusion and relating the event-sizes to the differential stress via an inverse relationship established for tectonic events, aims to evaluate this observation of the b -value distribution. The model implies that high pore pressures lead to high b -values as preferably events with smaller sizes are induced. Moderate pressures lead to values of b similar to the regional average. Since pore pressures decline as a function of distance to the injection point, the probability of observing a large magnitude event thus increases with distance.

For any statistical analysis of a seismic dataset, it is crucial to know the magnitude above which these data are complete. Traditional assessments of the magnitude of completeness M_c are based on the Gutenberg-Richter law. A newer method determines the completeness based on the performance of the stations of a seismic network. This study determines the dependency of this completeness estimate on the data from small independent subnetworks, feeding their data into the main network without using the same triggering algorithm. Additionally, the influence of spurious probabilities of single stations is estimated. Determining a threshold that defines the minimum contribution of a station to the completeness estimate limits the number of involved stations. This reduces the computational time and increases the reliability of the completeness estimate. Three maps for the Northern Californian Seismic Network are presented: 1) The distribution of the probability-based magnitude of completeness, 2) detection probability for M1 events and 3) for M3 events.

Chapter 1

General Introduction

Earthquakes are a natural response of the Earth's crust to the movements of the tectonic plates. Earthquakes occur when the frictional strength of this movement exceeds the strength of the surrounding rock, leading to failure. The result is a release of elastic strain energy. The size of such a seismic event depends on how much stress is released and over how large an area this release occurs. While thousands of earthquakes are recorded daily by seismic networks worldwide, only a few of these are felt and even less cause damage.

Besides these natural earthquakes, human activity may induce earthquakes through processes related to mines, reservoirs, dams and fluid and waste injections (e.g. Chen, 2009; Gupta, 2002; Simpson, 1986; Talwani, 1997) . While the sizes of such seismic events are generally smaller as for natural seismicity, the processes are principally the same. The stress build-up here is, for example, caused by the additional weight of the water column (dams) or added pore pressure in the ground (fluid injections). One of the largest reported earthquakes related to human activity occurred in the 1960's; an event with magnitude 5.5 was recorded in Denver, USA after waste water had been injected into a deep well (Healy et al., 1968; Talwani, 1997). Besides inducing earthquakes directly associated to human activities, there is also the risk of

triggering earthquakes on nearby faults that were previously critically stressed. Such events are often larger and it is more difficult to unambiguously link them to human activity. Dams are often associated with such larger events, for example the Koyna dam in India (Talwani, 1997) or the Zipingpu dam in China (Chen, 2009; Kerr & Stone, 2009). The role of the latter on the Wenchuan earthquake in 2008 is still highly debated.

The above examples can be divided into two different categories: 1) induced seismicity directly correlated to human activity and 2) triggered seismicity, occurring on nearby fault systems. While the event sizes of the first category are often smaller and they are located within or near the rock mass that has been altered, the second category incorporates larger events found further away. The seismic hazard and risk associated with both categories remains to be understood. To mitigate the hazard, events have to be avoided as much as possible. However, for a specific type of experiments, induced seismicity is a result of enhancing the permeability of the underground and thus intimately related to the project progress. In this thesis, I analyse this induced seismicity, associated with Enhanced Geothermal Systems.

1.1 Enhanced Geothermal Systems

The recent catastrophe in Fukushima has shown once again that there is no nuclear energy without risk (Ritterband, 2011) and several countries in Europe are considering abandoning nuclear power (e.g. Schmid, 2011; Scruzzi, 2011b). As energy consumption is unlikely to decline (IEA, 2008), alternatives have to be found.

Geothermal energy provides such an alternative (Holm et al., 2010; Scruzzi, 2011a). This energy exploits heat stored in the Earth's crust, created by radioactive decay. It can be used at different scales, ranging from private heat pumps to large geothermal power plants. For conventional uses, the heat is extracted from the ground by circulating water through a hot reservoir. However, this is only feasible if the permeability and the temperature of the underground are

high, such that the exploitation of the reservoir is profitable. Regions where this is the case are geographically limited (Holm et al., 2010). An alternative to conventional systems is found in Enhanced Geothermal Systems (EGS). These systems can be used where the heat gradient is high, but the natural permeability is too low.

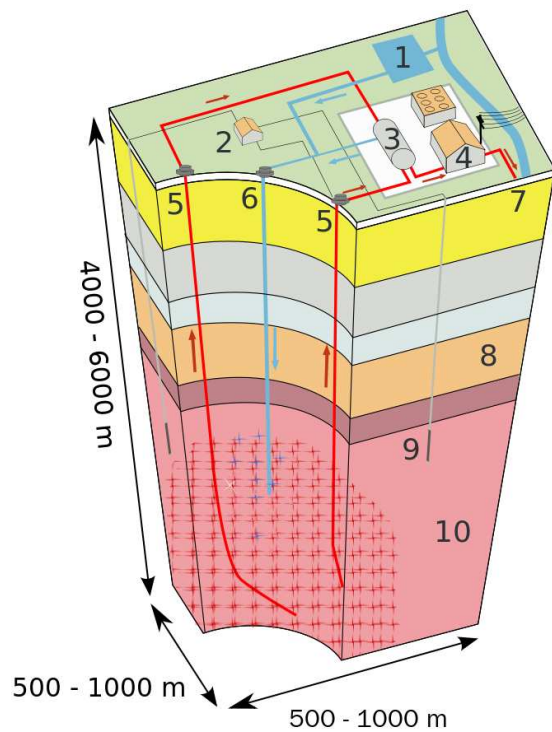


Figure 1.1: Schematic figure explaining the EGS principle. 1) reservoir, 2) pump house, 3) heat exchanger, 4) turbine hall, 5) production well, 6) injection well, 7) heated water for district heating, 8) porous sediments, 9) observation well and 10) crystalline bedrock. ©M. Haering, Geothermal Explorers Ltd, 2007

Figure 1.1 schematically explains the main principle of an Enhanced Geothermal System. Fluid is injected (6) at high pressure into the crystalline bedrock (10). Due to the high pressure, fractures open in the rock. When these fractures connect, the fluid can propagate, expanding the reservoir from which heat can be extracted. This process is associated with microseismic

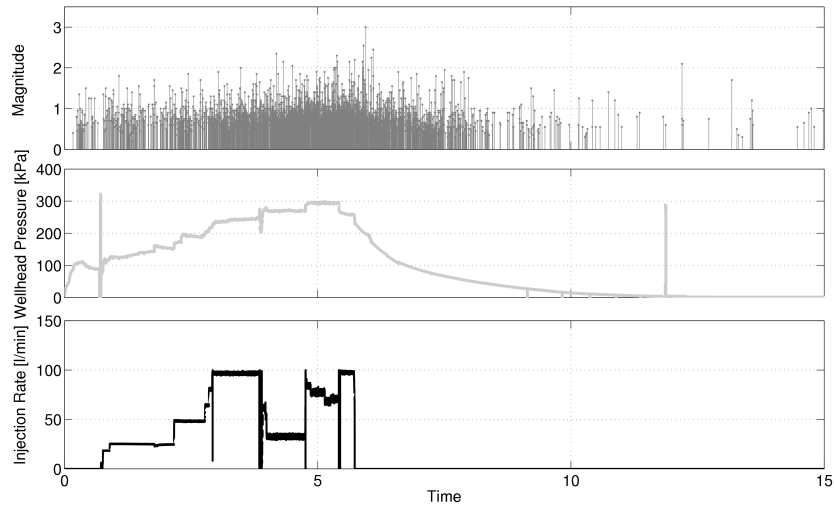
events – each opening of a fracture is equal to an earthquake, albeit small in size. The locations of these events are an important information, as they indicate the extend of the reservoir. The seismicity is therefore recorded by a dense network of seismic stations in adjacent boreholes (9) and at the surface. The entire process of fracturing – with the induced seismicity – until the reservoir is large enough to permit profitable heat extraction is called reservoir stimulation. Once the reservoir has been stimulated and the permeability has been increased due to the connected fractures, water can circulate as in conventional geothermal systems. It is then brought to the surface through the production wells (5), where it can be further used for district heating or electricity production (3, 4).

Operators of EGS face the problem that seismicity is intrinsically related to the process of fracturing and reservoir stimulation and can thus not be avoided. However, if event sizes are too large they might be felt on the ground and possibly lead to damage. Even without damages, the public nuisance decreases the acceptance of the system, if multiple events are felt.

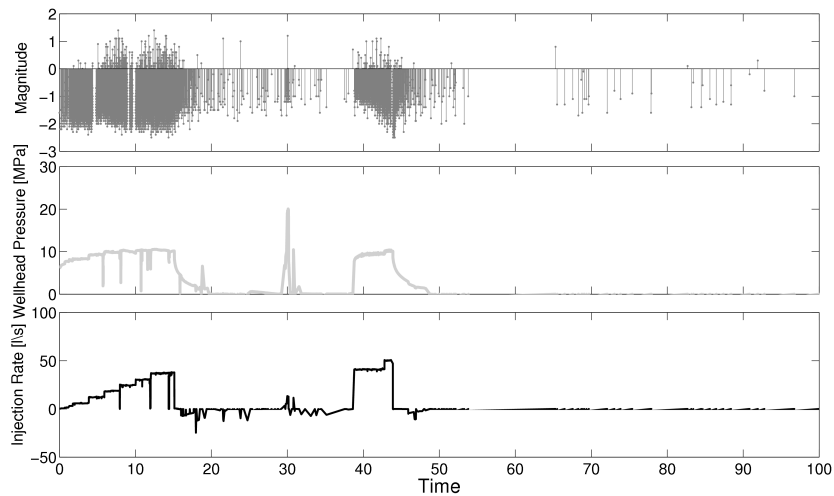
There are several mechanisms to explain seismicity induced by injections of fluids (Majer et al., 2007):

- (I) Changes in pore pressure, where an increase in the pore pressure results in a reduction in stress. This causes an unbalanced stress field which either leads to fractures along the pre-existing stress field, or produces new fractures if the changes are large enough. The second process is called hydrofracturing.
- (II) Changes in temperature, where cool fluids interacting with hot rock surfaces can create fractures due to thermal contraction.
- (III) Chemical alterations, where the injection of water or brine interacts with fracture surfaces and changes the coefficient of friction.

As high pressures are needed for EGS experiments, to open fractures and increase the perme-



(a)



(b)

Figure 1.2: Seismicity rates, wellhead pressure and injection rate for a) Basel in 2006 and b) Soultz-sous-Forêts in 1993. The earthquakes are clearly driven by the injection, they start when the injection is started and decay rapidly after no additional fluid is injected.

ability sufficiently so that fluid can circulate, they are likely the dominant process of the above. The injection rate is highly correlated to the pressure and to the observed event rate (Figure 1.2a and b) (e.g. Majer et al., 2007); increasing injection rates (lowest panels) increases the pressure measured at the wellhead (middle panels), while termination of the injection leads to a slow decay of the wellhead pressure. The seismicity rate (top panels) increases during the injection, and decreases after the injection has been stopped. However, there are still events observed much later, after the wellhead pressure is close to atmospheric pressure again. This can be explained with the pore pressure front that continues to propagate in the underground. The two examples shown are from a) Basel, Switzerland and b) Soultz-sous-Forêts, France. While there was only one longterm injection in Basel in 2006, three injections took place in Soultz-sous-Forêts in 1993. The seismicity rate decreases between injections in the second case, and increases significantly when the next injection starts.

1.1.1 Basel

This thesis shows the work with the induced data set from an EGS project in Basel, Switzerland. The project was set in the centre of this densely populated city (Figure 1.3). The water injection started on 2 December 2006, followed by a rapid increase in the seismicity rate (Figure 1.2a). An event with M_L 2.6 was recorded after six days of injection. In accordance with the alarm system (Bommer et al., 2006; Häring et al., 2008), the water injection was terminated after that. Later on the same day, during the preparations to bleed-off the well, an event with M_L 3.4 occurred (Häring et al., 2008). This event was felt by the public and covered highly by the media. It led to a risk study (Baisch et al., 2009), which concluded that the risk of continuing the EGS project was too high and the project had to be abandoned. During the injection and the following decay, over 11,000 seismic events were recorded. Approximately 3,500 of these had high quality signals and could be located.

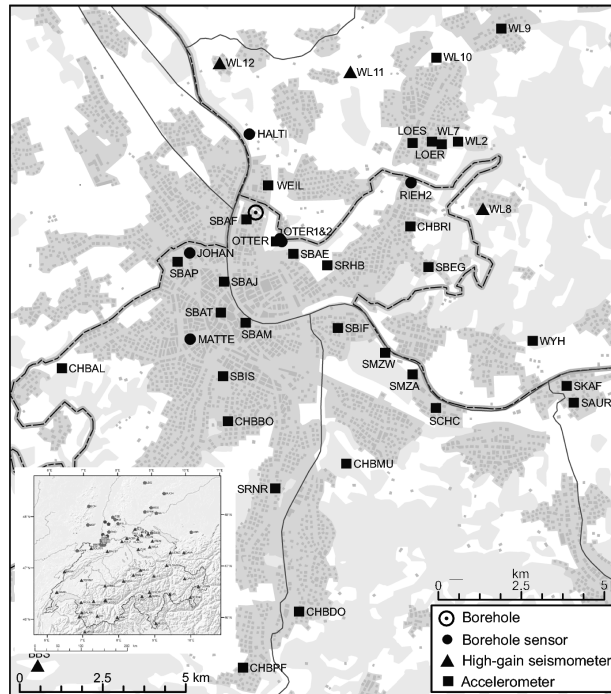


Figure 1.3: Overview of the Basel site. The locations of the borehole and the seismic network are indicated. The grey shading indicates the population density.

1.1.2 Soultz-sous-Forêts

The EGS project in Soultz-sous-Forêts, France has a long history of over 20 years with several injection experiments. The site lies within the upper Rhine graben (Figure 1.4a), where a high heat gradient is observed. This site is an European pilot project to which several partners contributed over the years (www.soultz.net).

Injection test were done through a total of four boreholes(1.4b); while GPK1 is an independent borehole, GPK 3 and 4 are extensions of the GPK 2 borehole. The EPS1 borehole is an extension of an abandoned borehole for oil and gas exploration, this borehole is fully cored and is used to gain information about the bedrock and the existing fractures (Genter & Traineau, 1996). This study analyses seismicity associated with an injection in 1993 into the GPK1 borehole (blue in Figure 1.4b).

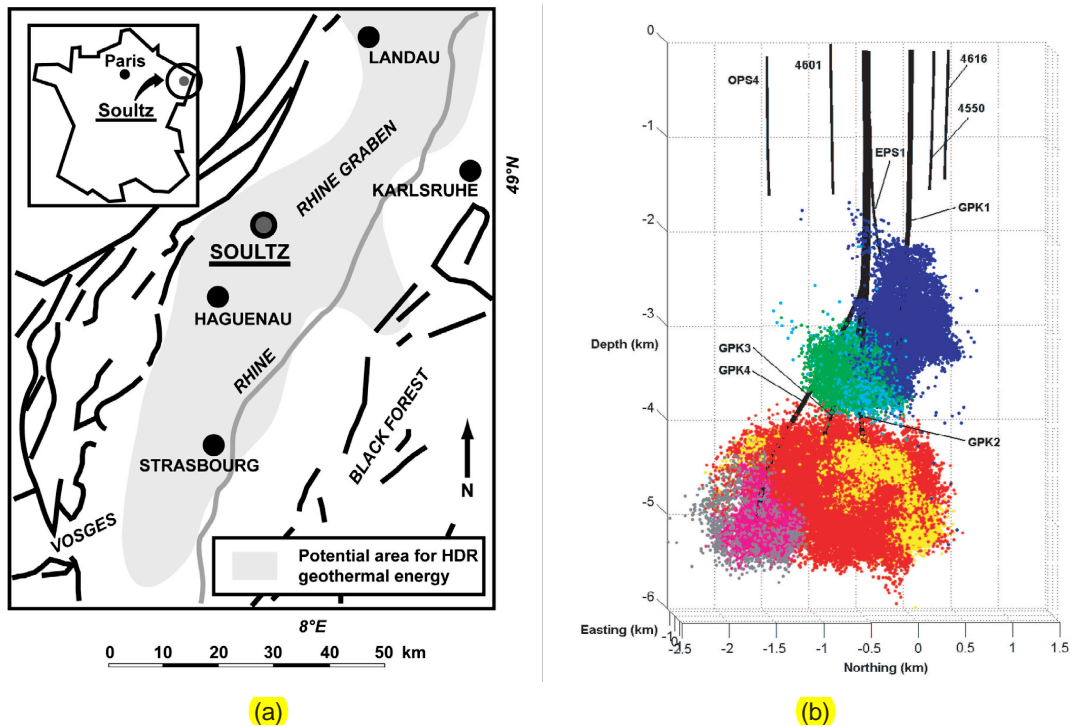


Figure 1.4: a) Overview of the Soutz-sous-Forêts site with the closest cities. The site lies within the upper Rhine graben. b) Overview over boreholes in Soutz-sous-Forêts and the measured seismicity associated with injections into these boreholes. While EPS1 is fully cased, injection test were conducted at different depths for GPK 1 – 4. The numbered boreholes refer to abandoned boreholes within which the seismic network was installed. Figure taken from Cuenot et al. (2008).

During the 1993 injection, a total of three injection tests, stimulating different depths, were conducted. These injections induced a total of about 18,000 microseismic events, of which 12,246 were located (Evans et al., 2005).

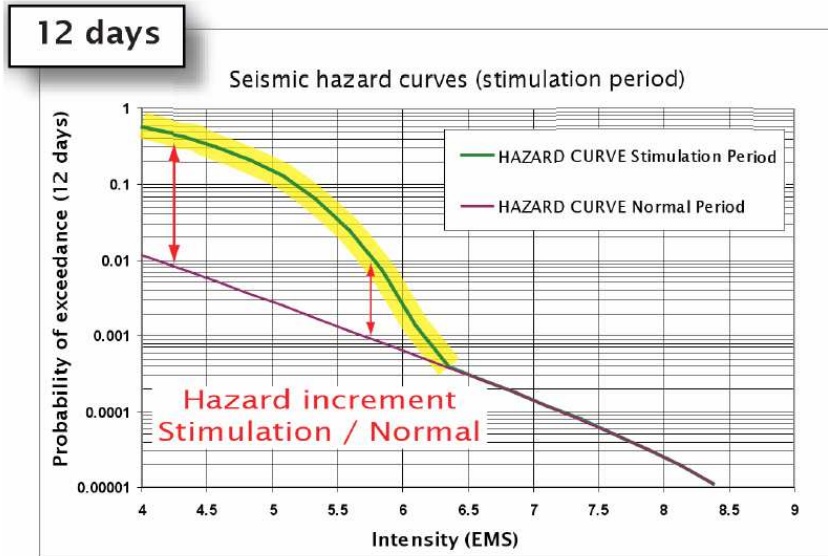
1.2 Challenges of EGS

1.2.1 Induced Seismicity Hazard Assessment

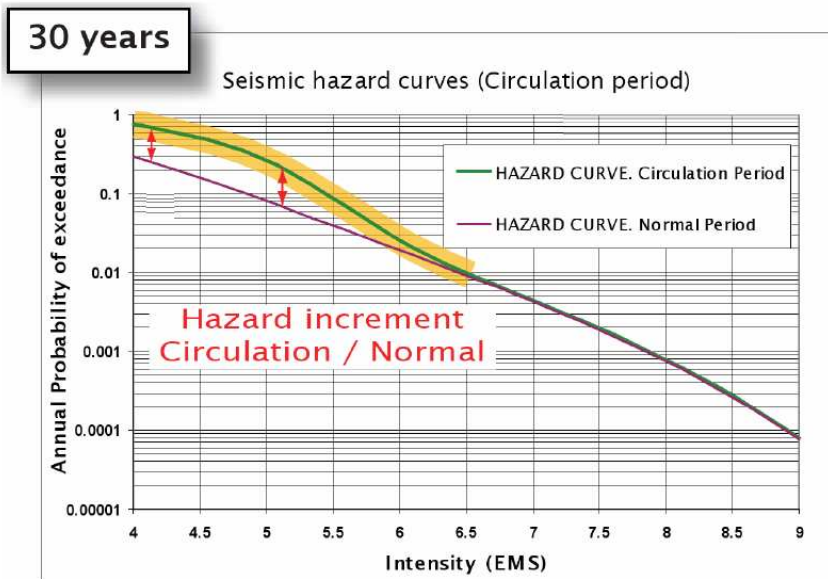
The EGS project in Basel shows the vulnerability of such projects (Giardini, 2009; Kraft et al., 2009). An earthquake with magnitude M_L 3.4 caused the whole project to be abandoned. During the project, there was an alarm system in place – a so-called traffic-light system, based on public response, observed local magnitude and peak ground velocity. This system failed to prevent the magnitude M_L 3.4 event. After the termination of the project, an extensive seismic risk study was performed (Baisch et al., 2009). One main outcome of this study were hazard estimates for different periods of the project (Figure 1.5). However, these only present snapshots, based on the averaged seismicity rate during each period. This is not feasible for future risk assessments as the rates are only known a posteriori.

In my thesis, I approach this problem by introducing time-varying seismic hazard assessment. I update the seismicity rates in real-time and present models that assess the hazard in real-time, based on the ongoing seismicity. This is crucial for new EGS, as the hazard has to be determined during the injection and not a posteriori. As this thesis is based on already recorded seismicity, the hazard assessments are done in pseudo real-time. The goal has to be to apply a real-time model to a future EGS project.

Probabilistic Seismic Hazard Assessment (PSHA) quantifies the potential ground shaking due to earthquakes. Traditional approaches determine the probability of exceeding a certain ground velocity for a long period of time (e.g. Giardini et al., 2004; Wiemer et al., 2009). These cal-



(a)



(b)

Figure 1.5: Probability of exceeding of EMS intensities, according to the Serianex Risk study (Baisch et al., 2009), for a) a 12 day injection period and b) a 30 years operation period. These hazard estimates only present snapshots and are based on average seismicity rates, determined after the termination of the project. ©Serianex

culations are based on historic earthquake catalogues, zonation models and recurrence time models. While this hazard is determined for the longterm and is stable over this period, the hazard associated with induced seismicity is relatively short-term and changes strongly over time.

First estimations of time-varying hazard assessments have been done for aftershock sequences (Gerstenberger et al., 2005; Wiemer & Wyss, 2000). In this thesis, I expand this approach and introduce Induced Seismicity Hazard Assessment (ISHA) to determine the hazard specifically related to induced seismicity. As shown above, seismicity rates are highly correlated with the rate of injection of fluid into a EGS reservoir (Figure 1.2). We can distinguish between four different periods for which the hazard needs to be assessed: I) The planning period, II) the reservoir stimulation, III) the operation period and IV) the post-operation period. The hazard during the first period is equal to the hazard in this region determined by traditional PSHA, while for the other three periods the hazard from the injection is added to this background.

A question that must be addressed is how long the rock will be disturbed due to the fluid injection. This is an essential input for ISHA, as the hazard is increased above the background as long as the seismicity rate is increased. The modified Omori-Utsu law (Ogata, 1999; Utsu, 1961) was introduced to describe the decay of aftershock sequences. This study shows that the decay of induced seismicity, after the fluid injection has been terminated, can be well described by this law.

Analysing the seismicity during reservoir stimulation is an important first step towards ISHA. The seismicity can be forecast with models used previously to forecast seismicity during aftershock sequences (Gerstenberger et al., 2005). Using methods to determine the validity of the models established in the framework of the Collaboratory Study for Earthquake Predictability (CSEP, <http://www.cseptestesting.org/>), I assess which assumptions lead to the models with the best predictive power.

1.2.2 Event-Size Distributions

While it has been proposed before (Baisch et al., 2010) that the largest seismic events occur shortly after fluid injection is terminated, there has so far been no detailed analysis of the event-size distribution within an EGS reservoir. In my thesis, I aim to better understand the processes within the reservoir by analysing the specific frequency–magnitude distribution within different volumes of the reservoir. Linking this pattern to the pore pressure evolution helps to understand the physics behind the event-size distribution.

1.3 Quality Assessment of Seismic Networks

To analyse any seismic data, it is crucial to know the magnitude above this data set is complete. Traditional methods estimate the completeness based on the Gutenberg–Richter law (Gutenberg & Richter, 1942). Schorlemmer & Woessner (2008) introduced a method that is based on the performance of the seismic network and its stations. However, it is not trivial to apply such a method to a seismic network that monitors an EGS project, as only few stations are involved, the triggering conditions change over time and many events are manually re-picked. The smallest network that this method has been applied to so far was the Mponeng gold mine in Carletonville, South Africa, operated by the Japanese-German Underground Acoustic Emission Research in South Africa (JAGUARS) project (Plenkens et al., 2011).

In my thesis, I analyse the method of Schorlemmer & Woessner (2008) for the Northern Californian Seismic Network and introduce new steps in the analysis to make it more reliable.

1.4 Chapter Contents

Chapter 2

This chapter includes the basic statistical analysis of the induced seismicity sequence caused by the EGS project in Basel, Switzerland in December 2006. The duration of the seismic sequence is determined by fitting the modified Omori-Utsu law (Ogata, 1999; Utsu, 1961) to the decay. I show that models previously established to describe aftershock sequences (Ogata, 1988; Reasenbergs & Jones, 1989, 1990, 1994), can be adapted to the settings of an induced seismic sequence, by including the injection rate in the models. These models can then forecast the ongoing seismicity during and after the fluid injection. This is important to determine the time-varying seismic hazard and, therefore, an important first step towards the induced seismicity hazard assessment (ISHA). Such models can, in the future, replace the traffic-light alarm system with a more sophisticated probability-based alarm system. This chapter was published in *Geophysical Journal international* in 2011.

Chapter 3

This chapter includes a detailed assessment of the spatio-temporal history of the statistical parameters of the seismic sequence in Basel. With a novel approach of focus-centred mapping of the spatial distribution of the b -value of the Gutenberg-Richter frequency–magnitude relation (Gutenberg & Richter, 1942), it is possible to analyse spatial differences of the b -value in more detail. The distribution of the b -value can then be related to changes in stress due to the increased pore pressure caused by fluid injection. I introduce a simple two-dimensional model in which events are triggered by changes in pore pressure alone and event-sizes are determined via the inverse relationship between differential stress and b (Amitrano, 2003; Schorlemmer et al., 2005). The spatio-temporal distribution of the b -values from this simulation is similar to

the data, the distribution of the b -value can therefore be related to changes in the pore pressure. This chapter is submitted to *Nature Geoscience*.

Chapter 4

In this chapter, I adapt the methods from Chapter 2 and 3 to the dataset of an induced seismicity sequence from the EGS in Soultz-sous-Forêts in France from 1993. The seismicity of this sequence is more complex than the one observed in Basel, as it was induced by three injections over three months. A detailed spatio-temporal analysis of the statistical parameters of this sequence reveals similarities to the results from Chapter 3. Direct comparisons remain difficult, as the magnitude definitions for both projects were significantly different, the relative changes however, are similar.

This study presents the fit of the best-fitting model of Chapter 2 – an ETAS model (Ogata, 1988), and a model introduced by Shapiro et al. (2010), adapted to pseudo real-time by Mena & Wiemer (2011), to the induced seismicity during the first injection test of the 1993 data from Soultz-sous-Forêts. The performance of these two models is tested with the same algorithms as in Chapter 2.

Analysing the seismic sequence from 1993 injection test in Soultz-sous-Forêts emphasises the general validity of the results from Chapter 2 and 3 and affirms that they are not characteristic to the Basel sequence alone.

Chapter 5

This study analyses the probability-based magnitude of completeness (PMC) method of Schorlemmer & Woessner (2008). It analyses different aspects of this method with the example of the data of the Northern Californian Seismic Network (NCSN). The influence of an independent subnetwork on the completeness estimate, is examined with the example of the data from a

CHAPTER 1. GENERAL INTRODUCTION

network that is designed to record the data of the Geysers geothermal field. This subnetwork does not follow the triggering condition of the NCSN, however it feeds its data into the seismic catalogue. This data has, therefore, to be removed prior to the analysis.

Additionally, the influence of spurious probabilities from single stations is analysed. A new threshold determines the minimum contribution of each station to the completeness estimate. This limits the number of involved stations in the calculation and significantly reduces the computation time as a side effect.

This study presents three maps for the NCSN, based on the parameters of my choice: 1) the distribution of the probability-based magnitude of completeness, 2) the probability to detect a magnitude M1 event and 3) a magnitude M3 event.

This paper will be submitted to *Bullentin of the Seismological Society of America*.

References

- Amitrano, D., 2003. Brittle-ductile transition and associated seismicity: Experimental and numerical studies and relationship with the b value, *J. Geophys. Res. - Solid Earth*, **108**(B1).
- Baisch, S., Carbon, D., Dannwolf, U., Delacou, B., Devaux, M., Dunand, F., Jung, R., Koller, M., Martin, C., Sartori, M., Secanell, R., & Vörös, R., 2009. Deep heat mining basel - seismic risk analysis, Tech. rep., Serianex.
- Baisch, S., Vörös, R., Rothert, E., Stang, H., Jung, R., & Schellschmidt, R., 2010. A numerical model for fluid injection induced seismicity at Soultz-sous-Forets, *International Journal of Rock Mechanics and Mining Sciences*, **47**(3), 405–413.
- Bommer, J. J., Oates, S., Cepeda, J. M., Lindholm, C., Bird, J., Torres, R., Marroquin, G., & Rivas, J., 2006. Control of hazard due to seismicity induced by a hot fractured rock geothermal project, *Engineering Geology*, **83**(4), 287–306.
- Chen, Y., 2009. Did the reservoir impoundment trigger the Wenchuan earthquake?, *Science in China Series D-Earth Sciences*, **52**(4), 431–433.
- Cuenot, N., Faucher, J., Fritsch, D., Genter, A., & Szablinski, D., 2008. The european eggs project at soultz-sous-forêts: From extensive exploration to power production, in *Power and Energy Society General Meeting - Conversion and Delivery of Electrical Energy in the 21st Century, 2008 IEEE*, pp. 1–8.
- Evans, K. F., Moriya, H., Niitsuma, H., Jones, R., Phillips, W. S., Genter, A., Sausse, J., Jung, R., & Baria, R., 2005. Microseismicity and permeability enhancement of hydrogeologic structures during massive fluid injections into granite at 3 km depth at the Soultz HDR site, *Geophys. J. Int.*, **160**(1), 388–412.
- Genter, A. & Traineau, H., 1996. Analysis of macroscopic fractures in granite in the HDR geothermal well eps-1, soultz-sous-forêts, france, *Journal of Volcanology and Geothermal Research*, **72**(1-2), 121 – 141.
- Gerstenberger, M. C., Wiemer, S., Jones, L. M., & Reasenber, P. A., 2005. Real-time forecasts of tomorrow's earthquakes in California, *Nature*, **435**(7040), 328–331.

REFERENCES

- Giardini, D., 2009. Geothermal quake risks must be faced, *Nature*, **461**, 848–849.
- Giardini, D., Wiemer, S., Fäh, D., & Deichmann, N., 2004. Seismic hazard assessment of Switzerland, 2004, Tech. rep., Swiss Seismological Service, ETH Zurich.
- Gupta, H., 2002. A review of recent studies of triggered earthquakes by artificial water reservoirs with special emphasis on earthquakes in Koyna, India, *Earth Science Reviews*, **58**, 279–310.
- Gutenberg, B. & Richter, C. F., 1942. Earthquake magnitude intensity, energy, and acceleration, *Bull. Seismol. Soc. Am.*, **32**, 163–191.
- Häring, M. O., Schanz, U., Ladner, F., & Dyer, B. C., 2008. Characterisation of the Basel 1 enhanced geothermal system, *Geothermics*, **37**(5), 469–495.
- Healy, J., Rubey, W., Griggs, D., & Raleigh, C., 1968. Denver earthquakes, *Science*, **161**(3848), 1301–&.
- Holm, A., Blodgett, L., Jennejohn, D., & Gawell, K., 2010. Geothermal Energy: International Market Update, Tech. rep., Geothermal Energy Association.
- IEA, 2008. Worldwide Trends in Energy Use and Efficiency – Key Insights from IEA Indicator Analysis, Tech. rep., International Energy Agency.
- Kerr, R. A. & Stone, R., 2009. A Human Trigger for the Great Quake of Sichuan?, *Science*, **323**(5912), 322.
- Kraft, T., Mai, P., Wiemer, S., Deichmann, N., Ripperger, J., Kästli, P., Bachmann, C., Fäh, D., Woessner, J., & Giardini, D., 2009. Enhanced geothermal systems - mitigating risk in urban areas, *EOS*, **32**(90), 273–280.
- Majer, E., Baria, R., Stark, M., Oates, S., Bommer, J., Smith, B., & Asanuma, H., 2007. Induced seismicity associated with enhanced geothermal systems, *Geothermics*, **36**(3), 185–222.
- Mena, B. & Wiemer, S., 2011. Building robust models to forecast the induced seismicity related to geothermal reservoir enhancement, *in prep.*.
- Ogata, Y., 1988. Statistical-models for earthquake occurrences and residual analysis for point-processes, *Journal of the American Statistical Association*, **83**(401), 9–27.
- Ogata, Y., 1999. Seismicity analysis through point-process modeling: a review, *Pure appl. geophys.*, **155**, 471–507.
- Plenkens, K., Schorlemmer, D., Kwiatek, G., & the JAGUARS Group, 2011. On the probability of detecting coseismicity, *Bull. Seismol. Soc. Am.*, **In Revision**.

REFERENCES

- Reasenber, P. A. & Jones, L. M., 1989. Earthquake hazard after a mainshock in california, *Science*, **243**(4895), 1173–1176.
- Reasenber, P. A. & Jones, L. M., 1990. California aftershock hazard forecatsts, *Science*, **247**(4940), 345–346.
- Reasenber, P. A. & Jones, L. M., 1994. Earthquake aftershocks – update, *Science*, **265**(5176), 1251–1252.
- Ritterband, C. E., 2011. Vage Ergebnisse der Wiener Konferenz zur Nuklearsicherheit, *Neue Zürcher Zeitung*, **146**.
- Schmid, U., 2011. Der Atomausstieg ist deutscher Konsens, *Neue Zürcher Zeitung*, **151**.
- Schorlemmer, D. & Woessner, J., 2008. Probabilistic magnitude of completeness, *Bull. Seismol. Soc. Am.*, **98**, 2103–2117.
- Schorlemmer, D., Wiemer, S., & Wyss, M., 2005. Variations in earthquake-size distribution across different stress regimes, *Nature*, **437**(7058), 539–542.
- Scruzzi, D., 2011a. Städtische Energiepolitik in neuen Tiefen, *Neue Zürcher Zeitung*, (143).
- Scruzzi, D., 2011b. Erste Schritte und Querelen zur Energiewende, *Neue Zürcher Zeitung*, (133).
- Shapiro, S. A., Dinske, C., Langenbruch, C., & Wenzel, F., 2010. Seismogenic index and magnitude probability of earthquakes induced during reservoir fluid stimulations, *Leading Edge*, **29**(3), 304–9.
- Simpson, D. W., 1986. Triggered Earthquakes, *Annual Review of Earth and Planetary Sciences*, **14**, 21.
- Talwani, P., 1997. On the nature of reservoir-induced seismicity, *Pure appl. geophys.*, **150**(3-4), 473–492, Workshop on Triggered and Induced Seismicity at the 2nd North American Rock Mechanics Symposium (NARMS 96), Montreal, Canada, Jun 18, 1996.
- Utsu, T., 1961. A statistical study of the occurence of aftershocks, *Geophys. Mag.*, **3**, 521–605.
- Wiemer, S. & Wyss, M., 2000. Minimum magnitude of complete reporting in earthquake catalogs: examples from Alaska, the Western United States, and Japan, *Bull. Seismol. Soc. Am.*, **90**, 859–869.
- Wiemer, S., Giardini, D., Fäh, D., Deichmann, N., & Sellami, S., 2009. Probabilistic seismic hazard assessment for Switzerland: best estimates and uncertainties, *J. of Seismology*, **13**(4), 449–478.

Chapter 2

Statistical analysis of the induced Basel 2006 earthquake sequence: Introducing a probability-based monitoring approach for Enhanced Geothermal Systems¹

Corinne E. Bachmann, Stefan Wiemer, Jochen Woessner and Sebastian Hainzl

¹published in *Geophysical Journal international* as C.E. Bachmann, S.Wiemer, J. Woessner and S. Hainzl: *Statistical analysis of the induced Basel 2006 earthquake sequence: Introducing a probability-based monitoring approach for Enhanced Geothermal Systems*

Summary

Geothermal energy is becoming an important clean energy source, however, the stimulation of a reservoir for an Enhanced Geothermal System (EGS) is associated with seismic risk due to induced seismicity. Seismicity occurring due to the water injection at depth has to be well recorded and monitored. To mitigate the seismic risk of a damaging event, an appropriate alarm system needs to be in place for each individual experiment. In recent experiments, the so-called traffic light alarm system, based on public response, local magnitude and peak ground velocity, was used. We aim to improve the pre-defined alarm system by introducing a probability-based approach; we retrospectively model the on-going seismicity in real-time with multiple statistical forecast models and then translate the forecast to seismic hazard in terms of probabilities of exceeding a ground motion intensity level. One class of models accounts for the water injection rate, the main parameter that can be controlled by the operators during an experiment. By translating the models into time-varying probabilities of exceeding various intensity levels, we provide tools which are well understood by the decision makers and can be used to determine thresholds non-exceedance during a reservoir stimulation; this, however, remains an entrepreneurial or political decision of the responsible project coordinators. We introduce forecast models based on the dataset of an EGS experiment in the city of Basel. Between December 2 and 8, 2006, approximately 11500 m³ of water were injected into a 5 km deep well at high pressures. A six-sensor borehole array, was installed by the company Geothermal Explorers Limited (GEL) at depths between 300 and 2700 metres around the well to monitor the induced seismicity. The network recorded approximately 11200 events during the injection phase, more than 3500 of which were located. With the traffic-light system, actions were implemented after a M_L 2.7 event, the water injection was reduced and then stopped after another M_L 2.5 event. A few hours later, an earthquake with M_L 3.4, felt within the city, occurred, which led to bleed-off of the well. A risk study was later issued with the outcome that the experiment could not be resumed. We analyse

the statistical features of the sequence and show that the sequence is well modelled with the Omori-Utsu law following the termination of water injection. Based on this model, the sequence will last $31+29/-14$ years to reach the background level. We introduce statistical models based on Reasenberg and Jones and Epidemic Type Aftershock Sequence (ETAS) models, commonly used to model aftershock sequences. We compare and test different model setups to simulate the sequences, varying the number of fixed and free parameters. For one class of the ETAS models, we account for the flow rate at the injection borehole. We test the models against the observed data with standard likelihood tests and find the ETAS model accounting for the on flow rate to perform best. Such a model may in future serve as a valuable tool for designing probabilistic alarm-systems for EGS experiments.

2.1 Introduction

Enhanced Geothermal Systems (EGS) represent an attractive source of alternative energy with a low carbon footprint and few environmental concerns. EGSs are commonly known as “hot-dry-rock” or “hot-fractured-rock” technique and refer to a technology that uses hydraulic stimulation of a hot ($T > 100 \text{ }^\circ\text{C}$) but comparably impermeable ($\kappa < 10^{-16} m^2$) rock mass at depth ($Z > 3$ kilometres) to create an artificial geothermal reservoir. These systems are most economically viable in areas with a steep geothermal gradient because drilling costs increase exponentially with depth. Proximity to end users of heat and electricity gained from depth is desirable in order to minimize energy loss through distance.

In a “hot-dry-rock ”experiment, the rock mass is stimulated hydraulically by pumping fluids through an injection well under high pressure into the target area at depth (e.g., Smith, 1983; Tenzer, 2001). The increase in pore pressure as the fluid propagates away from the injection well fractures the host rock locally. Generating fractures in the target rock mass simultaneously causes micro-seismicity through the fracturing process, defining the paths of the fluids to

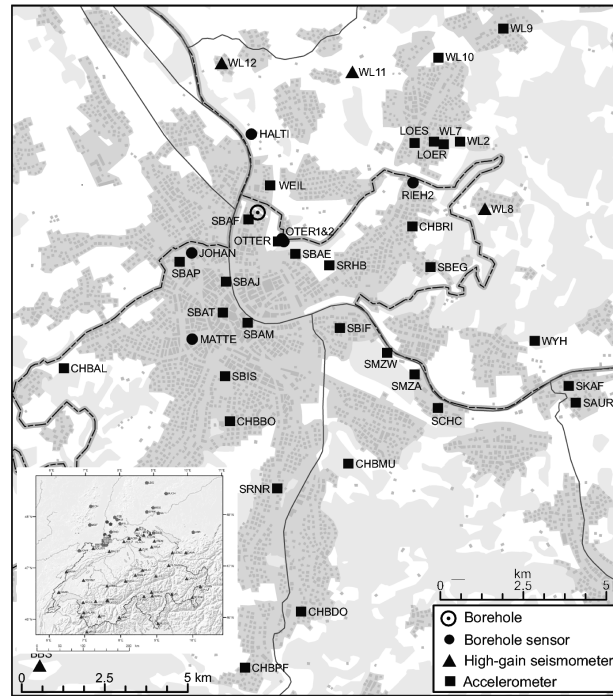


Figure 2.1: Overview of the study region with all seismic stations. Different symbols show borehole and strong motion stations maintained by either Geothermal Explorers or the Swiss Seismological Service. The inset indicates the location of all seismic stations in Switzerland with the high density of stations around Basel

flow through and heat up. The spatial distribution of the micro-earthquakes provides important clues about the volume and orientation of the fractured rock at depth. Highly sensitive seismic monitoring techniques are routinely applied at EGS sites to map the spatial and temporal development of the stimulated volume and to characterise the geothermal reservoir (e.g., Häring et al., 2008; Wohlenberg & Keppler, 1987). Once a sufficiently large reservoir (volume $> 1 \text{ km}^3$) has developed, a second well is typically drilled into the stimulated volume. Water then flows between the two wells; hot water is extracted from the production borehole and engineered to an energy resource. Artificially creating fractures in rock is a necessary component of an EGS; this process bears the risk of producing not only micro-earthquakes but also possibly moderate to large magnitude earthquakes that could cause damage (Giardini, 2009; Kraft et al., 2009).

One of the first purely commercially oriented EGS projects was initiated in Basel, Switzerland, in 1996 by an industry consortium (GeoPower Basel) (Häring et al., 2008). The consortium led by Geothermal Explorers Ltd (GEL) was well aware of the possibility of inducing earthquakes strong enough to be felt. To monitor earthquake activity and be prepared for hazard and risk mitigation actions, GEL adapted a ‘traffic-light’ system first proposed by Bommer et al. (2006) for the ‘Berlin’ geothermal project in El Salvador. The four stage traffic-light system was based on three components: 1) Public response, 2) observed local magnitude and 3) peak ground velocity (PGV). Häring et al. (2008) explain the different stages in detail; we only provide an abbreviated version here. According to the three components, the injection of fluids would either be 1) continued as planned (green), 2) continued but not increased (yellow), 3) stopped and bleed-off stimulation pressure started (orange) or 4) stopped and bleed-off to minimum wellhead pressure started (red), where bleed-off implies to actively pump water out of the borehole. The traffic-light system is defined *ad-hoc* and mainly based on expert judgement; however, it was the one single system that had been used in similar projects before (Bommer et al., 2006) and others did not exist at the time.

The fluid injection started on December 2, 2006. Approximately 11500 m^3 water were injected into a 5 km deep well at increasing flow rates (Häring et al., 2008) to stimulate the reservoir. The seismicity was monitored by a six-sensor borehole array at depths between 300 m and 2700 m around the injection well (GEL) and by up to 30 seismic surface stations in the Basel area (SED) (Figure 2.1). More than 11200 events were recorded, more than 3500 of which were located by GEL (Figure 2.2). The gradual increase in flow rate and wellhead pressure was accompanied by a steady increase in seismicity, both in terms of event rates and magnitudes (Figure 2.3). In the early morning hours of December 8, after water had been injected at maximum rates in excess of 50 l/s and at wellhead pressures of up to 29.6 MPa for about 16 hours (Häring et al., 2008), a magnitude M_L 2.6 event occurred within the reservoir. This triggered the ‘orange’ alarm level, so that the injection pressure was reduced around 8.12.06, 4:00a.m., and fully stopped on the

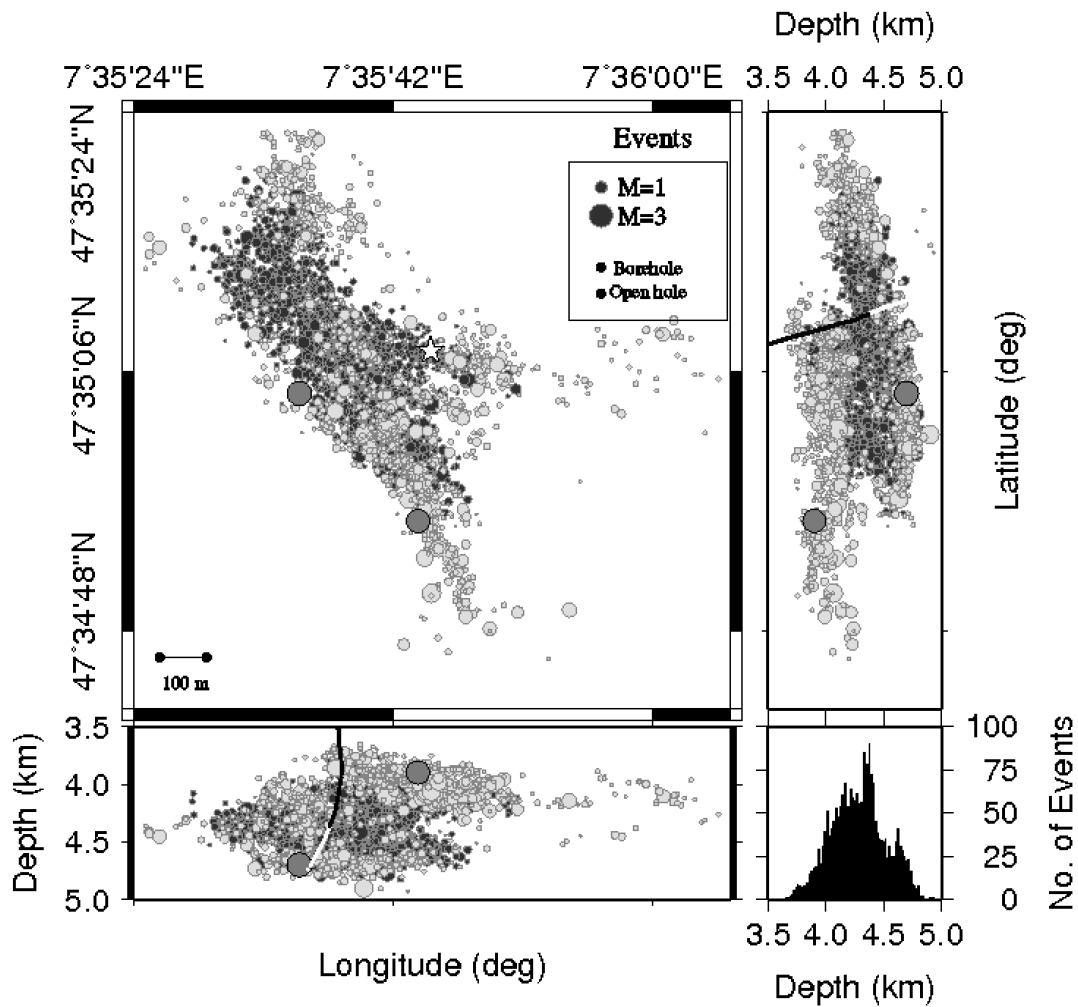


Figure 2.2: Distribution of the events in plane view (top left) and as depth distributions (EW lower panel and NS right panel). Circle sizes are scaled by magnitude; events with magnitudes above 3 are highlighted with darker colours. Events in black occurred during the injection and events in grey after water injection was terminated. The borehole is indicated; the darker part is cased and the lighter part is open.

same day at 11:33a.m (Häring et al., 2008). However, an M_L 3.4 event occurred five hours later, widely felt within the city of Basel. Slight non-structural damage, such as fine cracks in plaster, corresponding to an intensity of V on the European Macroseismic Scale (EMS98), has been claimed by many homeowners, with a damage sum, estimated and to a large extent already paid by insurance, of US \$7 million (Kraft et al., 2009). About one hour after the M_L 3.4 event, bleed-off was initiated by opening the injection well, and hydrostatic down-hole pressure was reached within four days. Following this, the seismicity slowly decayed. However, three additional felt earthquakes with $M_L > 3$ occurred one to two months after bleed-off. More than three years later, sporadic seismicity inside the stimulated rock volume is still being detected by the down-hole instruments. The EGS project was on hold for more than two years, awaiting the completion of an independent risk analysis study. The results of this study, completed in November 2009 (Baisch et al., 2009a), suggest that the risk of further felt and potentially damaging events is substantial. Public authorities thus decided that the project cannot be continued.

This well-monitored induced seismic sequence provides an excellent opportunity to improve the understanding of the physics of EGS. The Swiss Seismological Service (SED) at ETH Zurich, for example, is investigating the Basel dataset in the framework of the multidisciplinary research project GEOTHERM (www.geotherm.ethz.ch) of which this study is a part. Several results have already been published (e.g., Deichmann & Ernst, 2009; Deichmann & Giardini, 2009; Kraft et al., 2009; Ripperger et al., 2009) and additional studies currently being conducted to be published.

The pressure reduction and eventual bleed-off of the system during the critical days around December 8, 2006 was consistent with the actions stipulated in the traffic-light systems; however, the public outcry, ongoing legal actions and ultimate termination of the Basel EGS project highlights clearly that the traffic-light system was, at least in this case, not a sufficient monitoring and alerting approach. A major goal of this study is to develop and test alternative probability-based statistical approaches to the traffic-light system. To achieve this goal, we first need to evaluate

the performance of available statistical models that suitably describe and forecast features of induced seismicity and are readily able to forecast future seismic activity.

To model induced seismicity, a variety of approaches have been proposed in the past. Primarily physics-based approaches (Baisch et al., 2009c; Kohl & Megel, 2007; Shapiro & Dinske, 2009; Shapiro et al., 2007) suggest a hydro-mechanical model of fluid migration through the rock matrix and cracks. Events in such a model are triggered directly by shear failure of favourably oriented natural joints as a response of normal stress reduction due to high-pressure fluid injection (e.g., Baisch et al., 2009b,c). Such an approach also forms one of the logic tree branches of the Basel risk study and has been applied to other EGS projects, such as Soultz-sous-Forêts (Baisch et al., 2009b) or Cooper Basin (Baisch et al., 2009c). In this study, however, we focus on statistical approaches that describe the time-dependent seismic hazard as a combination of empirical observation and statistical modelling of the observed seismicity. A model in this sense defines the total number and frequency–magnitude distribution of the future seismicity in a given time window. The aim of the models is to best forecast the seismicity but not necessarily to understand the detailed physics of the ongoing processes. In a statistical framework, the seismic sequence triggered by fluid injection can be understood and described as a point process, as for any other sequence of clustered earthquakes. In addition to fluid-triggered events, each event potentially triggers ‘daughter’ earthquakes by the static and dynamic stress changes induced by their rupture. The overall seismicity can be described as a cascading, or epidemic, process, responding to an external forcing function.

The advantage of using statistical models to describe the seismicity during EGS stimulation is that the models are comparatively simple and well established in statistical seismology (eg. Gerstenberger et al., 2005; Hainzl & Ogata, 2005; Ogata, 1988; Woessner et al., 2010). We show in this paper that the entire Basel sequence can in fact be well described using statistical models. We argue that such models should be considered as a starting point or reference model for any assessment of the time-dependent seismic hazard.

We adopt and compare two model frameworks widely used in the domain of time-varying earthquake forecasting on time scales of hours and days:

- (1) The Reasenberg & Jones model, which is the basis of the Short Term Earthquake Probabilities (STEP) model (Gerstenberger et al., 2005, 2007; Woessner et al., 2011). STEP-based hazard maps were first implemented for time-dependent hazard forecasts in California and are available online at the United States Geological Survey (USGS) (<http://earthquake.usgs.gov/eqcenter/step/>).
- (2) The Epidemic Type Aftershock Sequence (ETAS) model (Hainzl & Ogata, 2005; Ogata, 1988). Based on ETAS, we also develop a model that takes the time-dependent pumping rate as an external forcing term into account.

None of these models has so far been applied to EGS-related seismicity but they are well established and tested in retrospective and in fully prospective forecasting experiments at regional scale (www.cseptesting.org; Schorlemmer et al., 2010; Woessner et al., 2011), as well as on the scale of aftershocks sequences (Cocco et al., 2010; Hainzl et al., 2009; Woessner et al., 2011).

We compare the forecasting ability of a total of eight models with standard likelihood testing approaches introduced by the Collaboratory for the Study of Earthquake Predictability (CSEP; Schorlemmer et al., 2010; Woessner et al., 2011; Zechar et al., 2010). We propose that a quantitative approach to model testing and evaluation is valuable as the ultimate goal is to establish models that can be used for regulatory guidelines.

2.2 Data

The seismicity analysed in this study was recorded by six permanent downhole borehole geophones, operated by GEL. Four of the geophones were installed at intermediate depths between

300 and 600 metres below the surface, one was at 1180 m and the deepest one at 2740 m. Prior analysis of this network led to the conclusion that two geophones at intermediate depth had a minor influence on the resolution and therefore they were not routinely processed (Dyer et al., 2008). Figure 2.1 indicates the location of the stations involved in the data acquisition. In addition to the borehole network, the SED maintained a dense network of seismometers and accelerometers; their locations are also shown in Figure 2.1.

The GEL network recorded over 11200 events from December 2006 to July 2008; 3500 had a good quality signal and were located. Two magnitudes were provided; 1) local earthquake magnitudes (M_L) were provided by the Swiss Seismological Service (SED) for the largest ~ 190 earthquakes only; and 2) a moment magnitude (M_W) was determined by the microseismic network of GEL (Dyer et al., 2008). Since the moment magnitudes are available for all 3500 events, we will be using them throughout this report. Bethmann et al. (2007) showed that the moment magnitudes provided by GEL are comparable to the moment magnitudes calculated by the SED. Figure 2.2 indicates the locations of all events located by GEL; earliest events occurred around the casing shoe and then migrated away from the opening, while latest events occurred to the east of the borehole. Dyer et al. (2008) and Häring et al. (2008) describe the evolution of seismicity in more detail.

Figure 2.3 shows the time-evolution of the events; the top panel shows the sequence until July 25, 2008 and the middle left panel a close-up from December 2 to December 12, 2006. Gray stems indicate single events, with magnitudes ranging from M_W 0.1 to M_W 3.1, where the M_W 3.1 event is equal to the earlier mentioned M_L 3.4 event which occurred at December 8, 2006, 4:48 p.m. Three additional events with magnitudes above three occurred in January and February 2007. The lowest panel in Fig. 2.3 includes the applied flow rate. The injected water was increased step wise and reached a maximum of about 100 l/sec before it was reduced. Dyer et al. (2008) describe the water injection and the pressure evolution in more detail.

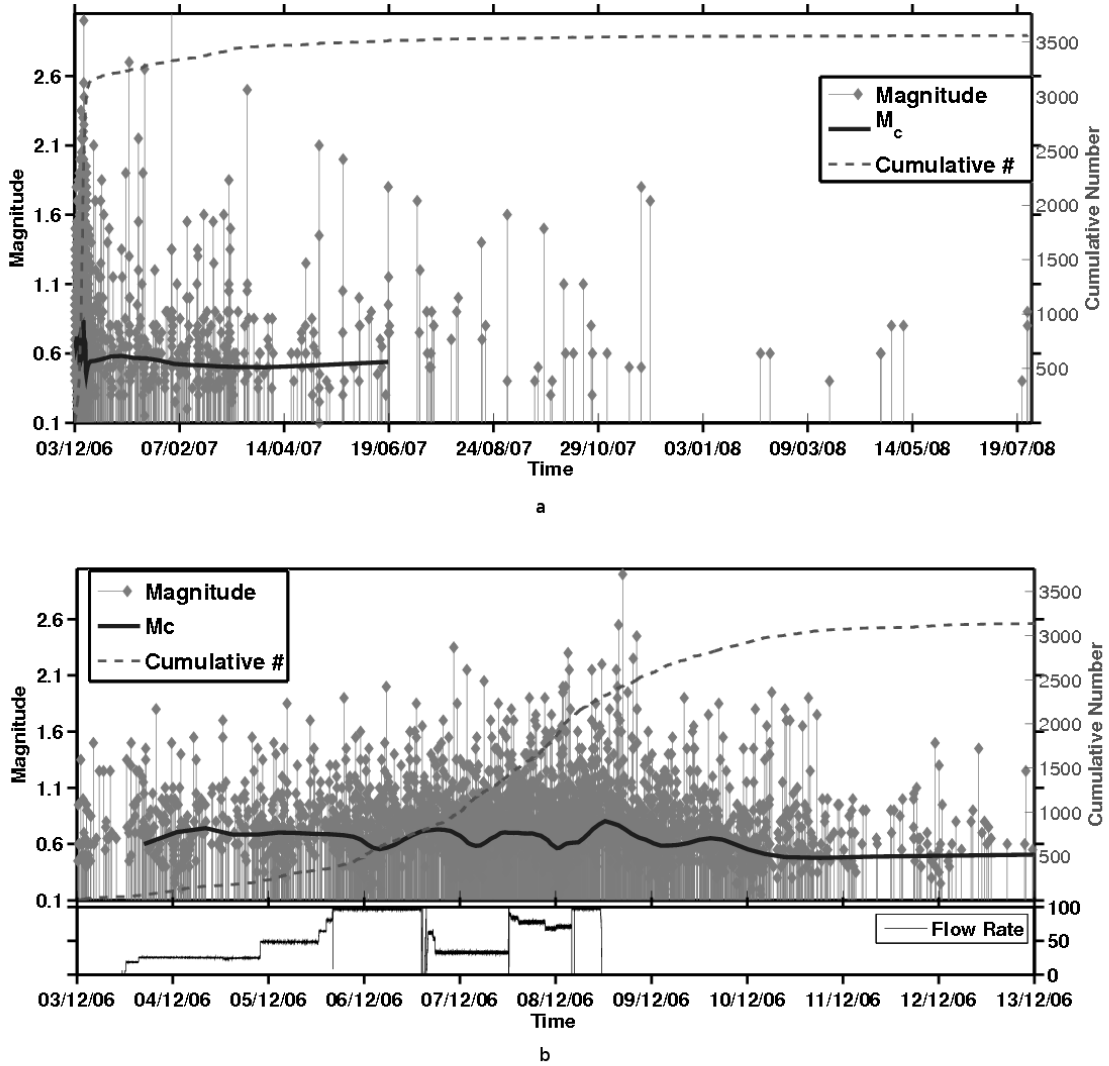


Figure 2.3: Completeness and time evolution of the (a) whole catalogue and the (b) first ten days. The black solid line indicates the variation of the completeness of this catalogue over time; it varies the most during the first days and then becomes constant. We did not determine the completeness after June 2007, as the seismicity becomes too sparse.

2.3 Method

2.3.1 Fitting the overall parameters of the sequence: b-values and duration

In a first step, we analyse the monitoring completeness and bulk statistical parameters of the sequence. Of specific interest in this context is an estimate of the time required for the seismicity to return to the background rate. This estimate has, possibly, an impact on the continued need to monitor the site.

To estimate seismicity parameters, we first need to analyse the magnitude of completeness, (M_c), of the catalogue as a function of time. We apply the maximum curvature method (Wiemer, 2000; Woessner & Wiemer, 2005) and require 150 events to estimate the M_c for one sample. Most computations in this study are based on adaptations of the software package ZMAP (Wiemer, 2001). The completeness estimates span a period starting about midday December 3, 2006 until June 2007, after which the seismicity becomes too sparse (Figure 2.3, as indicated by the black line). $M_c(t)$ varies between $0.5 \pm 0.07 \leq M_c \leq 0.9 \pm 0.11$ during the first nine days of the time series (Figure 2.3). These variations are most probably due to unpicked events during times of highest activity, because smaller events are hidden in the coda of larger ones. After a little more than one month, $M_c(t)$ remains constant at 0.5 ± 0.07 . For the overall completeness of the entire sequence, we choose in the subsequent analysis a conservative value of 0.9, the maximum observed in any time period.

We then estimate activity rates and relative earthquake size distribution during the injection phase and the post-injection period. Using a maximum likelihood fit, we determine the a - and b -values of the Gutenberg-Richter (GR) law (Gutenberg & Richter, 1942) which describes the

relation between the frequency of earthquakes and the magnitudes of an event:

$$\log N = a - bM \tag{2.1}$$

where N is the number of events with magnitudes larger or equal to M , a describes the productivity of the sequence and b the ratio of small to large events.

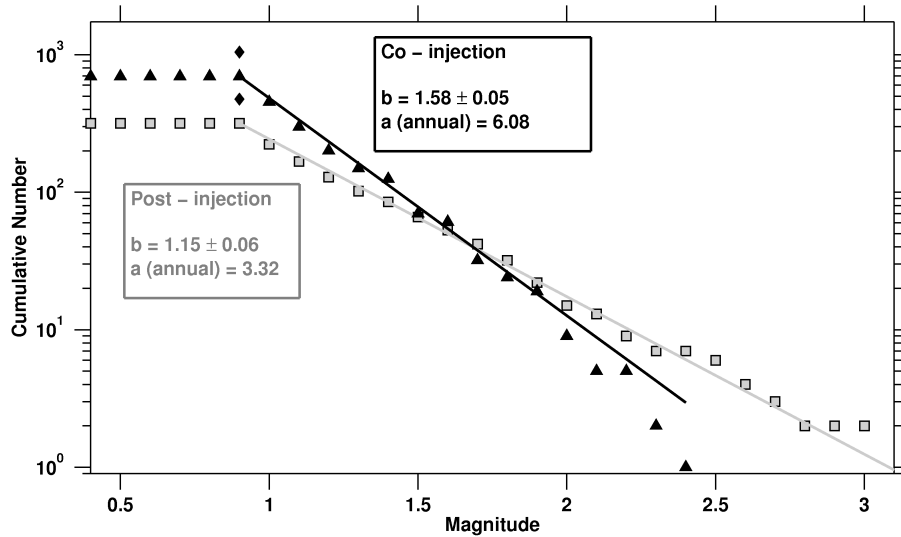


Figure 2.4: Gutenberg-Richter frequency–magnitude relation for two different sequences. Darker triangles show events during the injection, lighter squares mark events after the termination of water injection. Gutenberg-Richter parameters are indicated for each sequence.

We find a substantial decrease of the b -value from 1.56 ± 0.05 to 1.15 ± 0.07 for co- and post-injection events, respectively, using the above determined M_c of 0.9. All uncertainties are computed by bootstrapping the data set 100 times and fitting the parameters values to the bootstrap samples. The annual a -values for the same periods change from 6.08 to 3.31 (Figure 2.4, colours as in fig. 2.2).

Once the injection of water under high pressures stops, the seismicity decays gradually in the following weeks and months (Figure 2.5), quite similar to any tectonic aftershock sequence. For

aftershock sequences, the rate is usually well described by the Omori-Utsu law (Ogata, 1999; Utsu, 1961):

$$\lambda(t, M_c) = \frac{k(M_c)}{(t + c)^p} \quad (2.2)$$

where t is the time elapsed after the main shock, c and p are empirical parameters, characteristic for a specific sequence, and $k(M_c)$ is a function of the number of events with magnitudes above the completeness magnitude M_c .

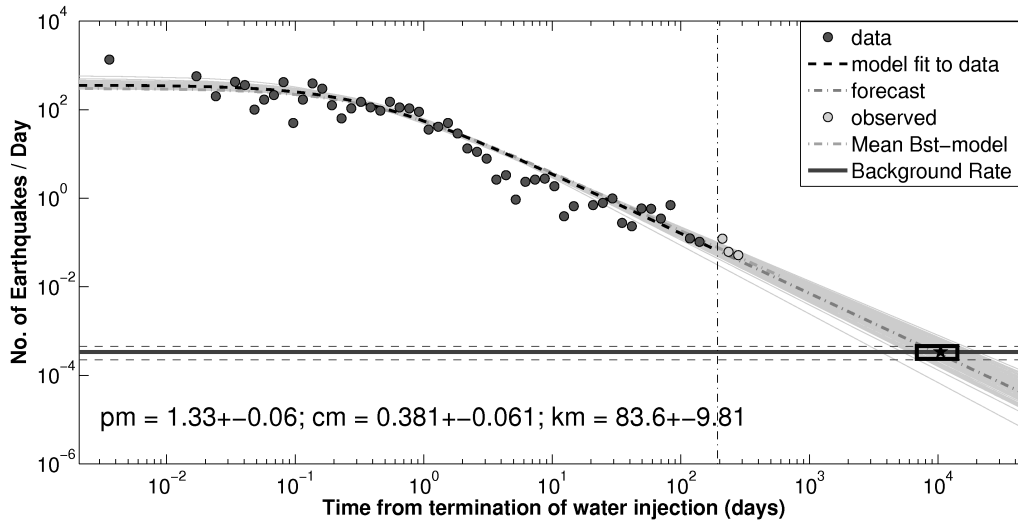


Figure 2.5: Decay of the sequence after the termination of the water injection. A modified Omori-Utsu law is fitted to the sequence to determine its duration; circles represent the data. We only fit the first 200 days of data (dark circles); events after this time (grey circles) fall within the uncertainty. The background of this region and the uncertainty are indicated at the bottom of the figure. Where they intercept with the model, we find the duration of the sequence. The black box indicates the uncertainty and the black star the best fit. We find a duration of $31 + 29 / - 14$ years.

We investigate whether the Omori-Utsu law can provide an acceptable fit to the data of the post-injection period. We fit the events with $M_w \geq 0.9$, that occurred between the end of the injection (December 8, at 11:33 a.m) and day 200 of the sequence. We find $p = 1.33 \pm 0.06$, $c = 0.38 \pm 0.061$ days and $k = 86.6 \pm 9.81$ (Figure 2.5) as the mean parameters for 1000 bootstrap models. The two-sample Kolmogorov-Smirnov (Conover, 1972; Woessner et al., 2004) test,

testing whether the cumulative rate of the data and the fitted Omori-Utsu law belong to the same distribution, is not rejected at the significance level of 0.05. This indicates a good fit of the Omori-Utsu law to our data.

To estimate the expected duration of the sequence, we additionally determine the background seismicity rate for this region. No event has ever been located within the small stimulated volume of about 1 km³ during the 25 year history of recording micro-seismicity in Switzerland. We therefore use as a proxy the seismic activity rate of the seismogenic source zone of Basel used in the determination of the Swiss Seismic hazard in 2004 (Giardini et al., 2004; Wiemer et al., 2009). The rate is normalised to the size of the stimulated volume (more specifically, to its 2D areal extension). This assumption is consistent with the definition of a seismic source as a zone of equal seismic potential in seismic hazard assessment. The seismogenic source zone has an a -value of 2.31, a b -value of 0.9, and spans over an area of 1741 km². The area affected by the injection is 1.6 km² which leads to a background rate of $R_b = 3.38e^{-4}$ events per day with $M_w \geq 0.9$. In other words, an $M_w \geq 0.9$ event should occur naturally only about every eight years. If we solve the Omori-Utsu law (eq. 2.2) for the duration, we get (Woessner, 2005)

$$t_a = \left[\frac{k}{R_b} \right]^{\frac{1}{p}} - c \quad (2.3)$$

With these values, we obtain a duration of the ‘aftershock’ sequence of $t_a = 31 + 29/ - 14$ years, where the uncertainties are obtained from the bootstraps in Figure 2.5.

2.3.2 Forecasting Models

We apply two different classes of model, which we introduce in the following paragraphs. Both models have been used to forecast aftershock sequence and are modified by us to be applied to an induced seismic sequence.

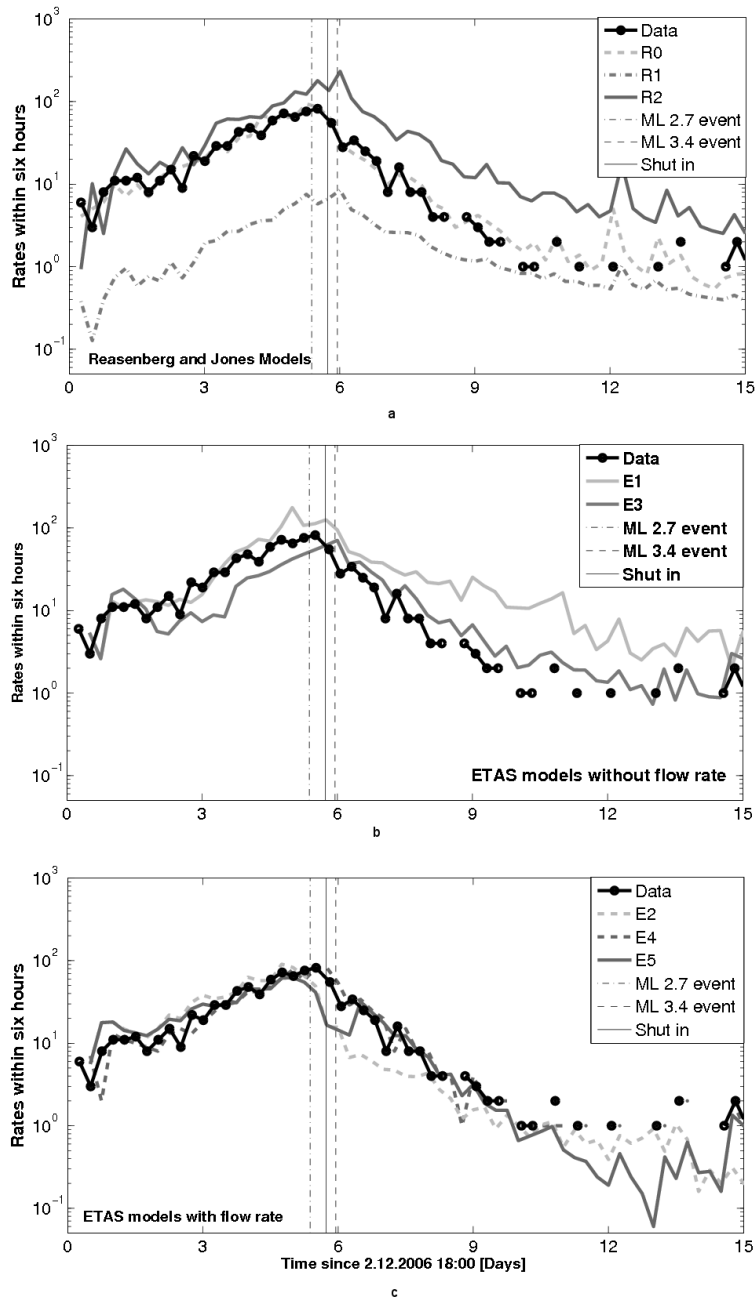


Figure 2.6: Summary of all eight models; (a) three models based on the Reasenberg & Jones approach, (b) two models based on ETAS approach without flow rate and (c) three models based on ETAS approach with flow rate. In all three panels, the observed rates within the next six hours is indicated with a bold black line and circles. The time of the shut in and the two largest events that led to actions within the traffic light system are indicated.

2.3.2.1 The Reasenberg & Jones model

Reasenberg & Jones (1989, 1990, 1994) combine the Gutenberg-Richter (GR) law (equation 2.1) and the Omori-Utsu law (equation 2.2) to determine the probability of triggering earthquakes. They express the rate λ of aftershocks with magnitudes larger than M_c at a given time t after the main shock with magnitude M_m as

$$\lambda(t, M_c) = \frac{10^{\tilde{a}+b(M_m-M_c)}}{(t+c)^p} \quad (2.4)$$

where \tilde{a} is given as

$$\tilde{a} = A_0 - \log \left[\int_S^T (t+c)^{-p} dt \right] \quad (2.5)$$

where

$$A_0 = a - b \times M_m \quad (2.6)$$

and a , b , p and c are the same constants as in equation 2.1 and equation 2.2, respectively.

The probability P of one or more events occurring in the magnitude range ($M_1 \leq M < M_2$, with $M_1 \geq M_c$) and the time range ($S \leq t < T$) is then given as (Wiemer, 2000):

$$P = 1 - \exp \left[- \int_S^T \lambda(t, M) dt \right] \quad (2.7)$$

Here, we treat each individual event as a main shock and sum the rates λ in each time bin to obtain the joint probability P of observing one or more event in the given magnitude range.

2.3.2.2 Epidemic Type Aftershock Models

We use an epidemic type aftershock (ETAS) model of Ogata (1988). The rate of aftershocks induced by an event occurring at time t with magnitude M_i is given by

$$\lambda_i(t) = \frac{K}{(c + t - t_i)^p} 10^{\alpha(M_i - M_{min})} \quad (2.8)$$

for time $t > t_i$. The parameters c and p are empirical parameters (compare Eq. 2.4) and K and α describe the productivity of the sequence. The total occurrence rate is the sum of the rate of all preceding earthquakes and a constant background rate λ_0 :

$$\lambda(t) = \lambda_0 + \sum_{[i:t < t_i]} \lambda_i(t) \quad (2.9)$$

We consider that the forcing term should depend on the applied injection flow rate F_r . According to Shapiro & Dinske (2009), we can model the fluid-triggered event rate as proportional to the injection rate. We therefore modify the background to be:

$$\lambda_0(t) = \mu + c_f \times F_r(t) \quad (2.10)$$

with c_f and μ being free parameters.

Forecasts with the ETAS model have to include secondary aftershock triggering during the prediction period. For that purpose, we use the mean of 10,000 Monte Carlo simulations based on the inverse transform method by Felzer et al. (2002) to obtain a sb forecast. The contribution in each magnitude bin is simply obtained by applying the Gutenberg-Richter frequency–magnitude relation to this rate with a given b -value.

For the Basel case study, we test different model versions:

- In two versions (E1 and E3), we set $c_f = 0$ in order to see whether the model without the

physically reasonable dependence on the flow rate has a similar prediction power.

- Fitting too many parameters to a limited data set can also lead to a reduced prediction power of the model. Thus we fixed in two versions (E1 and E2) as many parameters as possible to generic parameters known from previous model applications.
- In versions E4 and E5, we fit c_f in addition to all other parameters. To forecast rates for time t_i , we use $F_r(t_{i-1})$ for E4 and $F_r(t_i)$ for E5.

2.4 Modelling approaches

Before we apply and compare the statistical forecast models, we define a common framework in which we apply and test the models. This involves choosing the testing period, the updating strategy and the magnitude range in which to test the forecast. While these choices are somewhat arbitrary, they can potentially have a significant effect on the outcome of the testing, and they reflect to some extent the requirements of end users. We use the experience of the RELM and CSEP experiments to define the ‘rules of the game’ and retrospective testing of aftershock sequences (Field, 2007; Schorlemmer et al., 2010; Woessner et al., 2011).

For both model classes, the RJ-models (R0-R2) and the ETAS-models (E1-E5), we apply two modelling approaches: 1) Use one set of predetermined parameters from the entire sequence and 2) Update model parameter values with successively extending the period for assembling data by six hours. Models R1, E1 and E2 fall into class (1); we use generic parameters defined for other sequences and make forecasts with those in six hour bins. Models R2 and E3-E5 fall into class (2); here, we start with the same generic parameters, but after the first six hours of data, we fit the parameters to the data. We use increasing time bins and fit the parameters again after every time bin. For example, we fit the parameters to the first twelve hours of events to forecast hours 12 to 18. For both classes, we evaluate the performance of the models in six

hour bins.

In addition, we consider one model, R0, which is non-causal in the sense that it represents the best fit of a R&J model to the sequence. For this model, we divide the sequence in two parts, a co-injection and a post-injection period and fit a set of parameters to each period.

Table 2.1 summarises all eight models. For all models, we have both fixed and free parameters. The fixed parameters are based on generic values determined for other sequences or values found in the literature. For all approaches we fix the b -value at 1 and the c - value at 0.01 which is somewhat arbitrary; both values are often found in literature. We use neither the b -value fitted to the sequence nor the b -value of the seismic source zone as we can not justify using either of them in the forecasting mode. Using a c - value of 0.01 is consistent with the literature (Reasenberg & Jones, 1989). For the R&J models we use generic parameters defined by Reasenberg & Jones (1989), for model R1 we use them for the whole sequence, for R2 we start with those parameters. For the ETAS models, we use the generic parameters of $p = 1.2$ and $\alpha = 0.8$, which are typical values for tectonic events (Ogata, 1992). We apply them to the whole sequence for models E1 and E2 and use them as starting values for E3 - E5.

In addition to the fixed parameters, we list the free parameters for each model in Table 2.1. The more free parameters a model includes, the better its fit to past data should be; yet more parameters come at the cost of less robust models. To comparatively evaluate the model performances one would then have to resort to measures such as the Bayesian Information Criterion or Akaike Information Criterion which penalise models with more degrees of freedom. In our case we choose a different strategy that mimics prospective testing: Because each model forecasts the seismicity of the period $[t, t + 6hr]$ only with information obtained until time t , the forecast has zero degrees of freedom; therefore comparing the model likelihoods is sufficient.

CHAPTER 2. PROBABILITY-BASED MONITORING APPROACH FOR EGS

| Name | Type | Assumptions | Fixed Par. | # Free Par. |
|------|-------|---|---|--------------------------------------|
| R0 | R & J | Retrospective Two fitted periods No Update | $b = 1, c = 0.01 \text{ d}$ | 2 p, a |
| R1 | R & J | Generic Parameters No Update | $p = 0.91, a = -1.67$ $b = 1, c = 0.01 \text{ d}$ | 0 |
| R2 | R & J | Start with generic par. Update after six hours Increasing time window | $b = 1, c = 0.01 \text{ d}$ | 2 p, a |
| E1 | ETAS | Generic parameters | $p = 1.2, \alpha = 0.8$ $b = 1, c = 0.01 \text{ d}$ $c_f = 0$ | 2 K, μ |
| E2 | ETAS | Generic Parameters with flow rate | $p = 1.2, \alpha = 0.8$ $b = 1, c = 0.01 \text{ d}$ | 3 K, μ, c_f |
| E3 | ETAS | Start with generic par. Update after six hours | $b = 1, c_f = 0$ | 5 p, α, c K, μ |
| E4 | ETAS | Start with generic par. with flow rate | $b = 1$ | 6 p, α, c K, μ, c_f |
| E5 | ETAS | Start with generic par. flow rate with info from forecast bin | $b = 1$ | 6 p, α, c K, μ, c_f |

Table 2.1: Summary of the models and updating strategies used in the study. Model names are used in the text, the type indicates the base model. Main differing assumptions are indicated together with fixed / initial parameter values and free parameter values estimated from the sequence.

2.4.1 Modelling results

We compute forecasts of the seismicity for the eight models summarised in Table 2.1. For each model, we determine seismicity rates within six hours for a magnitude bin from $M_w = 0.9 - 3.5$ and compare them with observed events above $M_w \geq 0.9$. We start to forecast with the start of the fluid injection at 2.12.2006, 6pm, for a 6 hour time window and then successively update forecasts each 6 hours for a period of 15 days, summing up to 60 forecast windows.

The rate forecasts for all models in Figure 2.6 are shown compared to the observed seismicity indicated by the solid black line with circle markers. The top panel shows the three different Reasenberg and Jones models R0 to R2, the middle panel shows the ETAS model where flow rate was not included (E1 and E3) and the lowest panel shows the three ETAS models where flow rate was included in the modelling (E2, E4 and E5).

From a first visual inspection of Figure 2.6, we observe that model R1 underpredicts the rate of earthquakes during the intense injection period by more than a factor of 10, suggesting that an R&J model with generic parameters is not a suitable model to explain the induced sequence well. Model R0, which uses parameter values estimated retrospectively for the entire sequence for the co- and post-injection periods, demonstrates that if the ‘right’ set of parameters were known beforehand, an R&J model would be able to explain the seismicity well. Model R2, which updates the generic parameters every 6 hours, matches the seismicity rate much better than Model R1 in the co-injection period of the sequence; however, the model consistently overpredicts the post-injection seismicity of the sequence. This is similarly observed for model E1, an ETAS model using predefined parameters that are not updated during the forecasting experiment. Neither R1 nor E1 are able to respond adequately to the change of boundary conditions that occurs when the injection stops. Models E2-E5 fit the seismicity rate well based on a visual inspection.

2.4.2 Performance evaluation

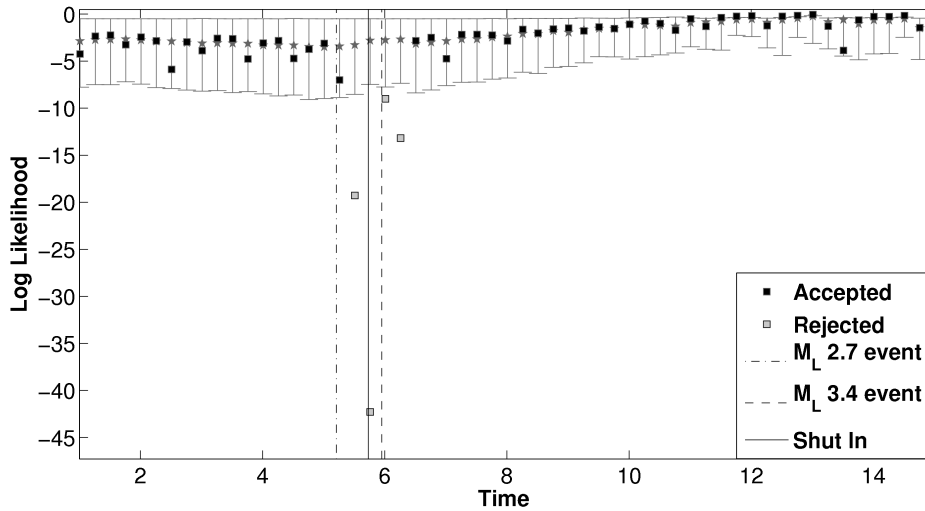


Figure 2.7: Log-likelihood values of the L-test for model E5 as a function of time. The panels display the mean and the 97.5 and 2.5 percentiles (grey dot and bars); days on which a log-likelihood value $LLS(t)$ is accepted are indicated with black squares; if the model is rejected, we indicate this with grey squares.

To quantitatively test the model forecasts in a pseudo-prospective approach, we use the N(umber)-test (Lombardi & Marzocchi, 2010; Schorlemmer et al., 2007, 2010; Werner et al., 2010; Woessner et al., 2011). This test compares the total forecast rates with the total number of observed earthquakes in the entire volume and indicates whether the too few or too many events are forecast or if the forecast is consistent with the observation. For example, if the model forecasts 0.5 events and 1 is observed, the cumulative Poisson distribution (PCDF) results in a quantile score of $\delta = PCDF(1, 0.5) = 0.910$. We reject the forecasts at the 0.05 significance level, thus for δ -values smaller than 0.025 and larger than 0.975. We determine the N-test for each six hour bin; the rejection ratio R_N denotes the percentage of test bins that are rejected.

In addition, we perform the L(ikelihood)-test (Schorlemmer et al., 2007, 2010). This test evaluates whether the forecast number of events and the distribution in the magnitude bins is consistent with the observation, again assuming the entire volume as one spatial bin. For each

magnitude bin we compute the log-likelihoods and sum this to a joint log-likelihood of the forecast. To verify that the joint log-likelihood is consistent with what is expected if the model is correct, we simulate 10,000 synthetic catalogues consistent with the forecast model and compute their log-likelihood values. This distribution of likelihood values is then compared with the observed log-likelihood. The quantile score γ then measures the amount of simulated log-likelihood values that are smaller than the observed log-likelihood. This test is one-sided and we reject a model if $\gamma < 0.025$ which implies that the observed log-likelihood is much smaller than expected if the model is true. According to the N-Test, we define the rejection ratio R_L that denotes the percentage of test bins that do not pass the L-test.

In Figure 2.7 we show the log-likelihoods for each six-hour bin of model E5. Bins, in which the observed log-likelihood falls within the 95%-confidence interval of the simulated values (grey error bars) are indicated by black squares; light grey squares denote bins in which the observed log-likelihood score falls outside the confidence limits. The rejection rate R_L for E5 is 0.15 (Table 2.2), therefore 9 bins out of 60 are rejected.

In addition, we calculate the joint log-likelihood of each model as a sum of over all time bins. Less negative joint log-likelihood indicate a better fit between model and data.

In Table 2.2 we summarise the scores of both tests and the joint log-likelihoods for each model. The joint log-likelihood confirms the visual inspection: The poorest model in terms of likelihood is R1, the best model in terms of the joint log-likelihood is model E5, closely followed by E4. However, none of the pseudo-prospective models reach the same likelihood as model R0, which is a retrospective fit to the entire sequence.

The models allow us to forecast the rate, or probability, of larger and potentially felt or damaging events. Figure 2.8 shows such a forecast as the probability of a $M_w \geq 2.0$, 3.0 and 4.0 events as a function of time for the next 6 hour period based on model E5. Probabilities of magnitudes above 2 are high from the start and decay to probability values of less than 0.5 only after the injection is finished. Probabilities for higher magnitudes such as 3 and 4 are smaller, but reach

| Name | Type | R_N | R_L | Joint Log Likelihood |
|------|--------------------|-------|-------|----------------------|
| R0 | Reasenberg & Jones | 0.33 | 0.17 | -170.85 |
| R1 | Reasenberg & Jones | 0.73 | 0.60 | -1433.77 |
| R2 | Reasenberg & Jones | 0.54 | 0.54 | -846.79 |
| E1 | ETAS | 0.65 | 0.63 | -478.11 |
| E2 | ETAS | 0.48 | 0.2 | -266.67 |
| E3 | ETAS | 0.43 | 0.35 | -276.19 |
| E4 | ETAS | 0.42 | 0.20 | -204.35 |
| E5 | ETAS | 0.40 | 0.15 | -204.33 |

Table 2.2: Quantitative evaluation of model forecasts: Model name, model type, fraction of rejected time bin in N-Test, fraction of rejected time bins in L-Test, and joint log-likelihood of the each model.

0.51 and 0.07 nonetheless.

2.4.3 Translating forecast rates to time-varying seismic hazard

The forecast rates for each magnitude bin of each model are the basic input needed to produce a time-dependent hazard model. We convert rates into probabilities of a given ground motion intensity, using standard procedures introduced originally by Cornell (1968). Hazard is the result of a combination of seismic rates, their frequency–size distribution and the Ground Motion Prediction Equation (GMPE) and its uncertainty. In contrast to the standard hazard assessment, which is computed for recurrence periods of hundreds to thousands of years, we are here interested in short term hazard in the order of hours to days. This is identical to the time-dependent hazard assessment introduced for aftershocks sequences by Wiemer (2000) and used in California (Gerstenberger et al., 2005). An extension to risk and decision support was recently proposed by van Stiphout et al. (2010).

To adapt the ground motion forecast to for Switzerland, we adjust the attenuation relation according to Fäh et al. (2003), expressed in the European Macroseismic Scale intensity (EMS).

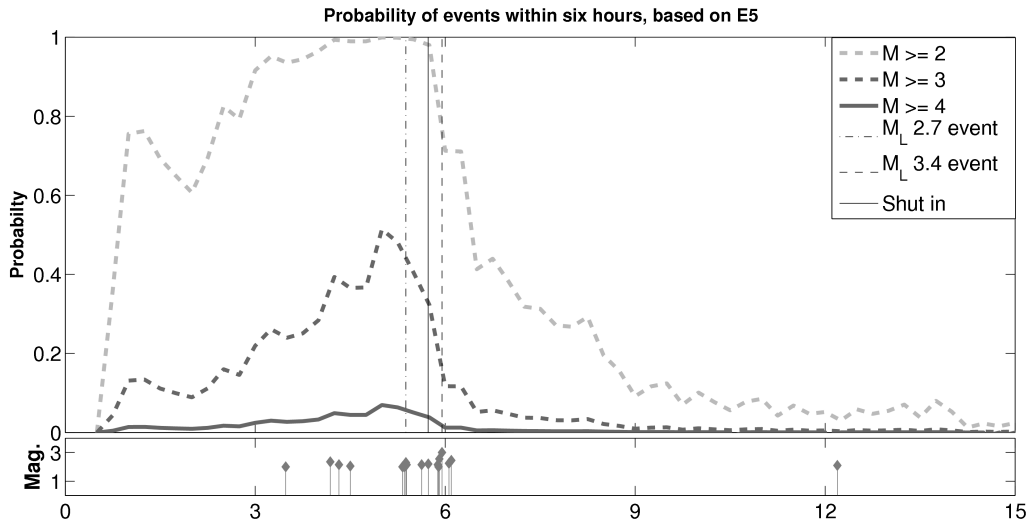
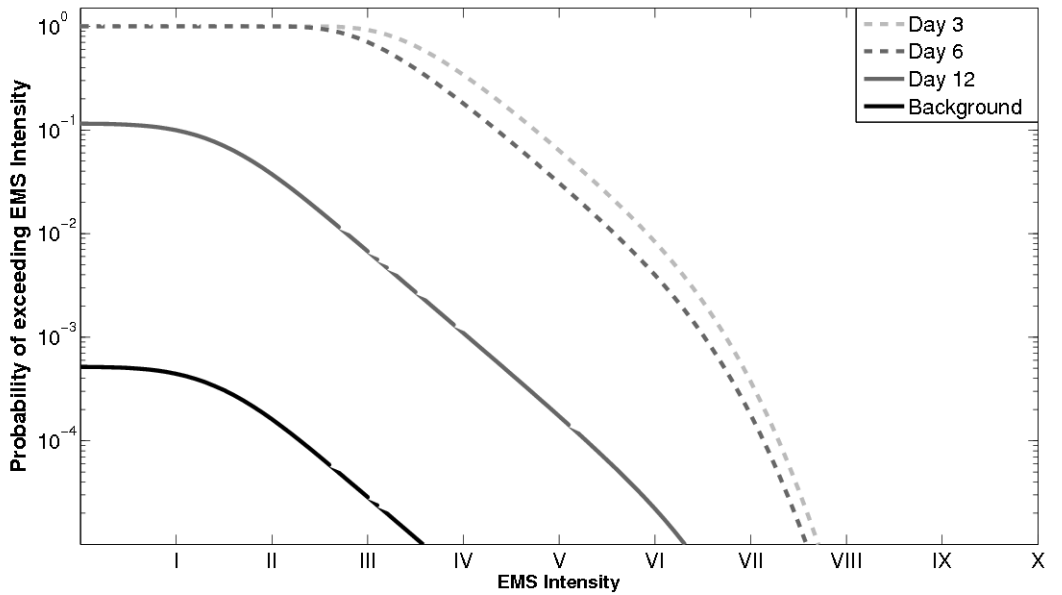


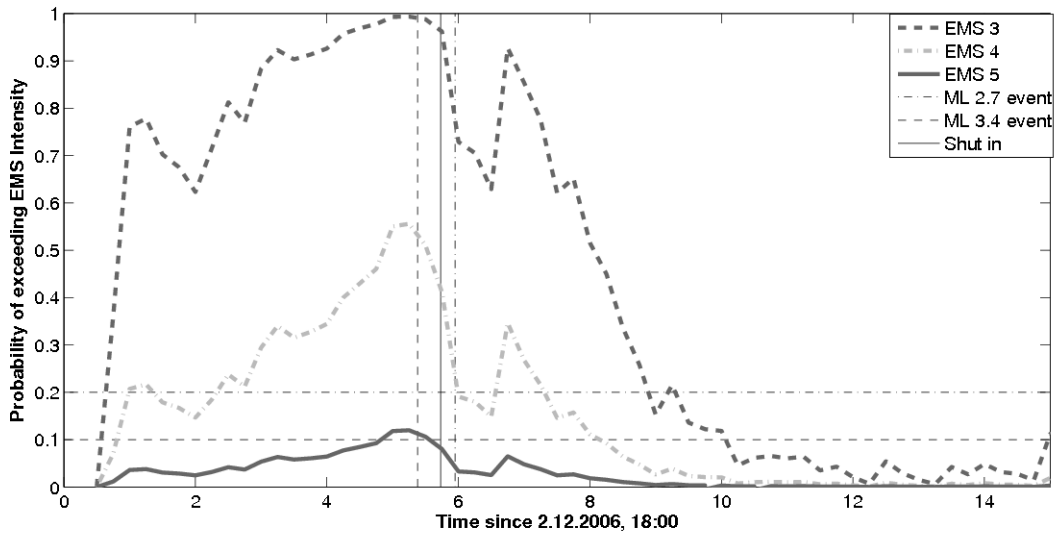
Figure 2.8: Probabilities for events within the next six hours for magnitudes \geq to 2, 3 and 4 with time, based on model E5. Observed events above magnitude 2 are indicated in the lower panel.

We integrate the hazard from $M_W \geq 2.5$ upward. The maximum magnitude, M_{max} , that is used in the induced hazard is another critical factor; it determines the roll-off at higher intensities. As an initial estimate we choose a somewhat arbitrary value of $M_W = 5.0$; however, we show the effect of a different maximum magnitude later.

Each model can then be translated into a hazard curve for the next 6 hour period. Figure 2.9a shows three typical examples of hazard curves, at three different times (day three, day six and day twelve), the background hazard curve is also indicated. The hazard during the intense induced sequence exceeds the background by a factor of more than 100. To visualise the evolution of the hazard as a function of time, we show the probability of exceeding EMS intensities III, IV and V for model E5 as a function of time in Figure 2.9b. EMS intensity III is the level at which a few people start feeling a light shaking indoors, an event with intensity IV is already felt by many indoors and intensity V is felt by most indoors and the vibration is strong (Gruenthal, 1998). The exceedance probabilities reach levels of 0.2 for EMS III and



a



b

Figure 2.9: Hazard curves based on model E5. (a) Probabilities of exceeding EMS Intensities I to X for three different times, (1) day three, (2) day six and (3) day twelve after the start of water injection. All three curves are based on $M_{max} = 5$. (b) Probabilities of exceeding EMS intensities III, IV and V within the next six hours for the first 15 days. Indicated are also the times of the two largest events during the first 15 days and the time of the termination of water injection.

IV already on day 1. A probability level of 0.1 is reached on day 4 for EMS intensity V. The maximum probability levels are 0.99, 0.55 and 0.12 for EMS intensity III, IV and V, respectively. All three maximum levels are reached after five days and six hours, i.e. before water injection was stopped and before the largest event occurred.

2.5 Discussion and Conclusion

The ultimate termination of the Basel EGS pilot study due to the public outcry as a consequence of the sequence of strongly felt earthquakes poses a substantial challenge for future EGS systems. In hindsight, it is obvious that the potential for triggering felt earthquakes was underestimated by GEL, as well as by the regulatory bodies. However, even today, more than three years after the main injection, scientists are not able to accurately forecast the response of a rock volume to the injection of water at high pressures, nor are there universally accepted guidelines for hazard and risk assessment prior, during, and after a stimulation. We see our study as a contribution towards an improved ability to forecast induced seismicity as it unfolds.

The seismicity recorded during and after the stimulation of the Basel EGS is one of the best monitored sequences of its kind. Our analysis of the monitoring completeness as a function of time (Figure 2.3) shows that $M_c(t)$ varies between 0.5 and 0.9. Higher values of M_c are typical during the first hours of intense aftershocks sequences, when the coda of larger events mask the smaller ones (e.g., Woessner & Wiemer, 2005). We suspect that the temporal changes in M_c (Figure 2.3) are caused by the same mechanism. In addition, it is possible that $M_c(t)$ changes as a result of temporal changes in the activity areas: If areas of a higher M_c (i.e., further away from the sensors) are more active, the overall M_c will appear to increase.

Our analysis of the decaying part of the sequence reveals that once the injection stopped, the decay can be well described using the Omori-Utsu law of aftershocks decay (Figure 2.5). The comparison between model and data passes the Kolmogorov-Smirnov test, which in our expe-

rience is a rather strict test for compliance to aftershock seismicity (Conover, 1972; Woessner et al., 2004). From a statistical viewpoint, there is nothing special about the sequence, which is consistent with the conclusion by Deichmann & Giardini (2009) that the earthquakes induced by the reservoir stimulation below Basel, rather than representing a case of hydrofracturing, occurred mainly as shear dislocation on pre-existing faults that were triggered by the increase in pore pressure due to the injected water, but driven by the ambient tectonic stress. In addition, we suggest that an unknown fraction of the events are not directly triggered by the change in pore pressure but rather indirectly as ‘aftershocks’ to other events, or as ‘daughter events’ in a cascading model.

Our assessment that the seismicity will take about 31+29/-14 years to decay to the background is consistent with the observations of aftershock sequences (Stein & Liu, 2009) as well as with predictions of laboratory studies (Dieterich, 1994). In aftershock sequences, the duration of the sequences, defined as the time when the rate returns to that before the event, has been proposed to be inversely correlated with the tectonic loading rate. The rate and state model of fault friction, which predicts changes in fault properties after earthquakes, and which is commonly used for aftershock studies (Dieterich, 1994), predicts an aftershock duration of

$$t_a = \frac{A\sigma}{\dot{\tau}} \quad (2.11)$$

where $\dot{\tau}$ is the rate of shear stressing on the fault, σ is the normal stress, and A is a constitutive parameter. Although the stressing rate is hard to measure, it is roughly proportional to the loading rate. The loading rate in Switzerland, and also in the Basel region is known to be low (< 1 mm/yr) and aftershock sequences are therefore expected to last longer than in tectonically more active regions.

The major unknown in the estimation of the aftershock duration is the local background rate. Ideally, monitoring at a comparable completeness level of the same rock volume for several years

would establish the background seismicity rate. This approach is prohibitively expensive. We chose the regional background rate, extrapolated from the micro-seismicity record, as a proxy, but the local variability of the background at the scale of one kilometre is unknown. Supporting evidence for a low background rate comes from the observation that micro-earthquakes in the past three years have been confined to the induced volume, no events have been detected outside the well-defined volume shown also in Figure 2.2, although the network of borehole sensors in principle would be able to detect them.

Our focus of modelling the rates of the micro-seismicity is on two largely statistical models, the Reasenberg and Jones approach (Reasenberg & Jones, 1989) and the ETAS model (Hainzl & Ogata, 2005; Ogata, 1988) . There are a number of reasons why we consider these models suitable alternatives to more physics-based modelling approaches (Baisch et al., 2009b; Kohl & Megel, 2007; Shapiro et al., 2010, 2007):

- Catalogue data of the micro-seismicity used for forecasting is, at least in principle, readily available in near-real time, a requirement for building a real-time hazard assessment system.
- Statistical models are well understood and well tested, because they are used commonly to model the behaviour of aftershocks and swarms (Hainzl & Ogata, 2005; Ogata, 1988; Reasenberg & Jones, 1989; Woessner et al., 2010).
- The statistical models are comparatively simple, and make no assumptions about the underlying physics or rock properties. They can therefore be considered as starting models, while more refined models should be used for forecasting only if shown to be superior in their ability to forecast the seismicity.
- The models output a seismicity rate forecast which can be converted to time-dependent hazard estimates: both of these outputs can readily be implemented as measure for

decisions on continuing an EGS experiment. This is not easily performed with physics-based models without introducing additional stochasticity (Cocco et al., 2010; Hainzl et al., 2009; Woessner et al., 2010).

One of our major objectives was to define a more quantitative alternative to the traffic-light system used so far in the monitoring and regulation of EGS creation (Bommer et al., 2006). Based on our findings here we propose that such a system would be built using a model such as E5 applied in real time, and translating the rates into hazard. This implies that first of all, a suitable real-time monitoring system must exist that, within minutes, can deliver reliable locations and magnitudes for the dozens to hundreds of events that can occur during stimulation every hour. It also implies that beforehand, a plan of action must be agreed upon that specifies the actions to take once a certain hazard threshold is reached. Models such as E5, which integrates the flow rate, can be used to forecast the expected hazard if a certain flow rate is applied in the hours and days to come; they can thus not only be used from a regulatory point of view, but also assist the operators in their decision making. The approach we propose here is, in our assessment, a substantial advance when compared to the traffic-light system, because:

- Not only a single magnitude of one larger event counts, but also the many small ones that occur. Including these small events for forecasting and decision making increases the robustness.
- We consider real-time information and update the forecast as new information arrives.
- Our model has been tested in a pseudo-prospective sense and also works well at regional and local scale for natural seismicity.
- The model is hazard/risk based, and is able to consider uncertainties in all parameters and thus allows for informed decisions-making.

- Our model can be used to simulate alternative stimulation strategies and their implications for future seismicity; by assuming different parameter values in these simulations, adequate modelling of different tectonic environments in terms of their productivity can be achieved.

Translating the forecast rates into seismic hazard is a straightforward calculation, and has been already implemented successfully at local and regional scale (e.g., Gerstenberger et al., 2005, 2007). It was also applied in the Basel risk study (Baisch et al., 2009a). We believe that this translation should be an integral part of a future monitoring and regulatory framework, because it allows to set thresholds that are hazard/risk based and fully probabilistic by definition. We anticipate that the underlying forecast models will become increasingly complex, and ensemble forecasting or logic trees will be considered just like they are in weather forecasting or probabilistic seismic hazard assessment. By translating all forecast rates, and their uncertainties, into hazard, taking into account the uncertainties in the expected ground motions, seismologists have combined the best of their knowledge into (comparatively) simple numbers. The hazard integration then takes care of integrating all magnitude bins, as well as the fact that sometimes smaller events can create larger than to be expected ground motions.

Further adding knowledge on the fragility of buildings, and translating into time-dependent risk, is then the next logical step, also already a part of the SERIANEX study (Baisch et al., 2009a). van Stiphout et al. (2010) introduced time-dependent risk assessment at a local scale by analysing the seismicity in the L'Aquila region. It is entirely possible to compute a threshold, for example, of a 1 % probability of exceeding damages of CHF 10 million or more, or not exceeding a 10% annual probability of causing a casualty. Therefore, such a threshold will be an integral part of any insurance scheme implemented for EGS systems. We believe that EGS technology and the associated clean energy does not come without a risk, as it is the case for almost any other technology. As scientists we strive to describe and reduce the risk. The

decision on how much risk to take – essentially where to set a threshold in our Figure 2.9b – is ultimately a political process. We see our paper in this context as a contribution toward building robust, and community-accepted, forecast models.

One of the major ‘free’ parameters of such a model is the maximum possible magnitude, M_{max} , used in the hazard calculation. There is very little knowledge how to set this number. Contemporary PSHA studies tend to set a larger M_{max} than applied in both our study and SERIANEX. The underlying question is wide open: Does the intense activity during stimulation also increase the probability of triggering an event with source dimensions significantly larger than the stimulated volume? The conservative answer to this question taken in regional time-dependent hazard assessment is that all earthquakes are treated equally, such that triggering is possible all the way to the regional M_{max} , which in the case of Switzerland is set between around 6 and 7.5 (Wiemer et al., 2009). Choosing a higher M_{max} will increase the hazard at higher ground motions, but may not be the critical factor in reaching an action threshold because already moderate events of M 3–4, with source dimensions well within the induced volume, can cause large enough ground motions to create non-structural damage. We show the effect of three different M_{max} : (1) 3.7 which was used by Baisch et al. (2009a) for the Basel risk study, (2) 5, which was used for this study and (3) 7, which is the maximum magnitude of the seismic zone of Basel in Figure 2.10a. We show the time evolution for these three M_{max} for two different EMS intensities III and V. While the probabilities for the lower intensity and higher probabilities practically overlap, we see a higher differentiation for the higher intensity. The inset in Figure 2.10a shows a snapshot of the probabilities for different M_{max} at day three (indicated by a dashed line). The curve with the smallest M_{max} drops off the fastest while the other two only begin to drop of at EMS intensities VI and VIII, respectively.

Another factor that we have not yet discussed is the influence of the b -value. We assume a constant b -value of 1 for all of our models. As we do not test for different magnitude bins, it has no influence there. However, the b -value has an influence on the hazard integration. In Figure

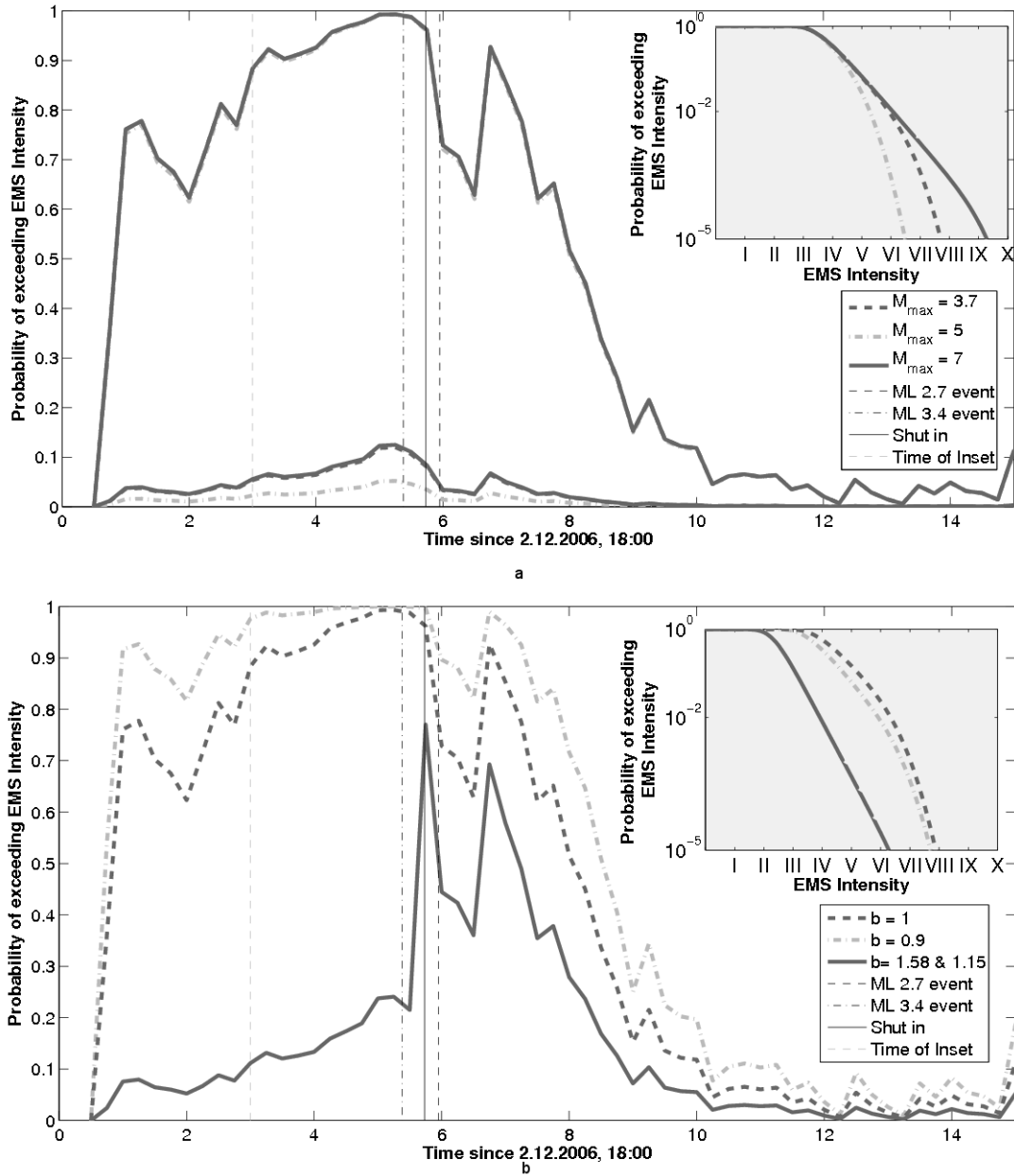


Figure 2.10: (a) Effect of different maximum magnitudes with (1) $M_{max} = 3.7$, (2) $M_{max} = 5$ and (3) $M_{max} = 7$. Higher probabilities show the probabilities of exceeding EMS intensity III, lower probabilities the exceedance probabilities for EMS V. The inset marks a hazard snapshot for day three (indicated by a light grey dashed line). (b) Effect of different b -values on the hazard integration with (1) $b = 0.9$, (2) $b = 1$ and (3) $b = 1.58$ for co-injection and 1.15 for post-injection events. The inset shows again a hazard snapshot for day three.

2.10b we show the time evolution of the hazard for three different assumptions: (1) b -value of 1, as in this study, (2) b -value of 0.9 as the seismogenic source zone of Basel (Giardini et al., 2004; Wiemer et al., 2009) and (3) b -values of 1.59 for co-injection and 1.15 for post-injection events, respectively, as we find for this dataset (compare Fig. 2.4). The inset shows, similar as in Figure 2.10a, a snapshot of the hazard for different EMS intensities at day three. The hazard is strongly reduced with higher b values and increases as this value decreases. However, for this study we fixed the b -value at 1, as the values of the whole sequence can not be justified for a real-time approach as they are only known posteriori. For all curves in Figure 2.10a we use a b -value of 1 and for all curves in Figure 2.10b we use a M_{max} of 5.

We show here the importance of quantitative testing of a model performance. We apply tests defined by the international Collaboratory for the Study of Earthquake Predictability (CSEP, www.cseptesting.org). Work on induced seismicity, can in our opinion, benefit substantially from CSEP, for example by using the community-accepted testing algorithms, such as the N- and L-test employed here, and by exploiting the models tested within CSEP. Both the R&J and ETAS models are currently being tested in fully prospective tests in a variety of testing regions (Schorlemmer et al., 2010). Additional, pseudo-prospective tests of models at the more local scale of aftershock sequences have been performed recently as an extension of the CSEP concept (Cocco et al., 2010; Hainzl et al., 2009; Woessner et al., 2010), which again offer highly relevant insights for modelling the induced seismicity. Reciprocally, the CSEP process can in our opinion also benefit from the work on induced sequences, because it offers the possibility to evaluate and improve modelling and testing within a reasonably well constrained environment. The testing applied in our study reveals that a fully retrospective matching of a sequence and a model forecast is misleadingly successful. Model R0, a rather simple model, offers the best fit to the data both in terms of N and L-test. It passes as an accepted model and is not rejected by the tests at the 5% significance levels. However, the same model, when applied in a pseudo-prospective sense (R2), performs quite poorly when compared to other models.

This illustrates that the pseudo-prospective approach applied by us, which recreates a real-time setup, is needed in order to achieve a less biased assessment of the forecasting ability of models. We suggest the rigorous testing approach applied in this study has been lacking so far in the evaluation of models for induced seismicity, and that future studies that propose methods for modelling induced seismicity should choose similar quantitative approaches.

From the testing results (Table 2.2), it is clear that ETAS class models in general perform better than R&J models. This finding is consistent with the current assessment of these models in various testing regions and pseudo-respective testing on aftershock sequences. The performance difference in our case may in fact be more substantial, because of the extreme conditions of very high rates and the dramatic change of process at the termination of the injection. The R&J model R2 is not able to adjust its forecast sufficiently at the end of the injection, and subsequently overpredicts the rates. The ETAS models, which differentiate between a background rate and a term of induced events, are much better able to adjust to this change. The ETAS formulation allows us also to specifically consider the induced flow rate, which is not possible for R&J. Including the flow rate does indeed substantially improve the model performance.

More work is needed to define a community-accepted real time system alternative to the traffic-light system. For example, our findings here should be applied consistently to a number of induced sequences to check if the results are robust. Does model E5 always provide the best fit? In addition, it is possible that the forecasting ability can be further improved if the spatial variability of micro-seismicity is better understood. Of course we also need to test more physics-based models in comparison to the statistical ones – yet these models need to provide pathways to generate seismicity rates.

One question that remains unsolved is whether the Basel EGS experiment would have been successful if our model E5 were applied for the real-time decision-making. Could we have prevented an event felt by the public and continued the experiment until reservoir creation? We see in Figure 2.9b that probabilities of exceeding EMS Intensity 3 already reached 20 % after

one day and 50 % after 2.5 days. Probabilities of exceeding EMS 5 also reached a level of 0.1 after less than 4.5 days. So by choosing any of these arbitrary thresholds, action would have been taken more than one day before the actual termination of the water injection on December 6, 2006 11:33 a.m. These questions remains unsolved until a future application and the a priori agreed schedule of decisions.

Acknowledgements We would like to thank Geothermal Explorers Ltd., who provided seismicity and injection data without which this work would not have been possible. This study is part of the project GEOTHERM, funded by the Competence Center of Environment and Sustainability (CCES) of ETH (<http://www.cces.ethz.ch/projects/nature/geotherm/>). We thank T. Kraft, G. de Souza and J. Zechar for valuable comments on the manuscript.

References

- Baisch, S., Carbon, D., Dannwolf, U., Delacou, B., Devaux, M., Dunand, F., Jung, R., Koller, M., Martin, C., Sartori, M., Secanell, R., & Vörös, R., 2009a. Deep heat mining basel - seismic risk analysis, Tech. rep., Serianex.
- Baisch, S., Vörös, R., Rothert, E., Stang, H., Jung, R., & Schellschmidt, R., 2009b. A numerical model for fluid injection induced seismicity at soultz-sous-forets, *International Journal of Rock Mechanics and Mining Sciences*, **47**(3), 405–413.
- Baisch, S., Vörös, R., Weidler, R., & Wyborn, D., 2009c. Investigation of Fault Mechanisms during Geothermal Reservoir Stimulation Experiments in the Cooper Basin, Australia, *Bull. Seismol. Soc. Am.*, **99**(1), 148–158.
- Bethmann, F., Deichmann, N., & Mai, M., 2007. Moment Magnitude. In: Evaluation of the induced seismicity in Basel 2006/2007: locations, magnitudes, focal mechanisms, statistical forecasts and earthquake scenarios, Tech. rep., Report of the Swiss Seismological Service to Geopower Basel AG, Basel, Switzerland.
- Bommer, J. J., Oates, S., Cepeda, J. M., Lindholm, C., Bird, J., Torres, R., G-Marroquin, & Rivas, J., 2006. Control of hazard due to seismicity induced by a hot fractured rock geothermal project, *Engineering Geology*, **83**(4), 287–306.
- Cocco, M., Hainzl, S., Catalli, F., Enescu, B., Lombardi, A. M., & Woessner, J., 2010. Sensitivity study of forecasts based on Coulomb stress calculation and rate-state frictional response, *J. Geophys. Res. - Solid Earth*, **115**(B05307).
- Conover, W. J., 1972. A Kolmogorov Goodness-of-Fit Test for Discontinuous Distributions, *Journal of the American Statistical Association*, **67**(339), 591–596.
- Cornell, C., 1968. Engineering seismic risk analysis, *Bull. Seismol. Soc. Am.*, **59**(5), 1583–1606.
- Deichmann, N. & Ernst, J., 2009. Earthquake focal mechanisms of the induced seismicity in 2006 and 2007 below Basel (Switzerland), *Swiss J. Geosci*, **102**, 457–466.

REFERENCES

- Deichmann, N. & Giardini, D., 2009. Earthquakes Induced by the Stimulation of an Enhanced Geothermal System below Basel (Switzerland), *Seismol. Res. Letts.*, **80**(5), 784–798.
- Dieterich, J., 1994. A constitutive law for rate of earthquake production and its application to earthquake clustering, *J. Geophys. Res. - Solid Earth*, **99**(B2), 2601–2618.
- Dyer, B., Schanz, U., Ladner, F., Häring, M., & Spillman, T., 2008. Microseismic imaging of a geothermal reservoir stimulation, *The Leading Edge*, pp. 856–869.
- Fäh, D., Giardini, D., Bay, F., Bär, M., Bernardi, F., Braunmiller, J., Deichmann, N., Furrer, M., Gantner, L., Gisler, M., Isenegger, D., Jimenez, M. J., P.Kästli, Koglin, R., Masciadri, V., Rutz, M., Scheidegger, C., Schibler, R., Schorlemmer, D., Schwarz-Zanetti, G., Steimen, S., Sellami, S., Wiemer, S., & Woessner, J., 2003. Earthquake catalog of Switzerland (ECOS) and the related macroseismic database, *Eclogae Geologicae Helveticae*, **96**(2), 219–236.
- Felzer, K., Becker, T., Abercrombie, R., Ekstrom, G., & Rice, J., 2002. Triggering of the 1999 M-W 7.1 Hector Mine earthquake by aftershocks of the 1992 M-W 7.3 Landers earthquake, *J. Geophys. Res. - Solid Earth*, **107**(B9).
- Field, E. H., 2007. Overview of the Working Group for the Development of Regional Earthquake Likelihood Models (RELM), *Seismol. Res. Letts.*, **78**(1), 7–15.
- Gerstenberger, M., Wiemer, S., Jones, L., & Reasenber, P., 2005. Real-time forecasts of tomorrow's earthquakes in California, *Nature*, **435**, 328–331.
- Gerstenberger, M. C., Jones, L. M., & Wiemer, S., 2007. Short-term aftershock probabilities: Case studies in California, *Seismol. Res. Letts.*, **78**(1), 66–77.
- Giardini, D., 2009. Geothermal quake risks must be faced, *Nature*, **461**, 848–849.
- Giardini, D., Wiemer, S., D.Fah, & Deichmann, N., 2004. Seismic hazard assessment of Switzerland, 2004, Tech. rep., Swiss Seismological Service, ETH Zurich.
- ed. Gruenthal, G., 1998. *European Macroseismic Scale 1998 (EMS-98)*, Cahiers du Centre Europeen de Geodynamique et de Seismologie 15.
- Gutenberg, B. & Richter, C. F., 1942. Earthquake magnitude intensity, energy, and acceleration, *Bull. Seismol. Soc. Am.*, **32**, 163–191.
- Hainzl, S. & Ogata, Y., 2005. Detecting fluid signals in seismicity data through statistical earthquake modeling, *J. Geophys. Res. - Solid Earth*, **110**(B05S07).
- Hainzl, S., Enescu, B., Catalli, F., Cocco, M., Wang, R., Roth, F., & Woessner, J., 2009. Aftershock modeling based on uncertain stress calculations, *J. Geophys. Res. - Solid Earth*, **114**(B05309).

REFERENCES

- Häring, M. O., Schanz, U., Ladner, F., & Dyer, B., 2008. Characterisation of the Basel 1 enhanced geothermal system, *Geothermics*, **37**(5), 469–495.
- Kohl, T. & Megel, T., 2007. Predictive modeling of reservoir response to hydraulic stimulations at the European EGS site Soultz-sous-Forets, *International Journal of Rock Mechanics and Mining Sciences*, **44**(8), 1118–1131.
- Kraft, T., Mai, P., Wiemer, S., Deichmann, N., Ripperger, J., Kästli, P., Bachmann, C., Fäh, D., Woessner, J., & Giardini, D., 2009. Enhanced geothermal systems in urban areas - lessons learned from the 2006 basel ml 3.4 earthquake, *EOS*, **32**(90), 273–274.
- Lombardi, A. M. & Marzocchi, W., 2010. The Assumption of Poisson Seismic-Rate Variability in CSEP/RELM Experiments, *Bull. Seismol. Soc. Am.*, **100**(5A), 2293–2300.
- Ogata, Y., 1988. Statistical-models for earthquake occurrences and residual analysis for point-processes, *Journal of the American Statistical Association*, **83**(401), 9–27.
- Ogata, Y., 1992. Detection of precursory relative quiescence before great earthquakes through a state model, *J. Geophys. Res.*, **97**(B13), 19845–19871.
- Ogata, Y., 1999. Seismicity analysis through point-process modeling: a review, *Pure appl. geophys.*, **155**, 471–507.
- Reasenber, P. & Jones, L., 1989. Earthquake hazard after a mainshock in california, *Science*, **243**(4895), 1173–1176.
- Reasenber, P. & Jones, L., 1990. California aftershock hazard forecasts, *Science*, **247**(4940), 345–346.
- Reasenber, P. & Jones, L., 1994. Earthquake aftershocks – update, *Science*, **265**(5176), 1251–1252.
- Ripperger, J., Kästli, P., Fah, D., & Giardini, D., 2009. Ground motion and macroseismic intensities of a seismic event related to geothermal reservoir stimulation below the city of basel - observations and modeling, *Geophys. J. Int.*, **3**(179), 1757–1771.
- Schorlemmer, D., Gerstenberger, M. C., Wiemer, S., Jackson, D., & Rhoades, D. A., 2007. Earthquake likelihood model testing, *Seismol. Res. Letts.*, **87**, 17–29.
- Schorlemmer, D., Zechar, J. D., Werner, M. J., Field, E. H., Jackson, D. D., Jordan, T. H., & Group, T. R. W., 2010. First results of the regional earthquake likelihood models experiment, *Pure appl. geophys.*, **167**(8-9), 859–876.
- Shapiro, S., Dinske, C., Langenbruch, C., & Wenzel, F., 2010. Seismogenic index and magnitude probability of earthquakes induced during reservoir fluid stimulations, *Leading Edge*, **29**(3), 304–9.

REFERENCES

- Shapiro, S. A. & Dinske, C., 2009. Fluid-induced seismicity: Pressure diffusion and hydraulic fracturing, *Geophysical Prospecting*, **57**(2), 301–310.
- Shapiro, S. A., Dinske, C., & Kummerow, J., 2007. Probability of a given-magnitude earthquake induced by a fluid injection, *Geophys. Res. Lett.*, **34**(22).
- Smith, M., 1983. A history of hot dry rock geothermal energy systems, *Journal of Volcanology and Geothermal Research*, **15**(1-3), 1–20, Geothermal Energy of Hot Dry Rock.
- Stein, S. & Liu, M., 2009. Long aftershock sequences within continents and implications for earthquake hazard assessment, *Nature*, **461**(7269), 87–9.
- Tenzer, H., 2001. Development of hot dry rock technology, *Geo-Heat Center Quarterly Bulletin*, **22**(4).
- Utsu, T., 1961. A statistical study on the occurrence of aftershocks, *Geophys Mag.*, **30**, 521–605.
- van Stiphout, T., Wiemer, S., & Marzocchi, W., 2010. Are short-term evacuations warranted? Case of the 2009 L'Aquila earthquake, *Geophys. Res. Lett.*, **37**(L06306).
- Werner, M., Zechar, J. D., Marzocchi, W., Wiemer, S., & CSEP-Italy Working Grp, 2010. Retrospective evaluation of the five-year and ten-year CSEP-Italy earthquake forecasts, *Annals of Geophysics*, **53**(3), 11–30.
- Wiemer, S., 2000. Minimum magnitude of complete reporting in earthquake catalogs: examples from Alaska, the Western United States, and Japan, *Bull. Seismol. Soc. Am.*, **90**, 859–869.
- Wiemer, S., 2000. Introducing probabilistic aftershock hazard mapping, *Geophys. Res. Lett.*, **27**(20), 3405–3408.
- Wiemer, S., 2001. A software package to analyze seismicity: Zmap, *Seismol. Res. Letts.*, **72**, 373–382.
- Wiemer, S., Giardini, D., Fäh, D., Deichmann, N., & Sellami, S., 2009. Probabilistic seismic hazard assessment for Switzerland: best estimates and uncertainties, *J. of Seismology*, **13**(4), 449–478.
- Woessner, J., 2005. *Correlating Statistical Properties of Aftershock Sequences to Earthquake Physics*, Ph.D. thesis, ETH Zurich.
- Woessner, J. & Wiemer, S., 2005. Assessing the quality of earthquake catalogues: Estimating the magnitude of completeness and its uncertainty, *Bull. Seismol. Soc. Am.*, **95**(2), 684–698.
- Woessner, J., Hainzl, S., Marzocchi, W., Werner, M. J., Lombardi, A. M., Catalli, F., Enescu, B., Cocco, M., Gerstenberger, M. C., & Wiemer, S., 2011. A Retrospective Comparative Test for the 1992 Landers Sequence, *J. Geophys. Res.*, **116**(B05305).

REFERENCES

- Woessner, J., Hauksson, E., Wiemer, S., & Neukomm, S., 2004. The 1997 Kagoshima (Japan) earthquake doublet: A quantitative analysis of aftershock rate changes, *Geophys. Res. Lett.*, **31**(3).
- Woessner, J., Christophersen, A., Zechar, J. D., & Monelli, D., 2010. Building self-consistent, short-term earthquake probability (STEP) models: improved strategies and calibration procedures, *Annals of Geophysics*, **53**(3), 141–154.
- Wohlenberg, J. & Keppler, H., 1987. Monitoring and interpretation of seismic observations in hot dry rock geothermal energy systems, *Geothermics*, **16**(4), 441–445.
- Zechar, J. D., Schorlemmer, D., Liukis, M., Yu, J., Euchner, F., Maechling, P. J., & Jordan, T. H., 2010. The Collaboratory for the Study of Earthquake Predictability perspective on computational earthquake science, *Concurrency and Computation: Practice and Experience*, (22), 1836–1847.

Chapter 3

Influence of pore pressure on the event size distribution of induced earthquakes¹

Corinne E. Bachmann, Stefan Wiemer, Jochen Woessner and Bettina P. Goertz-Allmann

¹Submitted *Nature Geoscience* as C.E. Bachmann, S.Wiemer, B.P. Goertz-Allmann and J. Woessner *Influence of the pore pressure on the event size distribution of induced earthquakes*

Abstract

During an enhanced geothermal system (EGS) experiment, fluid is injected at high pressure into crystalline rock, to enhance its permeability and thus create a reservoir from which geothermal heat can be extracted. The fracturing of the basement caused by these high pore-pressures is associated with microseismicity. However, the relationship between the magnitudes of these induced seismic events and the applied fluid injection rates, and thus pore-pressure, is unknown. Here we show how pore-pressure can be linked to the seismic frequency–magnitude distribution, described by its slope, the b -value. We evaluate the dataset of an EGS in Basel, Switzerland and compare the observed event-size distribution with the outcome of a minimalistic model of pore-pressure evolution that relates event-sizes to the differential stress σ_D . We observe that the decrease with distance of the injection point of b -values is likely caused by a decrease in pore-pressure. This leads to an increase with distance and time of the probability of a large magnitude event.

3.1 Discussion

Enhanced Geothermal Systems (EGS) represent a promising alternative for clean energy. For such systems, two boreholes are drilled to depths of below 3 km into the basement, between which a fluid, typically water, is circulated to extract the heat at temperatures well above 100°C. The fluid is pumped at high pressure into the first borehole, to increase the permeability of the rock; a process called reservoir stimulation. This process is accompanied by thousands of micro-earthquakes, their hypocenters reveal critical information about the ongoing evolution of the reservoir. Few events eventually happen to be large enough to be felt at the surface, creating nuisance for the population or even damage to the building stock. The seismic hazard and risk associated with the induced seismicity is in some cases, such as for the EGS project

beneath the city of Basel (Switzerland), estimated as too high to be acceptable for society (Baisch et al., 2009). Induced seismicity is currently the largest obstacle to the widespread installation of EGS systems near urban centers (Giardini, 2009). Enhancing our understanding of the physical processes that control the generation of induced seismicity is therefore an urgent scientific challenge.

The basic principles of pore-pressure induced seismicity are well understood: the increase in pore-pressure decreases the normal stress on the rock volume, resulting in a lower effective stress. The failure releases pre-existing tectonic stresses with the consequence of nucleating sudden slip – in other words, micro-earthquakes. However, the current statistical, physical and numerical models of induced seismicity cannot sufficiently explain – let alone forecast – the critical parameters that ultimately control seismic hazard and risk, i.e. the scaling of earthquake sizes, the temporal occurrence of events, the amount of induced seismicity and the maximum possible magnitude. To investigate the physical processes controlling these parameters, we analyse the seismicity related to the EGS experiment conducted in Basel in December 2006. The seismicity induced during the experiment was closely monitored by a six-sensor borehole array (see Figure 3.1a), which recorded over 11,000 events of which over 3,500 could be located (Haering et al., 2008). The recorded events range from moment magnitudes M_w 0.1 to 3.2, with three events above M_w 3 (occurring 0.22, 38 and 55 days after the termination of the injection). Today, seismicity at the site is still slightly above the assumed long-term background, its decay being indistinguishable from a typical aftershock sequence (Bachmann et al., 2011).

In the following, we analyse the space–time evolution of the relative earthquake size distribution of the induced earthquakes in Basel. The cumulative number of earthquakes, N , in a given volume generally follows a power law distribution and can be expressed as (Gutenberg & Richter, 1942) $\log N = a - bM$ (1), where a and b are constants that describe the productivity and the relative size distribution, respectively. Higher b -values indicate more small events relative to larger events and vice versa. Equation (1) and slight modifications thereof are used

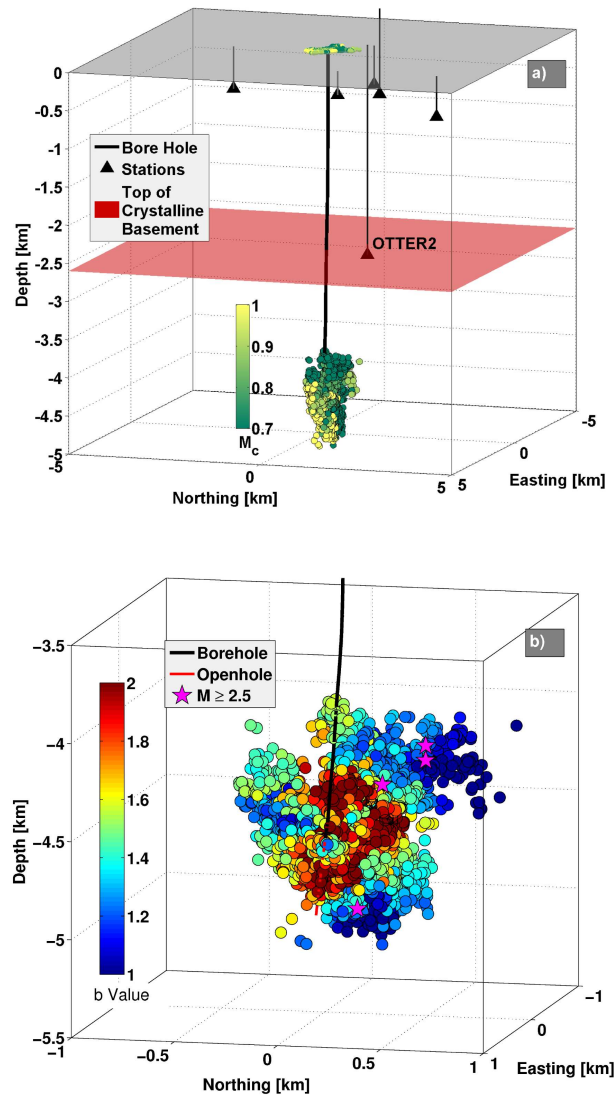


Figure 3.1: Overview: a) Overview of the experiment showing the depth (a.s.l.) of the events (circles) and the location of the seismic stations (triangles). The red plane marks the top of the crystalline basement, within which all events occurred. The colorscale indicates the recording completeness ranging from M_c 0.7 to 1. b) Close-up of the events with the overall b -value distribution. While values range from 0.8 to 3, the colorbar is limited from 1 to 2 for a clearer visibility.

in essentially all seismic hazard studies as it allows extrapolation from the observed smaller events to the infrequent larger ones. Studies of micro-earthquakes on faults (Schorlemmer & Wiemer, 2005; Wiemer & Wyss, 1997) have shown that the b -value, when mapped with high quality data at high resolution, varies in the Earth's crust over distances of a few kilometers or less. These studies, combined with the analysis of regional and global focal mechanism data (Gulia & Wiemer, 2010; Schorlemmer et al., 2005) as well as laboratory work (Amitrano, 2003; Scholz, 1968) indicate that the b -value is inversely proportional to the differential stress σ_D and thus may qualitatively be used as a stress meter at depth in the Earth's crust, where generally no direct measurements are possible. In subduction zones (van Stiphout et al., 2009) and volcanic systems (Wiemer & Wyss, 2002), it has been argued that high b -values are also related to the presence of fluids. In this study we apply for the first time high-resolution b -value mapping to induced seismicity in order to obtain information on the stress regime and possibly the pore-pressure evolution.

Because the evolution of the induced seismicity is a highly dynamic process, we need to investigate the dataset with respect to both, time and space, and to identify the most prominent gradients in the earthquake-size distribution. We first describe the observations and then introduce a geomechanical model to explain the spatio-temporal b -value variability comparing the remarkable match for observed and simulated seismicity (Figures 3.2, 3.3 and 3.4).

The evolution of the observed seismicity as a function of time and distance (Figure 3.2a) illustrates the migration of fluids away from the injection point. The b -value substantially decreases from the co-injection period ($b_{co} = 1.57 \pm 0.06$) to the post-injection period ($b_{co} = 1.14 \pm 0.06$) (Bachmann et al., 2011) (inset to Figure 3.2a), increasing the seismic hazard for the post-injection phase.

We introduce a new focus-centered mapping technique to determine the three-dimensional distribution of the b -values. The local completeness M_c is determined using the closest 150 events in space and is calculated with the maximum curvature method (Woessner & Wiemer,

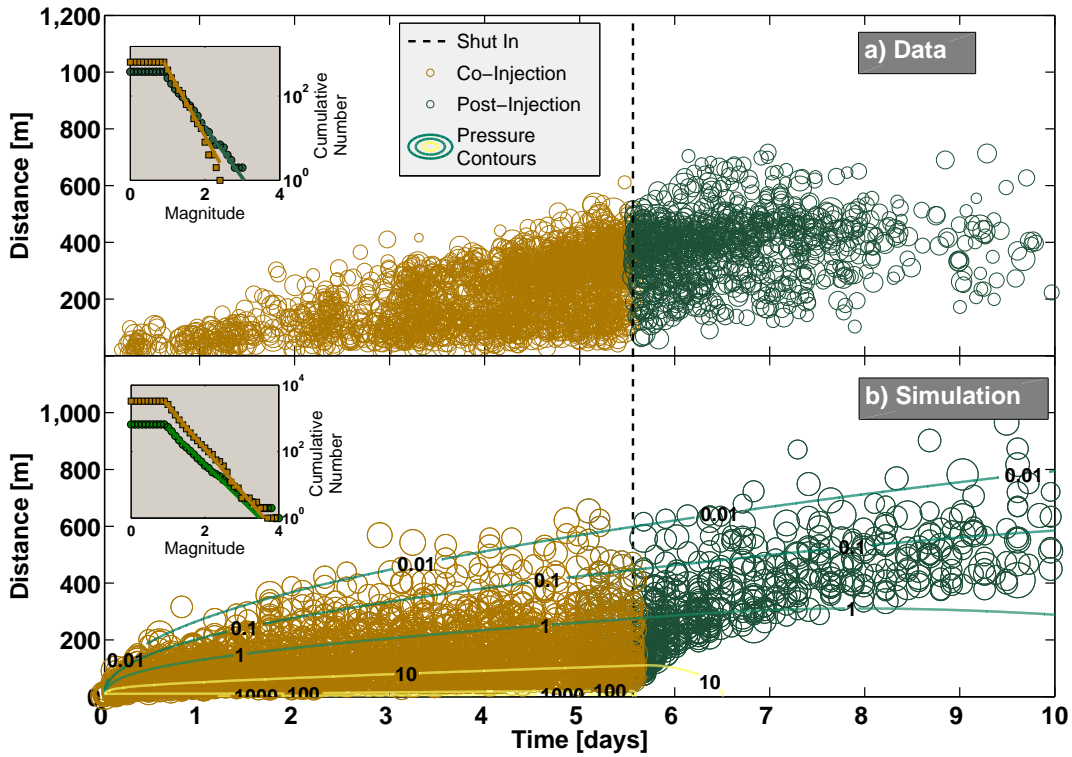


Figure 3.2: Time Evolution: a) Radial distance vs from the injection point. The inset marks the frequency-magnitude distribution of the co- and post-injection period separately. The values are $b_{co} = 1.57 \pm 0.06$ (brown) and $b_{post} = 1.14 \pm 0.06$ (green). b) Equivalent figure for the simulated events, we find $b_{mco} = 1.30 \pm 0.02$ (brown) and $b_{mpost} = 1.08 \pm 0.06$. The contours represent the pressure based on a linear diffusion model and linearly increasing wellhead pressure (Dinske & Shapiro, 2010).

2005). M_c defines the catalogue threshold for determination of the b -value, and ranges from M_c 0.7 – closest to the deepest borehole sensor (Haering et al., 2008) (OTTER2 at 2.2 km distance), to M_c 1 furthest away from the sensor (Figure 3.1 a). To determine the b -value with the maximum likelihood method (Bender, 1983; Utsu, 1999), we require at least 25 events with $M \geq M_c$ in each sample. The resulting b -values range from 0.8 to 3.0 (Figure 3.1b) with a mean standard error of $\sigma(b) = 0.2$. We observe a very systematic behavior: highest b -values are observed close to the casing shoe, forming a toroidal (doughnut-shaped) area, and lowest values are located at the outermost edges of the seismicity cloud. The temporal component of this variability is shown by analysing the co- and post-injection period separately (Figure 3.3a and b); high b -values are observed near the injection point and occur during the injection, while areas with lower b -values are found further away from the borehole and develop after shut-in. Large magnitude events (LME; defined in our context as events felt at the surface, i.e. events with $M_w \geq 2.5$) are located in regions with below average b -values ($b \leq 1.3$). We evaluate this by calculating the *causal* b -value for each event; we determine b -values based on the closest 150 events in space, *preceding* the event. By comparing the distribution against a random correlation of the b -value and the magnitude, we find that it is significant at the 99.95% level to observe five LME in regions with below average b -value.

Figure 3.3c highlights the frequency–magnitude distributions (FMD) of two nodes with significantly different b -values: $b_{red} = 2.96 \pm 0.44$ and $b_{blue} = 0.83 \pm 0.10$. While the red events, close to the injection point, are spatially very concentrated, the blue events at the rim of the seismic cloud are sampled over a larger volume. The potential for larger events such as an M_w 3.5, estimated solely by extrapolating the local FMD, is up to 10,000 times higher in the blue volume. Further systematic behaviour of the seismicity is documented by analysis in one dimension, the distance to the casing shoe, separately for the co- and post-injection period (Figure 3.4a). While a relation between distance and b -value is not obvious for the shortest (< 200 m) distances during the injection, we find a systematic decay of b -values in both periods beyond a distance

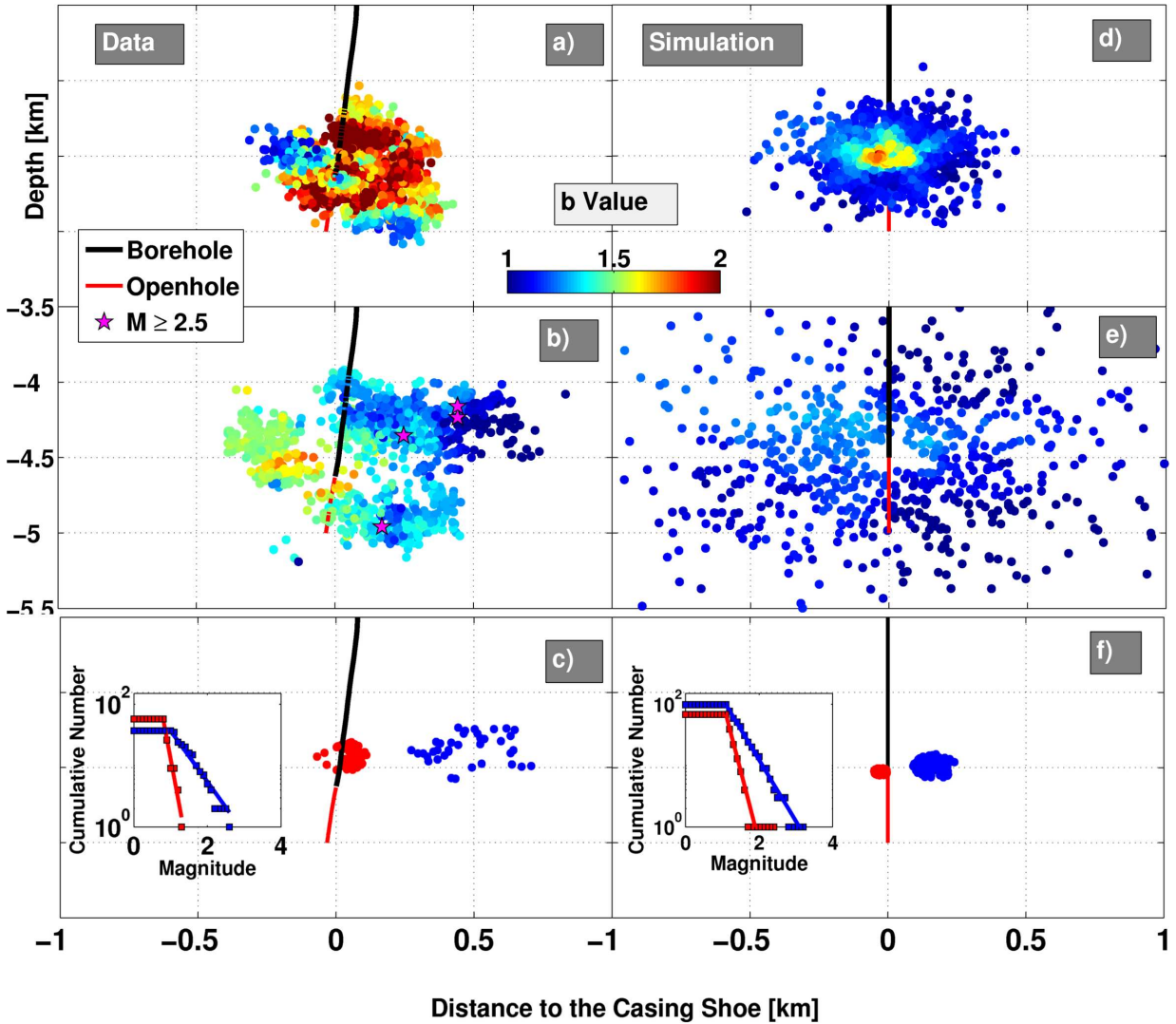


Figure 3.3: b -value Distribution: a) and b), cross section along the N-S axis, with b -value distribution based on co-injection and post-injection events, c) Frequency–magnitude distribution for two sampled areas with a high b -value of 2.93 ± 0.40 (red) and a low b -value of 0.83 ± 0.1 (blue). d) to f) Equivalent plots to a) to c) with the simulated events. The sample volumes in f) show b -values of 2.31 ± 0.30 (red) and 1.00 ± 0.10 (blue). The b -values range from 1 to 2 in all subplots.

of 200 meters that also holds when considering the uncertainty in the data.

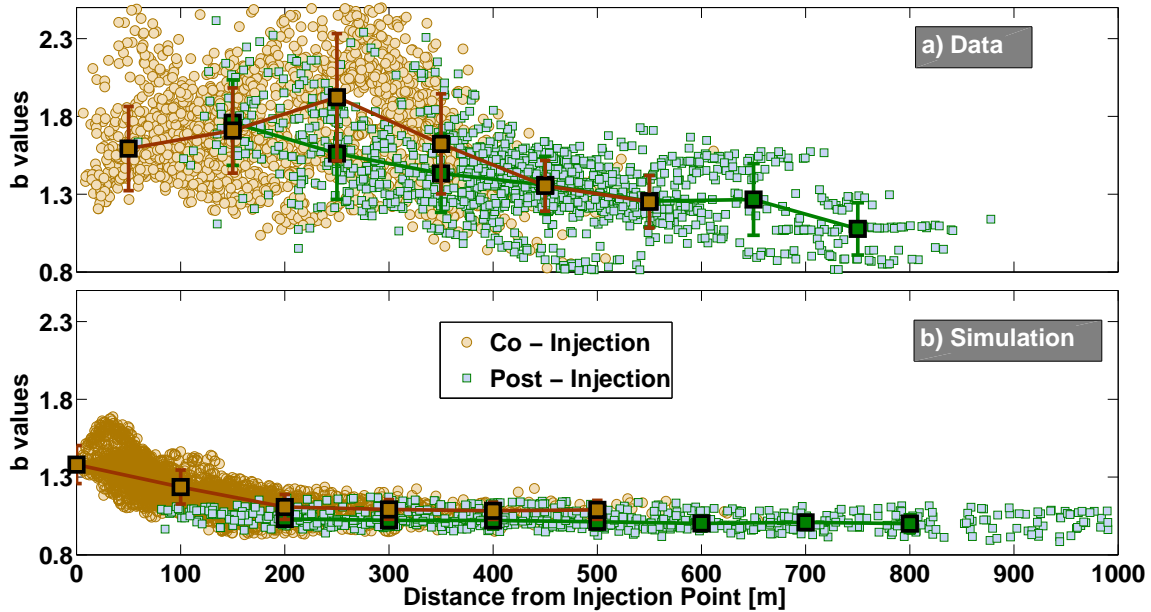


Figure 3.4: Time and Distance: b -values against radial distance from the injection point for a) observed events and b) simulated events. The b -value decays with distance from the injection point starting around 200 m for the data and the simulated events. Events are separated in co- and post-injection periods (brown and green, respectively).

Based on all these observations, the first conclusion we draw is that b -values are spatially highly variable in the induced seismicity sequence of the EGS in Basel, decreasing systematically with time and distance from the casing shoe. The current state of knowledge on b -values of induced sequences is that they are generally higher than normal tectonic events (Wyss, 1972). Our analysis unravels a much more complex yet systematic pattern; values range from typical tectonic b -values at the edges of the seismicity cloud to extremely high values near the injection point. Our detailed spatial mapping indicates that the spatial distribution of the b -value helps to forecast the location of felt events more accurately than possible with a bulk analysis.

To develop a geomechanical understanding of the observed systematic behaviour of the b -

values with space and time, we simulate the induced seismicity cloud in space and time under the hypothesis that high b -values near the injection point are a response to the pore-pressure perturbation.

We randomly distribute potential failure points (we call them seed faults), representing pre-stressed faults, in a two-dimensional space centered around the injection point. Each seed fault is assigned a minimum and maximum principal stress σ_3 and σ_1 , based on a background stress regime according to Haering et al. (2008) and a Gaussian perturbation of 10 %. Using a constant cohesion (7Mpa) and coefficient of friction (0.85), we can analytically calculate the Mohr-Coulomb diagrams and thus a failure criterion for each seed fault. The density of seed faults is a free parameter of the model and can be adjusted to match the observed amount of seismicity. We introduce a time-dependent point pressure source at the injection point. The pressure-time function is linearly increasing over 6 days, a simplified version of the actual injection pressure time series at Basel (Dinske & Shapiro, 2010). We propagate the pore-pressure through the model space based on linear diffusion in a hydraulically isotropic medium with an effective diffusivity of $0.05 \text{ m}^2/\text{s}$. Dinske & Shapiro (2010) introduced an analytical solution to the diffusion equation (Wang, 2000) for the case of a linearly increasing source time function. We use their analytical solution assuming an effective source radius of 70 m, in order to reach realistic values of the pore-pressure perturbation. The naturally occurring pore-pressure variation in the reservoir due to tides is assumed to be on the order of 2000 Pa [Evans pers. comm.], therefore we assume that this is the minimum pressure that is required to trigger an event.

Figure 3.5a depicts the model schematically. The seed faults are represented by the points closest to failure and are color-coded according to their respective differential stress σ_D . The pore-pressure evolution with time reduces the normal stresses shifting the Mohr circles towards the failure. An event is induced once the Mohr circle touches the failure envelope. To assign a magnitude to an event, we exploit the observation from laboratory and natural earthquake analysis that b -values are inversely related to σ_D (Amitrano, 2003; Schorlemmer et al., 2005).

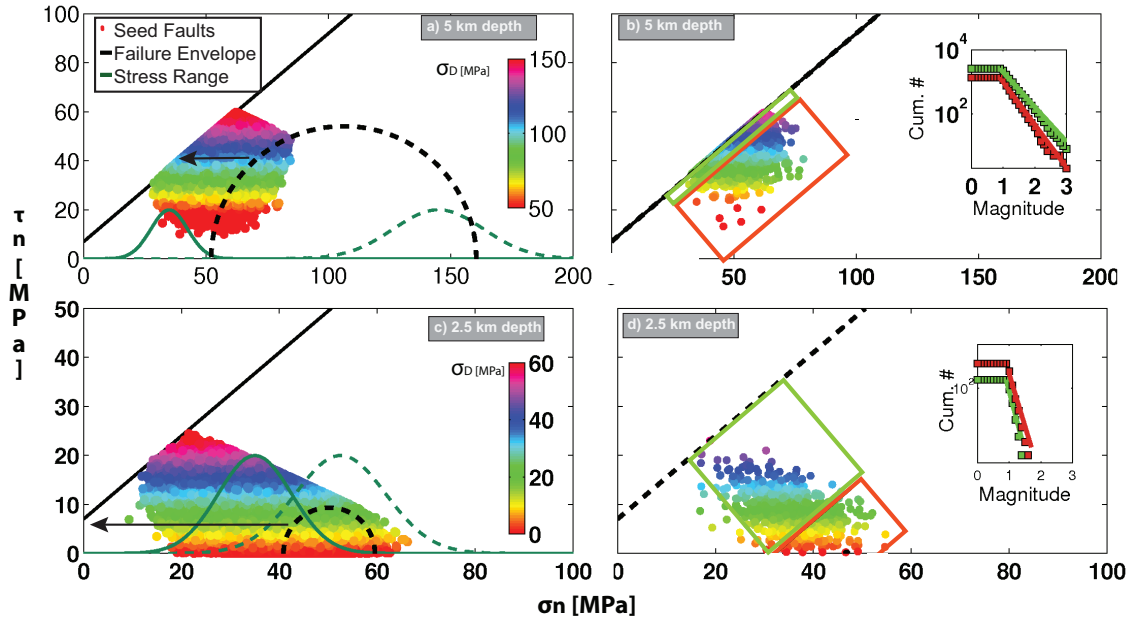


Figure 3.5: Model: a) Mohr-Coulomb plot for the 2D model. Points denote the points close to failure for all 300,000 seed faults. Increasing the pore pressure (ΔP) shifts the potential seed to the left; an event is triggered if the Mohr-Coulomb circle (dashed black circle) touches the failure envelope. The arrow indicates the minimum pore pressure change needed to trigger a seed fault. The b -value and the differential stress σ_D are inversely correlated, leading to an event-size for each seed fault drawn from a power-law with the respective b -value. b) Result of one simulation of the model, a total of 3,921 seed faults were triggered. The b -values for events triggered with high ΔP (green rectangle) and low ΔP (red rectangle) are significantly different, $b_{highP} = 1.33 \pm 0.03$ (green) and $b_{lowP} = 1.08 \pm 0.02$ (red) (indicated by the FMD inset). c) and d) equivalent plots for a narrower stress range at a shallower depth where only 532 events with a high overall b -value of 2.46 ± 0.1 are triggered.

As scaling law, we use a simple linear scaling between the observed ranges of b -values (0.8 to 3.5) and σ_D values of our model (20 to 150 MPa). The magnitudes are then randomly drawn from a power-law distribution with the assigned b -value for each failure occurrence.

Using a linear diffusion model with constant hydraulic diffusivity is a strong simplification for two reasons: (i) the opening of fractures potentially modifies the diffusivity, creating non-linearity (Hummel & Mueller, 2009) and (ii) actual pore-pressure propagation can be highly anisotropic, occurring preferentially along zones of weakness (Evans et al., 2005). However, the model

serves as a first-order approximation and can, at least within 300 m of the casing shoe, explain some features of the observed seismicity well (Goertz-Allmann et al., 2011). We find that the simulated evolution of the seismicity with time and distance (Figure 3.2b) resembles the distribution of the observed events (Figure 3.2a).

Analysing the b -value against the distance to the injection point (Figure 3.4b) of one typical realization of the model indicates that we find the same characteristics in simulated and observed seismicity. The b -values decay with distance from the injection point and are generally higher during the injection (inset to Figure 3.2b). The spatial distribution of the simulated events (Figure 3.3d and e) are likewise similar to the observations; values are high close to the injection point and lower further away. However, the area of high b -values ($b > 1.5$) is more concentrated around the injection point for the simulated events.

To understand the geomechanical reasons for the good match between model and observation, we show the state-of-stress of all seed faults that were triggered in one simulation of the model (Figure 3.5). Out of the 300,000 seed faults, 3,921 ruptured. We divide these into events with pore-pressure changes ΔP above (red square) and below (green square) the mean value of 8.3 MPa and determine the corresponding FMDs of the two subsets (Figure 3.5b). The corresponding b -values are $b_{highP} = 1.33 \pm 0.03$ and $b_{lowP} = 1.08 \pm 0.02$. This can be understood when viewing the available seeds: The subset of faults failing at high pore-pressures contains fewer large differential stresses compared to the one at lower pore-pressures and thus less LME are induced.

In a second application, we simulate the fluid injection at a shallower depth, where the bounds of σ_1 and σ_3 are narrower (compare Fig. 4 of Haering et al. (2008)). The available seed faults (Figure 3.5c) show a much different distribution. The narrower range of the differential stress lead to a different distribution of the b -values. If we divide the seed faults again by those triggered with below and above average pore-pressures, we find $b_{highP} = 2.7 \pm 0.1$ and $b_{lowP} = 2.38 \pm 0.09$. These values are less well constrained than the above ones, as only 524 seed

faults were triggered. These much higher b -values indicate that the potential of triggering large magnitude events is smaller within a narrower stress range and imply that LMEs are less likely at shallower depths.

Our results suggest the following conceptual model for the scaling of the induced seismicity. Near the borehole (0 – 200 m), the pore-pressure rapidly rises once the stimulation starts, and numerous events are induced. These failures sample a wide range of differential stresses, including very small σ_D that were originally far away from the failure criterion but still ruptured due to the high pressure perturbation. It is these small σ_D values that cause a systematic bias towards higher b -values, such that events close to the injection point exhibit a higher b -value. As the pore-pressure front progresses, seed faults experience only a moderate increase in pore-pressure, with correspondingly larger σ_{DC} . The differential stresses of these faults follow more closely a typical tectonic earthquake–size distribution. Once the pumping is stopped, pore-pressures near the well (< 200 m) decrease rapidly, and this area is then essentially devoid of seismicity (Kaiser, 1950). Further out, pore-pressures continue to increase gradually, although absolute values remain low. We suggest that static and dynamic stress changes caused by the numerous earthquakes themselves will contribute to inducing (or in some cases inhibiting) events in these regions. These stress changes also contribute in the vicinity of the injection, but there they are negligible when compared to the pore-pressure. The observed exponential decay of seismicity (Bachmann et al., 2011) with typical aftershock parameters is then a combination of the continued gradual expansion of the pore-pressure front and the gradual decay of aftershock activity caused by static and dynamic stress changes.

Based on this simple geomechanical simulation, we can also address the question of how large future events will be and how likely they will be. Therefore, we evaluate the synthetic seismicity cloud in time and space for a and b -values within specific time- and distance bins. For each time- or distance bin, we can estimate the probability p of an event exceeding a certain magnitude M

as (Wiemer, 2000)

$$p = 1 - e^{-1/x}, \text{ where } x = 1/(a - bM) . \quad (3.1)$$

The probability for an event exceeding M 4 is shown in Figure 3.6. We choose time bins of 10^5 s, moving at 10^4 s intervals, and distance bins of 100 m, moving across distance in 10 m increments. We compare the probability based on our synthetic event cloud with varying b -values (white) with the probability based on an event cloud synthesized from a constant b -value (1.2) (gray). Error bars depict the standard deviation obtained from 100 simulations. For these estimates to be realistic, we need to expand our original two-dimensional model to three dimensions, in order to properly account for the volumetric expansion of the event cloud. The probability of an LME is governed by two factors i) the overall number of events per bin (i.e., the a value) and ii) the b -value in this bin. We find that the probability for LME increases with time during the injection and then decays after the shut-in. A varying b -value causes a substantial increase of the mean probability for the time period right after shut-in (Figure 3.6a), and shifts the maximum of the probability to further distances from the injection point (Figure 3.6b). These calculations are consistent with observations of LME during hydraulic stimulations in geothermal systems not only in Basel (Deichmann & Giardini, 2009), but also elsewhere (Baisch et al., 2010). Our observations and the stochastic model approach presented can form the basis for an improved probabilistic real time forecasting system of induced seismicity in future EGS experiments.

The observed, highly systematic distance and time evolution of the b -values in Basel calls in our opinion for a fundamental mechanism as an explanation. The link between differential stress and b -value is fundamental mechanism, established across a large range of scales, from the analysis of individual rock samples in the laboratory to global seismicity. Adding this as the only independent ingredient to our minimalistic model of induced earthquakes is sufficient to explain the observed b -values evolution in space and time. Furthermore, the ability to explain the size

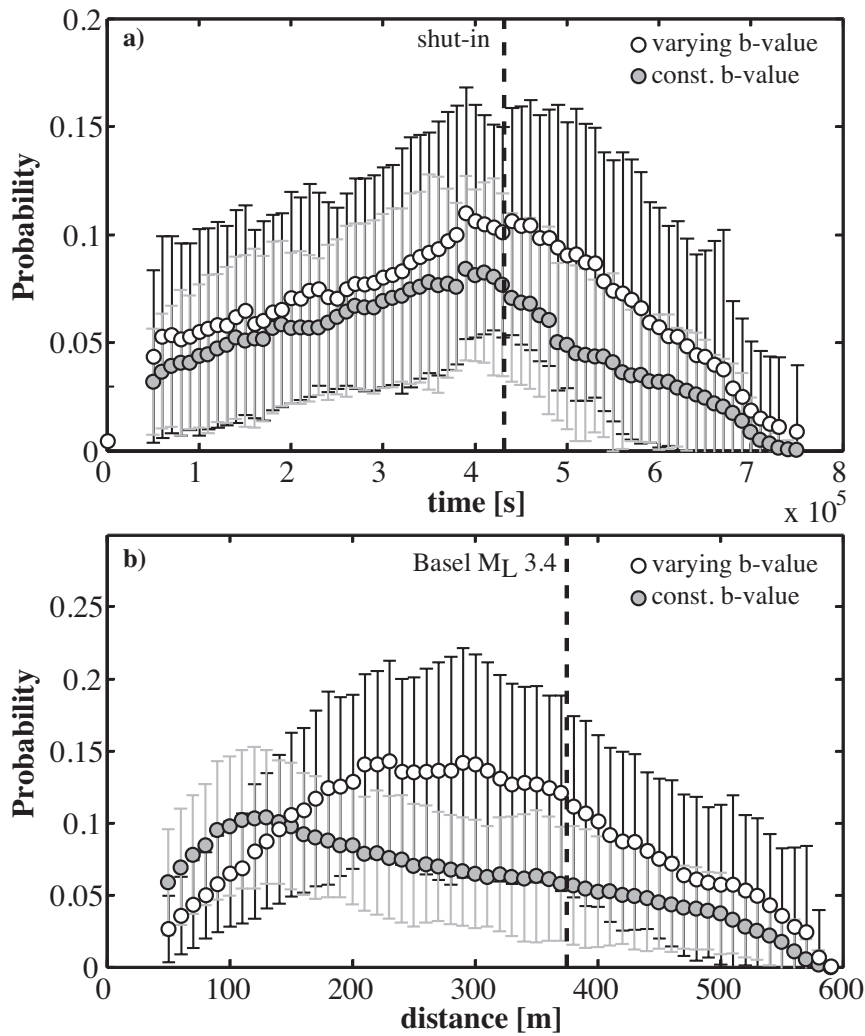


Figure 3.6: Probability for Large Magnitude Events: Occurrence probability of M 4 event, varying with a) time and b) radial distance from the injection point for a varying b -value (white) and a constant b -value (gray). The errorbar denotes the standard deviation based on 100 simulations of the geomechanical model. The dashed line in a) marks the shut-in time and in b) the location of the largest observed Basel event.

distribution of induced events is strong additional evidence that differential stress is one of the governing parameters that influences b -values for a wide range of tectonic settings.

We propose that our conceptual model, developed for the well-recorded induced seismicity in the natural laboratory of the Basel EGS, is universally able to explain a wide range of observations of the earthquake-size distribution. We speculate that the same mechanism of pore-pressure changes is responsible for other high b -values anomalies in the Earth's crust: in aftershock zones near the areas of highest slip (Wiemer & Katsumata, 1999); in volcanic regions near magma chambers (Wiemer & McNutt, 1997) and in subduction zones (van Stiphout et al., 2009). It is worthwhile noting that in the immediate vicinity of the rupture plane of larger earthquakes, static and dynamic stress changes are expected to be large enough to trigger events with a wider than usual range of differential stresses, thus contributing to higher b -values near faults.

Acknowledgements We would like to thank Geothermal Explorers Ltd., who provided seismicity data without which this work would not have been possible. This study is part of the project GEOTHERM, funded by the Competence Center of Environment and Sustainability (CCES) of ETH (<http://www.cces.ethz.ch/projects/nature/geotherm/>).

References

- Amitrano, D., 2003. Brittle-ductile transition and associated seismicity: Experimental and numerical studies and relationship with the b value, *J. Geophys. Res. - Solid Earth*, **108**(B1).
- Bachmann, C., Wiemer, S., Woessner, J., & Hainzl, S., 2011. Statistical analysis of the induced Basel 2006 earthquake sequence: Introducing a probability-based monitoring approach for enhanced geothermal systems, *Geophys. J. Int.*, **186**, 793 – 807.
- Baisch, S., Carbon, D., Dannwolf, U., Delacou, B., Devaux, M., Dunand, F., Jung, R., Koller, M., Martin, C., Sartori, M., Secanell, R., & Voeroes, R., 2009. Deep heat mining Basel - seismic risk analysis, Tech. rep., Serianex.
- Baisch, S., Voeroes, R., Rothert, E., Stang, H., Jung, R., & Schellschmidt, R., 2010. A numerical model for fluid injection induced seismicity at Soultz-sous-Forets, *International Journal of Rock Mechanics and Mining Sciences*, **47**(3), 405–413.
- Bender, B., 1983. Maximum-likelihood estimation of b-values for magnitude grouped data, *Bull. Seismol. Soc. Am.*, **73**(3), 831–851.
- Deichmann, N. & Giardini, D., 2009. Earthquakes Induced by the Stimulation of an Enhanced Geothermal System below Basel (Switzerland), *Seismol. Res. Letts.*, **80**(5), 784–798.
- Dinske, C. & Shapiro, S., 2010. Interpretation of microseismicity induced by time-dependent injection pressure, *SEG Expanded Abstracts*, pp. 2125–2129.
- Evans, K., Moriya, H., Niitsuma, H., Jones, R., Phillips, W., Genter, A., Sausse, J., Jung, R., & Baria, R., 2005. Microseismicity and permeability enhancement of hydrogeologic structures during massive fluid injections into granite at 3 km depth at the Soultz HDR site, *Geophys. J. Int.*, **160**(1), 388–412.
- Giardini, D., 2009. Geothermal quake risks must be faced, *Nature*, **461**, 848–849.
- Goertz-Allmann, B. P., Goertz, A., & Wiemer, S., 2011. Stress drop variations of induced earthquakes at the Basel geothermal site, *Geophys. Res. Lett.*, **38**.

REFERENCES

- Gulia, L. & Wiemer, S., 2010. The influence of tectonic regimes on the earthquake size distribution: A case study for Italy, *Geophys. Res. Let.*, **37**.
- Gutenberg, B. & Richter, C. F., 1942. Earthquake magnitude intensity, energy, and acceleration, *Bull. Seismol. Soc. Am.*, **32**, 163–191.
- Haering, M. O., Schanz, U., Ladner, F., & Dyer, B. C., 2008. Characterisation of the Basel 1 enhanced geothermal system, *Geothermics*, **37**(5), 469–495.
- Hummel, N. & Mueller, T. M., 2009. Microseismic signatures of non-linear pore-fluid pressure diffusion, *Geophys. Res. Let.*, **179**(3), 1558–1565.
- Kaiser, J., 1950. *Untersuchungen über das Auftreten von Geräuschen beim Zugversuch*, Ph.D. thesis, Fak. f. Maschinenwesen, TH Munich, Germany.
- Scholz, C., 1968. Frequency–magnitude relation of microfracturing in rock and its relation to earthquakes, *Bull. Seismol. Soc. Am.*, **58**(1), 399–&.
- Schorlemmer, D. & Wiemer, S., 2005. Microseismicity data forecast rupture area, *Nature*, **434**(7037), 1086.
- Schorlemmer, D., Wiemer, S., & Wyss, M., 2005. Variations in earthquake-size distribution across different stress regimes, *Nature*, **437**(7058), 539–542.
- Utsu, T., 1999. Representation and analysis of the earthquake size distribution: A historical review and some new approaches, *Pure appl. geophys.*, **155**(2-4), 509–535.
- van Stiphout, T., Kissling, E., Wiemer, S., & Ruppert, N., 2009. Magmatic processes in the Alaska subduction zone by combined 3-D b value imaging and targeted seismic tomography, *J. Geophys. Res. - Solid Earth*, **114**(B11), B11302 (16 pp.).
- Wang, H., 2000. *Theory of linear Poroelasticity with Applications to Geomechanics and Hydrogeology*, Princeton Univ. Press.
- Wiemer, S., 2000. Introducing probabilistic aftershock hazard mapping, *Geophys. Res. Let.*, **27**(20), 3405–3408.
- Wiemer, S. & Katsumata, K., 1999. Spatial variability of seismicity parameters in aftershock zones, *J. Geophys. Res. - Solid Earth*, **104**(B6), 13135–13151.
- Wiemer, S. & McNutt, S., 1997. Variations in the frequency-magnitude distribution with depth in two volcanic areas: Mount St Helens, Washington, and Mt Spurr, Alaska, *Geophys. Res. Let.*, **24**(2), 189–192.

REFERENCES

Wiemer, S. & Wyss, M., 1997. Mapping the frequency–magnitude distribution in asperities: An improved technique to calculate recurrence times?, *J. Geophys. Res. - Solid Earth*, **102**(B7), 15115–15128.

Wiemer, S. & Wyss, M., 2002. Mapping spatial variability of the frequency–magnitude distribution of earthquakes, in *Advances In Geophysics*, vol. 45 of **Advances In Geophysics**, pp. 259–302.

Woessner, J. & Wiemer, S., 2005. Assessing the quality of earthquake catalogues: Estimating the magnitude of completeness and its uncertainty, *Bull. Seismol. Soc. Am.*, **95**(2), 684–698.

Wyss, M., 1972. Towards a physical understanding of the earthquake frequency distribution, *Geophysical Journal of the Royal Astronomical Society*, **31**(4), 341–59.

Chapter 4

Analysis of the Soultz-sous-Forêts seismicity induced by an injection test in 1993

Corinne E. Bachmann

Abstract

To determine the general validity of the results of Chapter 2 and 3, this chapter analyses the seismic data recorded during an injection test in 1993 from the Enhanced Geothermal System (EGS) in Soultz-Sous-Forêts (SSF), France. The observed magnitudes from this data range from $M_w = -2.5$ to 1.4, two events with magnitude 1.4 occurred during the first injection (after 7.75 and 12.5 days). A total of 25 events with $M_w \geq 1$ were recorded. Unlike in Basel, the injections were not interrupted by a large magnitude event. During September and October 1993, a total of three injections took place: two long term injections during 15 and 5.5 days and one short term injection over 2 days which had to be stopped due to system failure.

The analysis of the statistical parameters shows a similar overall behaviour of the Soultz-sous-Forêts data and the Basel data. While the b -value range from Soultz is lower, the relative pattern is similar with highest values of b close to the open hole sections and lower values further out. Values from sequences where no fluid injection is involved are smaller than values from stages associated with injections. This is consistent with the model proposed in Chapter 3 which implies that high pore pressures are the cause for high b values. To determine the decay after the two longterm injections, the data is fit with the modified Omori-Utsu law. While the decay after the second long term injection fits this law, the decay after the first injection is too short and does not follow this law.

The ongoing seismicity of the first injection during the 1993 SSF sequence is modelled with two approaches – the best-fitting real-time ETAS model (E5) from Chapter 2 and a model introduced by Shapiro et al. (2010), adapted to real-time by Mena & Wiemer (2011).

This study emphasises that the findings from chapter 2 and 3 are not limited to the data recorded during the EGS experiment in Basel. The results are more global and the methods can be applied to other induced seismic sequences.

4.1 Introduction

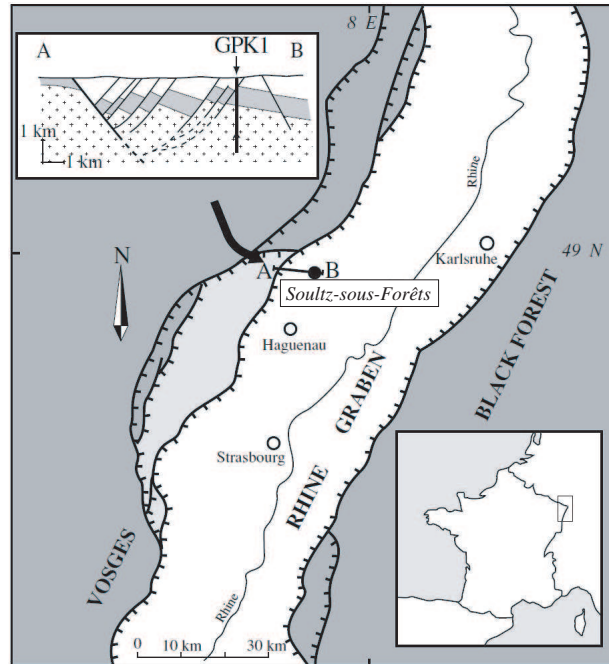


Figure 4.1: Overview of the geological setting of Soutz-Sous-Forêts site. The site lies within the Upper Rhine graben. The cross-section marks the granite (cross-pattern, dark grey in plan view), Mesozoic sediments (light grey) and the Oligocene and Miocene sediments (white). Figure taken from Evans et al. (2005)

The Enhanced Geothermal System in Soutz-sous-Forêts (SSF), France has a history of over 20 years with several injection tests. By adapting the methods to describe induced seismicity from Chapters 2 and 3 to data from this site, I aim to establish that the observations made for the induced seismicity sequence from the EGS in Basel, Switzerland are not only characteristic to this sequence but can be more generalised.

The geothermal study site in SSF lies within the upper Rhine graben, close to the German border (Figure 4.1). Over the last 20 years there have been several injections into five different boreholes (see Figure 1.4b and <http://www.soultz.net/>). The ongoing seismicity induced by different injection test, has been widely studied (e.g. Cuenot et al., 2006; Dorbath et al., 2009;

Evans et al., 2005). Today, three reservoirs have been developed within granite at depths of 3.5 and 5 km.

This study analyses the seismicity induced by an early injection in September and October 1993. These test were the third injections at the SSF site, but the first through openhole (Jones et al., 1995). The well GPK1 (marked in Figure 4.1 and Figure 4.2) had been drilled down to 2000m before and was extended down to 3600m in 1992; the casing shoe is at 2580m depth. During the two months of this injection test, three different parts of the GPK1 well were stimulated. A total of about 18,000 microseismic events were induced, of which 12246 were located (Evans et al., 2005)

4.2 Data

4.2.1 Seismic Network

The seismic network consists of three down hole stations, installed in abandoned oil wells at depths of 1400 to 1600m (Baria et al., 1995; Jones et al., 1995). The location of the seismic stations is marked by numbers in Figure 4.2.

4.2.2 Injections

The seismicity can be divided into six stages, three are associated with fluid injections and three are intermediate or post-injection periods (Figure 4.4).

September Injection

The September injection started on September 2 1993 and lasted for 15 days, during which approximately 25,300 m³ of water was injected into the open hole section from 2850 to 3400m.

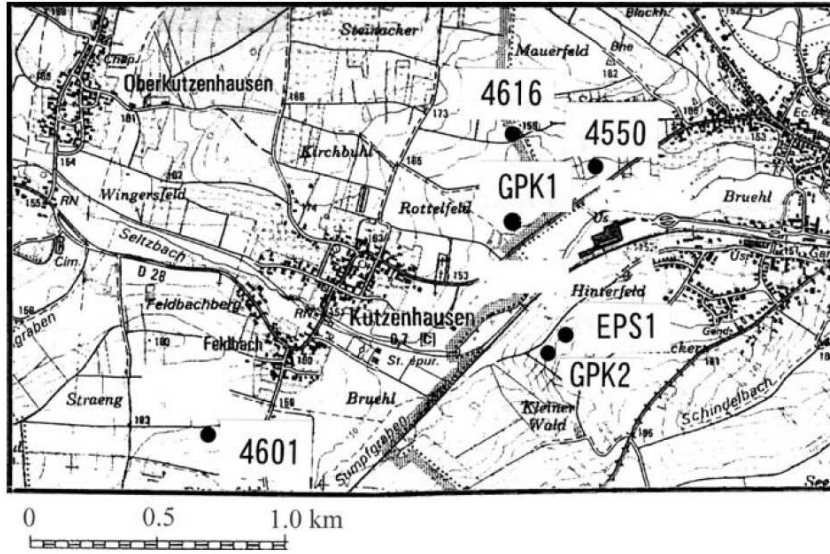


Figure 4.2: Map showing the region of the Sultz-Sous-Forêts Site with the closest settlements. GPK1, EPS1 and GPK2 denote three wells. the numbered wells are abandoned oil wells, hosting the seismic network. Figure taken from Evans et al. (2005)

The openhole part from 3400 to 3600m was filled with sand during this injection. The injection rate was increased stepwise from 0.15 l/s to a maximum of 40 l/s (see Figure 4.3a). During these 15 days, a maximum well-head pressure of 10 MPa was reached (Figure 4.3b) and approximately 9,500 events were induced (Figures 4.3c and 4.4a). The time evolution (Figure 4.5a) of the events in this stage indicates that they evolve away from the borehole. The distance to the casing shoe increases to up to 800m during this 15 days. The injection was followed by a day of shut in and two days of venting. A total of 1,200 m³ of fluid was vented.

Following this injection, there was a test to stimulate a main fracture zone at 3485 m depth. The borehole was sealed with a double packer and water was first injected at 3.5 l/s and then at 6 l/s during which the packer failed and the test was abandoned. Only around 70 events were induced during this test (Figure 4.4c). They are all concentrated around the injection point.

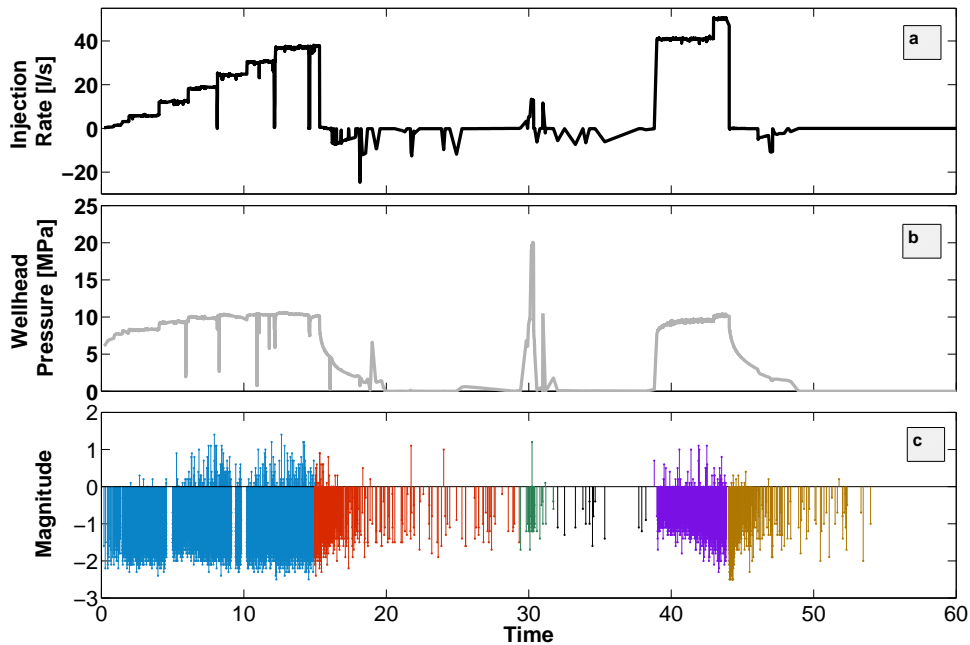


Figure 4.3: Injection rate, wellhead pressure and observed seismicity rate during the 1993 injection test at the SSF site. The colours of the seismicity correspond to the six different stages of the seismicity associated with the six different co-injection and post-injection periods (compare Figure 4.4). Holes in the seismicity rate indicate three different periods (4.75d, 9.2d and 10d) where no data was recorded due to technical difficulties.

October Injection

In October, the previously sanded part of the borehole below 3400 m was washed out and water was injected in the entire open hole section from 2850 m to 3600m. The injection lasted four days, and was increased from 41 l/s to 50 l/s after three days, leading to a total of 12,000 m³ of fluid. The well-head pressure once again reached around 10MPa. The seismicity is first concentrated around the newly open section and then spreads to previously stimulated zones (Figure 4.4e). The time evolution of the events highlights this as well (Figure 4.5b), the events occur first within 300m distance from the newly opened part of the borehole at 3400m depth

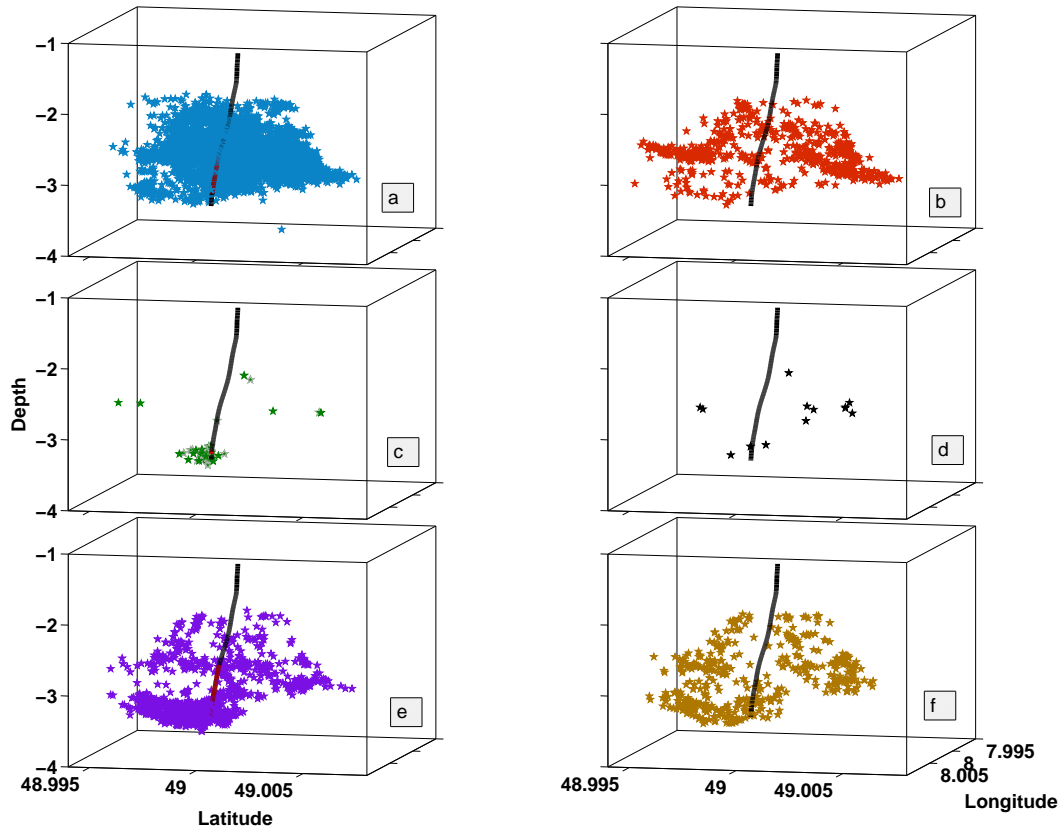


Figure 4.4: Illustration of the seismicity during the six different stages. a) First injection in the open hole section from 2850 to 3400m, during first 15 days, b) decay after the first injection from 15 days up to 29 days, c) injection into a fracture zone at 3485 depth for two days, during which the borehole was sealed with a double-packer above and below 3845 m depth d) decay after the double-packer injection from 32 up to 39 days, e) third large scale injection from 2850m down to the bottom of the borehole at 3600m, f) decay after the last injection. The borehole is marked in black in all panels, the respective open hole sections in red. The colours of the seismicity corresponds to the colours in Figure 4.3.

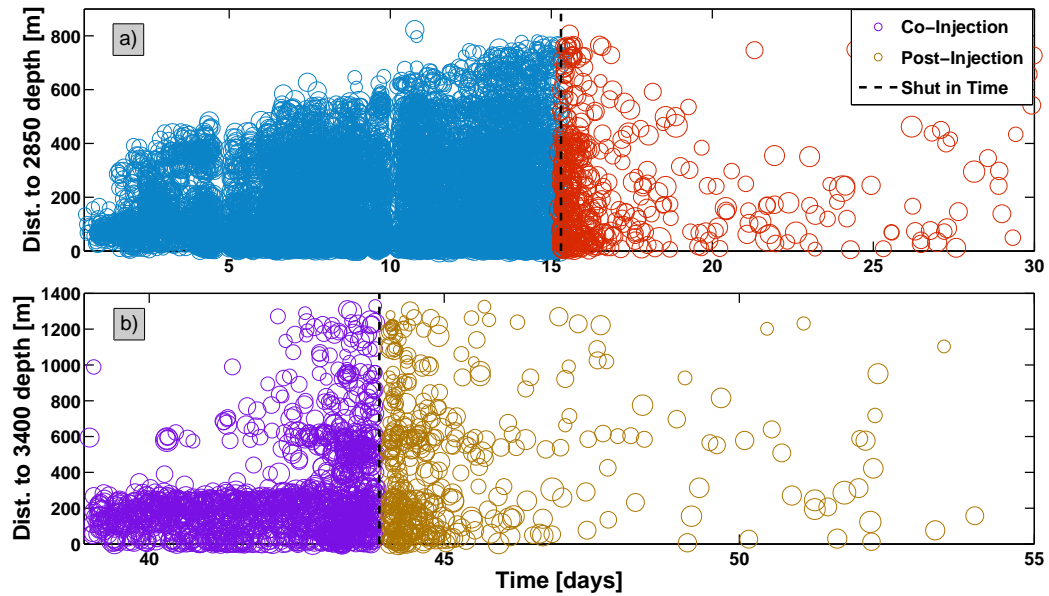


Figure 4.5: Time versus distance for the two main injections and their post-injection events. For a) the distance against the casing shoe at 2850 m depth is measured, for b) the distance from the newly open part of the borehole at 3400m is measured. While there is a typical increase with distance for the first injection, the seismicity is concentrated in the previously unstimulated part for the third injection. The colours correspond to Figures 4.4 and 4.3

and only spread further away after three days.

Intermediate Seismicity

The seismicity occurring in between and after the injections is much sparser (Figure 4.4b, d and e). There are only 660, 22 and 484 events between and after the injections, respectively.

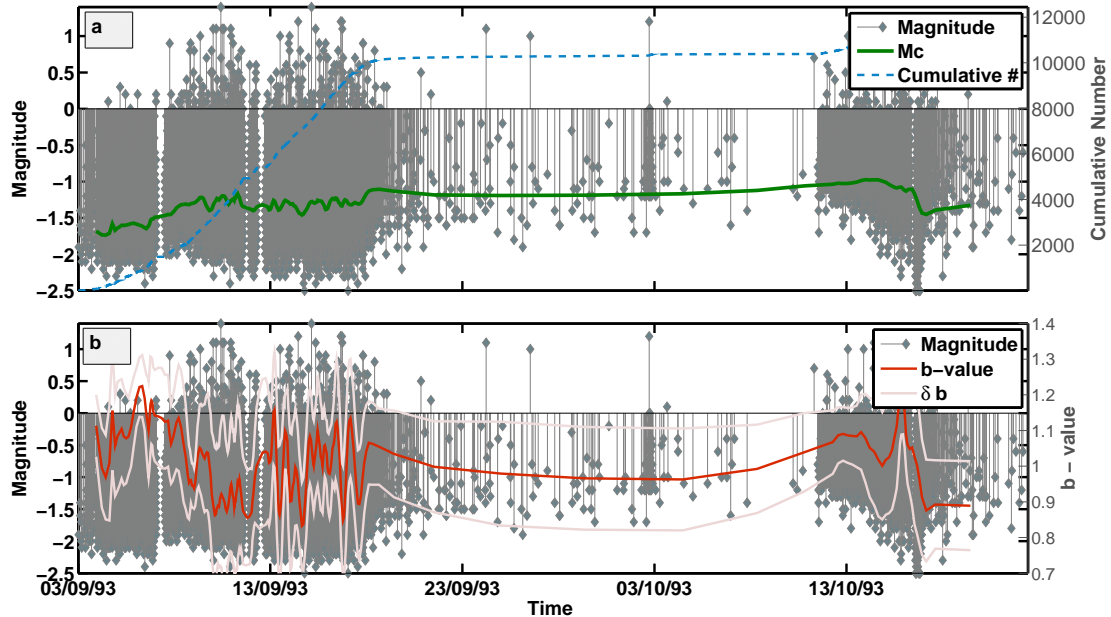


Figure 4.6: Statistical parameters of the seismic sequence with time for a) completeness magnitude and b) b -value with one standard deviation.

4.3 Analysis of the SSF Sequence

4.3.1 Statistical parameters of the SSF sequence

Completeness and overall b -values

As a first step, I analyse the overall statistical parameters of the seismic sequence from SSF. The magnitude of completeness (M_c), determined with the maximum curvature method (Wiemer & Wyss, 2000; Woessner & Wiemer, 2005) in overlapping time bins of 200 events, varies highly with time (green line in Figure 4.6a). The completeness varies from values of $M_c = -1.7 \pm 0.11$ to $M_c = -1.0 \pm 0.12$ over time. A conservative assumption of the overall magnitude of completeness is therefore $M_c = -1$, which will be used in the subsequent analysis of the data.

To estimate the changes in the earthquake size distribution over time, I estimate the variation of the b -value of the Gutenberg-Richter law (Gutenberg & Richter, 1942) over time. This is done equivalent to the completeness estimation in overlapping time bins of 200 events (red line Figure 4.6b). The values of b vary from 0.83 ± 0.12 to 1.2 ± 0.09 . The largest variations are found in during the first injection, where b varies from 1 to 1.2. The changes of b can also be analysed for the six different stages separately. The overall completeness $M_c = -1$ leads to insufficient events to determine a significant b value for the third and the fourth stage. The b values of the remaining four stages are substantially different (Figure 4.7). While the differences in the b -values are not as pronounced as in Chapter 2 and 3, the values for stages related to fluid injections are substantially higher than b -values values associated with intermediate seismicity (Figure 4.7).

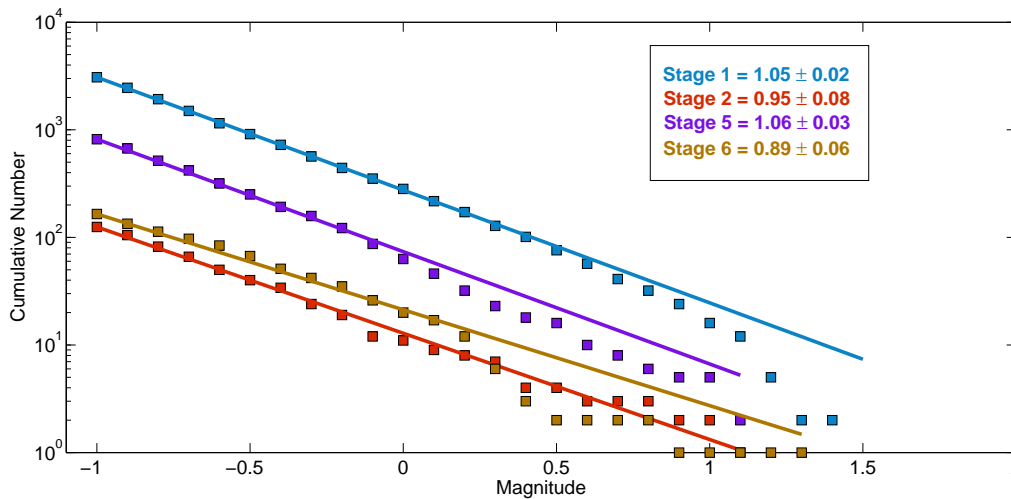


Figure 4.7: Frequency–magnitude distributions for four out of six stages (see Figure 4.4). While the first (blue) and the fifth (purple) stage are associated with fluid injections, the second (red) and the sixth (brown) stage show the decay after the two longterm injections. Values of b associated with fluid injections are substantially higher.

Three dimensional b value distribution

To determine the three dimensional distribution of the b -values, one first has to determine the local completeness. As above, this done with the maximum curvature method (Wiemer & Wyss, 2000; Woessner & Wiemer, 2005). Equivalent to Chapter 3, the 150 nearest events at each earthquake location are sampled to determine the completeness. This estimate varies from $M_c = -2.1$ to -0.7 , with the largest variations over depth. The deepest borehole seismometer is installed at 1600m depth, more than 400m above the shallowest seismicity. This can in part explain this large gradient.

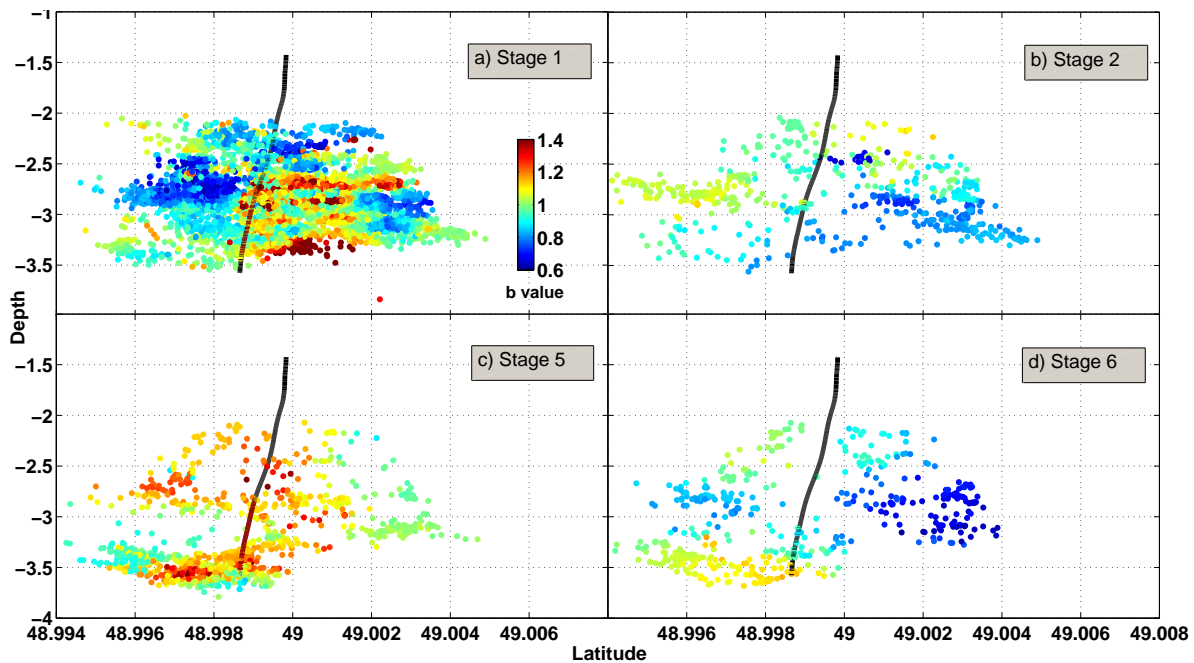


Figure 4.8: Three dimensional b -value distribution for four out of the six stages (see Figure 4.4). Stages 1 and 5 are associated with fluid injections, stages 2 and 6 show the decaying seismicity after the injections. Higher b -value are found during the injections, close to the openhole sections. Lower values are found further out, from the decaying sequences. The three dimensional distribution of stage 1 is shown in more detail in Figure 4.9.

To determine a b -value, at least 25 events above the local completeness are required at each

node. As before, the seismicity is too sparse during the third and the fourth stage. Therefore the b -value distribution is only determined for six stages (Figure 4.8). The values of b , determined with the maximum likelihood method (Aki, 1965; Bender, 1983; Utsu, 1999), vary from 0.6 to 1.4 for all four stages.

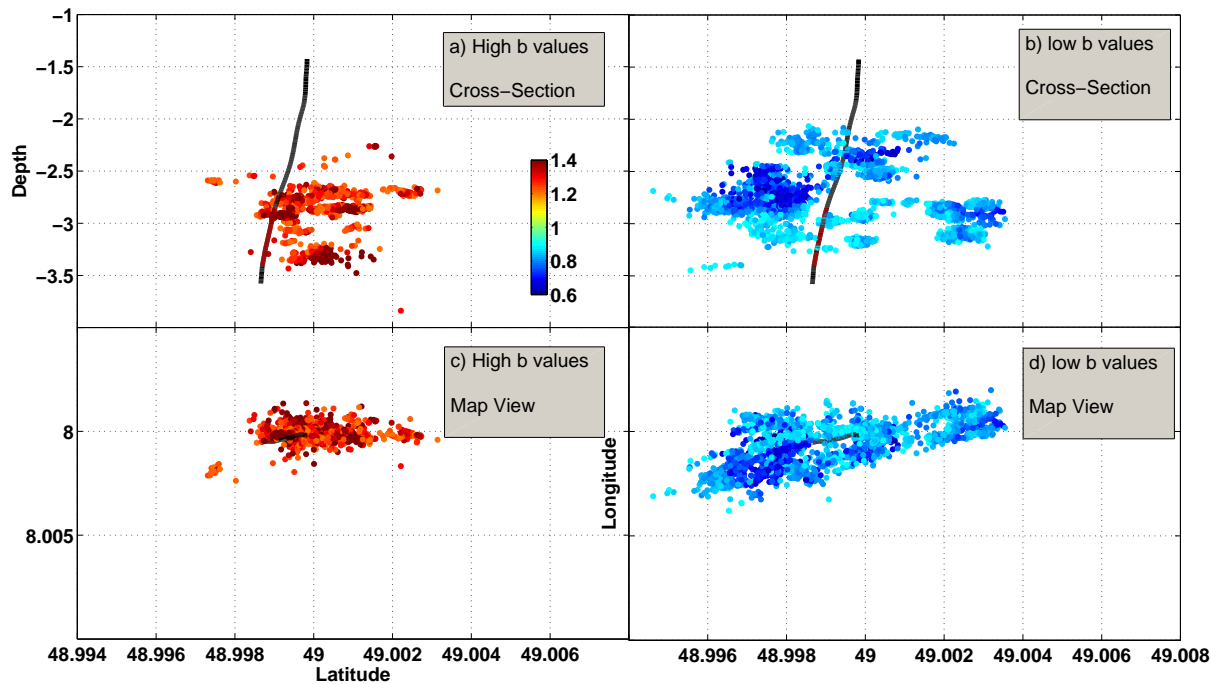


Figure 4.9: Three dimensional b -value distribution of the first stage, divided into areas with $b \geq 1.2$ and $b \leq 0.9$, shown as cross section (a, b) and mapview (c, d). The cross sections highlight that higher b -values are found closer to the injection point and lower values further out. The mapview emphasises the extension of the areas with high, respectively low b -values. Lower b -values are found further out than higher values.

The b -values show a similar pattern as in Chapter 3 (compare Figure 3.3) with higher values close to openhole sections and in stages related to fluid injections, and lower values further out and in stages without active injection. During the first stage, over 9,000 events were recorded, which leads to a highly overlapping three-dimensional view where the patterns are not easily differentiated. Dividing the b -values in $b \geq 1.2$ and $b \leq 0.9$ allows one to analyse the patterns in

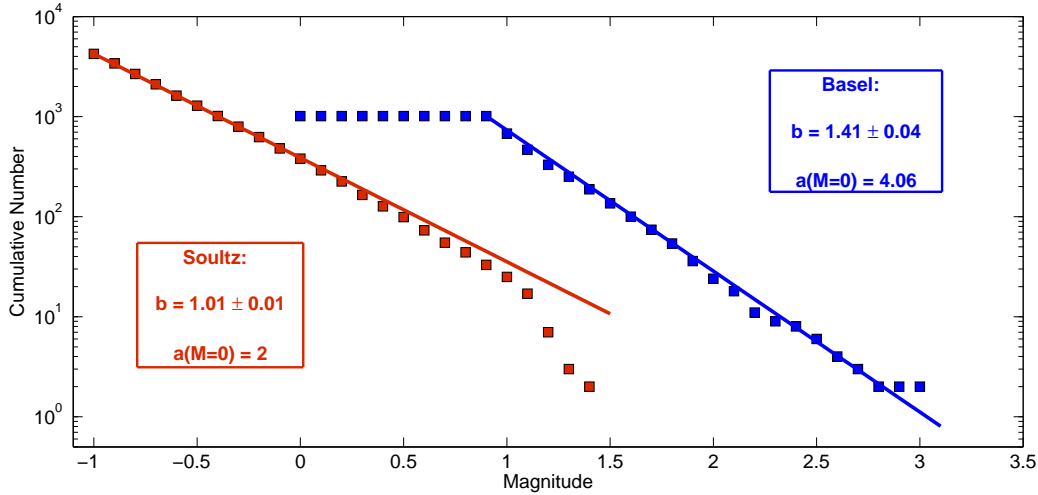


Figure 4.10: Comparison of the frequency–magnitude distribution (FMD) of the SSF and the Basel sequence. As the magnitude definitions are substantially different, a direct comparison between both FMDs is not possible.

more detail (Figure 4.9). This partition highlights the above stated observations: high b -values are concentrated near the open hole section (red in Figure 4.9) and lower values are found further away (blue in Figure 4.9). The mapview emphasises that the extension of the area with lower b -values is larger than the area with smaller values (Figure 4.9c and d).

Chapter 3, introduced the relations between the pore pressure diffusion and the b -value distributions. Large changes in the pore pressure lead to a relative excess of smaller events and thus to high b -values. The highest pore pressures are generally observed close to the open hole section and along the paths of preferred fluid flow. I therefore conclude that mapping the b -value distribution for the SSF site helps to improve the understanding of the created reservoir. Comparing the b -values found in this study with the values from Chapter 3, shows that the range is substantially smaller in this study; $b = 0.5 - 2$, compared to $b = 0.8 - 3$. In addition, the recorded magnitude ranges differ considerably; while the magnitudes from SSF range from $M_w = -2.5$ to 1.4, Basel shows events from $M_w = 0.1$ to 3.1. The frequency–magnitude distributions

(FMD) of these two data sets are highly different (Figure 4.10)

Since the magnitude definitions of the two sequences are substantially different, it is not possible to directly compare both values. This indicates that one has to know that magnitude definitions of two regions are similar before comparing absolute b -values. If they are too different, it is preferable to only examine relative changes.

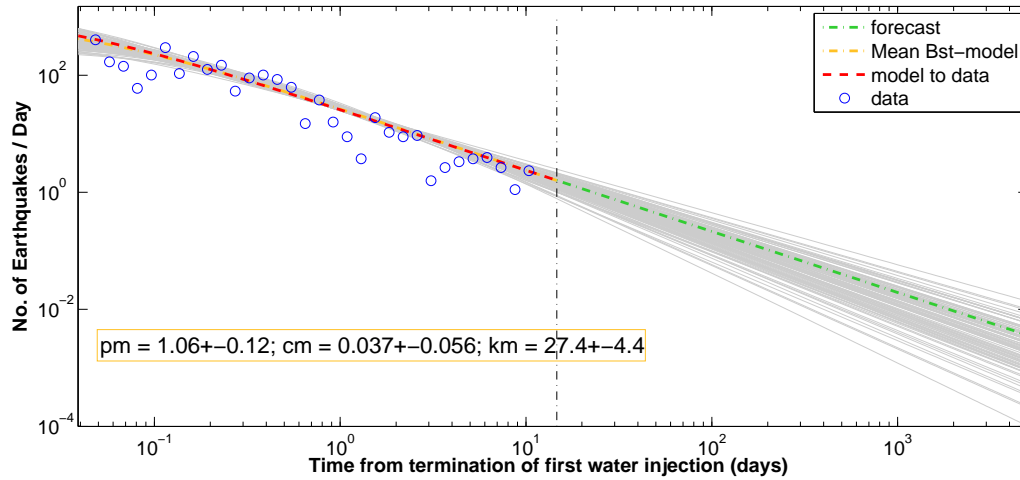
Fitting the decay of two stages

To determine whether the decay of the seismicity in the intermediate stages can be described similar as the decay of the Basel sequence, I fit the modified Omori-Utsu law (Ogata, 1999; Utsu, 1961) to the stages after the two long term injections (Stage 2 and 6). The modified Omori-Utsu law normally describes the rates of aftershock sequences:

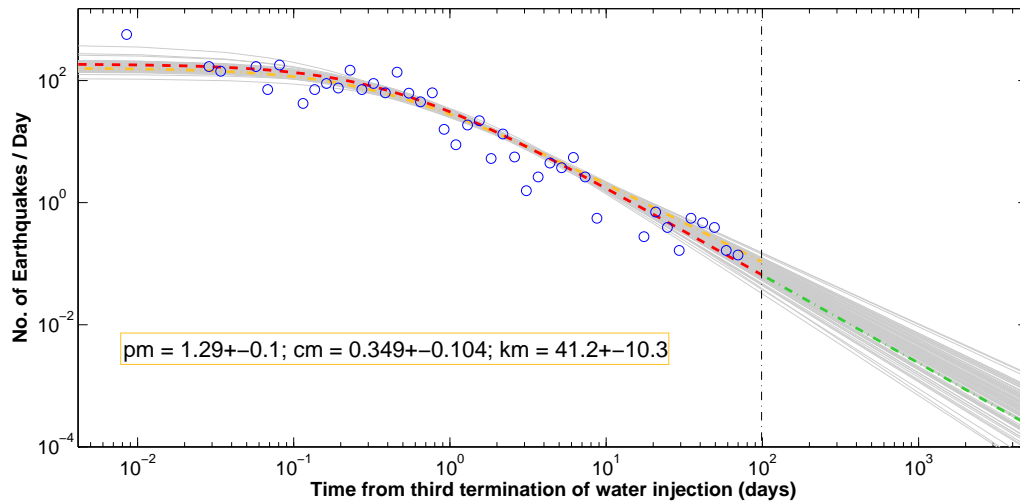
$$\lambda(t, M_c) = \frac{k(M_c)}{(t + c)^p} \quad (4.1)$$

where t is the time elapsed after the main shock, c and p are empirical parameters, characteristic for a specific sequence, and $k(M_c)$ is a function of the number of events with magnitudes above the completeness magnitude M_c .

While the time between the first injection and the double packer injection is relatively short and does not show a decay following equation 4.1, the decay after the last injection follows the modified Omori-Utsu law (Figure 4.11). The decay after the last injection passes the two-sample Kolmogorov-Smirnov (Conover, 1972; Woessner et al., 2004) test. This test, determines whether the cumulative rate of the data and the fitted Omori-Utsu law belong to the same distribution; it is not rejected at the significance level of 0.05.



(a)



(b)

Figure 4.11: Decay after the two major injections; a) from 15.4 to 29.2 day and b) after 43.9 days. The decay between the first injection and the double packer injection (a) can not be fit with the modified Omori-Utsu law, however the decay after no additional injections follow (b) can be well fit with this law.

4.3.2 Forecasting of the seismicity rate

4.3.2.1 ETAS and Shapiro Model

The ongoing seismicity of the SSF sequence is forecast with two models: the best-fitting real-time model from Chapter 2 – i.e. an epidemic type aftershock (ETAS) model with additional

information about the injection rate – and a model introduced by Shapiro et al. (2010). The later model has been adapted to real-time updating by Mena & Wiemer (2011).

According to the ETAS model by Ogata (1988), the rate of aftershocks induced by an event occurring at time t with magnitude M_i is given as:

$$\lambda_i(t) = \frac{K}{(c + t - t_i)^p} 10^{\alpha(M_i - M_{min})} \quad (4.2)$$

for time $t > t_i$. The parameters c and p are empirical parameters and K and α describe the productivity of the sequence. The total occurrence rate is the sum of the rate of all preceding earthquakes and a constant background rate λ_0 :

$$\lambda(t) = \lambda_0 + \sum_{[i:t < t_i]} \lambda_i(t) \quad (4.3)$$

The best-fitting real-time model in Chapter 2 included the applied injection rate F_r in the forcing term. According to Shapiro & Dinske (2009), the fluid-triggered event rate is modelled as proportional to the injection rate. The background rate then becomes:

$$\lambda_0(t) = \mu + c_f \times F_r(t) \quad (4.4)$$

with c_f and μ being free parameters.

Shapiro et al. (2010) introduce a model where the number of events is linked to the the injected fluid volume Q_c :

$$\log N_M(t) = \log Q_c(t) - bM + \Sigma \quad (4.5)$$

where M is the magnitude, b is the b -value of the frequency–magnitude distribution (Gutenberg & Richter, 1942) and Σ is the seismogenic index. The seismogenic index can be derived by

using the seismicity rate and the fluid injection rate from equation 4.5:

$$\Sigma = \log N_M(t) - \log Q_c(t) + bM \quad (4.6)$$

Both models are updated according to Chapter 2, with increasing time windows of six hour lengths. The parameters determined for bin t_i are used to forecast seismicity for bin t_{i+1} , where the forecast bin has a length of six hours. Chapter 2 evaluates several approaches to determine the best set of parameters (compare table 2.1), as a starting point I determine the fit of the SSF sequence with the best-fitting real-time model (E5). Mena & Wiemer (2011) similarly examine different approaches for the fit of the parameters for the model by Shapiro et al. (2010); analogue to above, the their real-time model that updates the seismogenic index Σ and the b -value for each bin (called SR in Mena & Wiemer (2011)) is used here.

The model by Shapiro et al. (2010) depends on the injection rate; when the rate is zero, no events are forecast. To be able to compare the performance of the two models, the analysed period is therefore limited to the first injection test, i.e. the first 15.25 days of the sequence (Figure 4.12).

The start of the first bin coincides with the occurrence of the first event on 16.09.1993, 4.23pm. The first two bins show zero observed events, as no events above the completeness magnitude $M_c = -1$ are observed.

4.3.2.2 Performance Evaluation

According to Chapter 2, the performance of the two models is evaluated with the N(umber)-test (Lombardi & Marzocchi, 2010; Werner et al., 2010; Woessner et al., 2011) and the L(ikelihood)-test (Schorlemmer et al., 2007, 2010). The N-test compares the total number of observed earthquakes with the forecast rates and indicates whether too few or too many events are forecast. The daily rejection ratio R_N (Table 4.1) indicates the fraction of bins that are rejected according

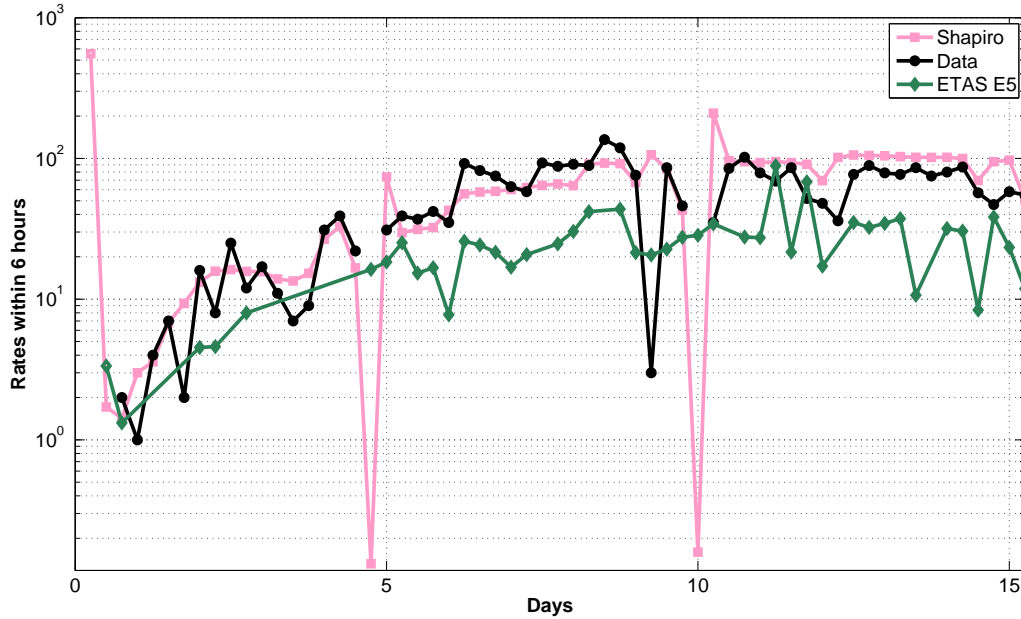


Figure 4.12: Modelling results of the SSF sequence for Shapiro’s model (pink) and the ETAS E5 model (green), the observed data is indicated in black. Technical difficulties led to data gaps at 4.75 and 10 days, which are shown as bins with 0 observed events.

to this test. The L-test evaluates whether the forecast number of events and the distribution in the magnitude bins is consistent with the observation, again assuming the entire volume as one spatial bin. For each magnitude bin I compute the log-likelihoods and sum this to a joint log-likelihood of the forecast. To verify that the joint log-likelihood is consistent with what is expected if the model is correct, I simulate 10,000 synthetic catalogues consistent with the forecast model and compute their log-likelihood values. This distribution of likelihood values is then compared with the observed log-likelihood. The quantile score γ then measures the amount of simulated log-likelihood values that are smaller than the observed log-likelihood. This test is one-sided and rejects a model if $\gamma < 0.025$, which implies that the observed log-likelihood is much smaller than would be expected if the model is true. According to the N-Test, the daily rejection ratio R_L is defined as fraction of test bins that do not pass the L-test.

| Name | Type | R_N | R_L | Joint Log Likelihood |
|------|---------|-------|-------|----------------------|
| SR | Shapiro | 0.60 | 0.55 | -1505.40 [-658.22] |
| E5 | ETAS | 0.82 | 0.84 | -1865.79 [-1853.54] |

Table 4.1: Quantitative evaluation of model forecasts: Model name, model type, fraction of rejected time bin in N-Test, fraction of rejected time bins in L-Test, and joint log-likelihood of the each model. The joint log likelihoods in the brackets indicate the corrected values, where bins containing no data are excluded.

While the visual fit of the SR model in Figure 4.12 is good, the joint log likelihood (JLL) is relatively low. The first bin uses the generic value of $\Sigma = 0.5$, introduced by Mena & Wiemer (2011), this leads to an overpredictions of the rates in this bin (Figure 4.12). Additionally, technical difficulties lead to data gaps for several bins (Figure 4.12 at 4.75 and 10 days). As the forecast of the SR model highly depends on the injection rate, the lack of information about the injection rates in this bin leads to a forecast value close to zero. The corrected JLL value, that excludes these three bins is indicated in the brackets in Table 4.1, the value is significantly higher.

As already observed in Figure 4.12, table 4.1 indicates that the performance of the ETAS model E5 is poorer than the Shapiro model. The ETAS model under predicts the rates in most bins, which leads to only around 20 % of the bins being accepted by both tests. The generic starting values of the ETAS model lead to a better fit for the first bin than the generic value of the SR bin and the data gaps do not have high influence on the performance of the E5 model, removing these bins therefore does not have an influence on the JLL (in brackets in Table 4.1). However, the overall performance of the ETAS model is poorer than Shapiro's model.

Comparing Table 4.1 with Table 2.2 from Chapter 2 indicates that the overall fit of the two models to the SSF sequence is worse than for the Basel sequence. While the best-fitting model E5 has a rejection rate R_L of only 0.15 for the Basel data, the lowest R_L for the models in this chapter is 0.52.

4.3.2.3 Hazard Integration

Similar to Chapter 2, I translate the rates forecast for the SSF sequences in to probabilities of exceeding EMS intensities, using standard procedures introduced originally by Cornell (1968). Hazard is the result of a combination of seismic rates, their frequency–size distribution and the Ground Motion Prediction Equation (GMPE) and its uncertainty. A direct comparison with the maximum hazard of the Basel sequence (blue in Figure 4.13) indicates that the maximum hazard of the SSF sequence (red) is much lower.

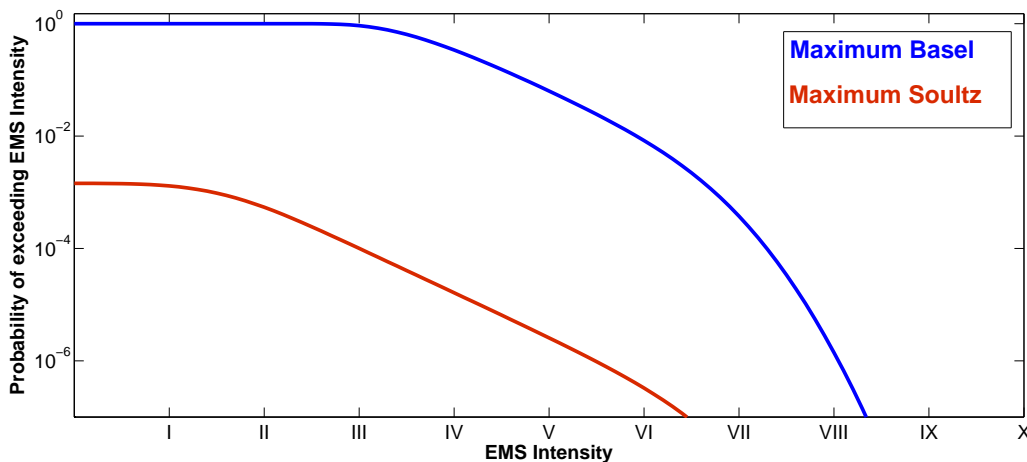


Figure 4.13: Hazard curves based on model SR. Probabilities of exceeding EMS Intensities I to X for the maximum observed values for Basel (blue) and the Soutz-sous-Forêts sequence (red).

4.3.3 Seismogenic Index

An important parameter of Shapiro’s model is the seismogenic index Σ (Equation 4.6). Shapiro et al. (2010) compare Σ for different sites and conclude that the Basel data showed one of the highest values of Σ . Figure 4.14 indicates the time-evolution of the seismogenic index for Basel and for two injections of the SSF sequence. The first index is 0.5 for all sequences, as Mena &

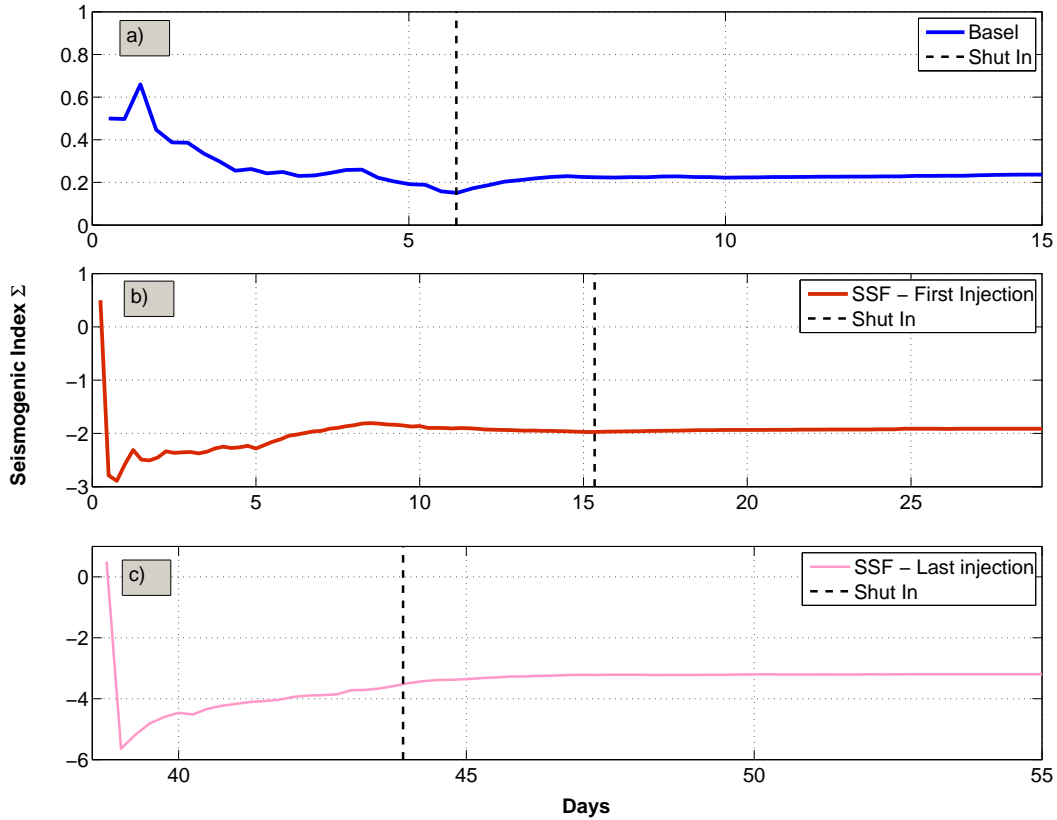


Figure 4.14: Evolution of seismogenic index Σ with time for a) Basel, b) the first injection in SSF and c) the third injection in SSF. The respective shut in is indicated in all three panels. The starting value is 0.5 for all three sequences.

Wiemer (2011) choose that as a generic starting value. The seismogenic index for Basel first increases and then stays constant around a value of 0.25; with a mean $\Sigma_{Basel} = 0.25 \pm 0.08$. For the first injection of the SSF sequence (Fig. 4.14b), the seismogenic index is significantly smaller at around -2. Ignoring the first bin with $\Sigma = 0.5$ leads to $\Sigma_{SSF1} = -2.08 \pm 0.25$. The third injection of the SSF sequence shows even smaller values of Σ , $\Sigma_{SSF2} = -3.54 \pm 0.54$ (again by ignoring the first bin).

Shapiro et al. (2010) compare the seismogenic index for different regions and find lower values for hydrocarbon reservoirs than for geothermal reservoirs (compare Figure 3 in Shapiro et al.

(2010)). The highest values they find are found of the Basel sequence for which they find $\Sigma = 0.2 \pm 0.7$. The values of the SSF sequence I find here are in the lower range of the geothermal reservoirs, along with values found for the Ogachi (Kaieda et al., 1993) and Paradox Valley (Ake et al., 2005) geothermal reservoirs.

4.4 Conclusions

Adapting the methods developed in Chapters 2 and 3 to the seismic sequence of one injection test in Soultz-Sous-Forêts helps to emphasise their general validity and affirms that they are not characteristic to the Basel sequence alone.

Even though the seismicity from the SSF sequence is more complex, as it was induced through several injections at different depths, the spatio-temporal distribution of the b -values resembles the one of the Basel sequence. Higher values are found near the open hole section and lower values further away and later into the sequence. This affirms that the model developed in Chapter 3, linking the pore pressure evolution to the spatial distribution of the b -values, can be used to describe other induced seismicity sequences.

To forecast the ongoing seismicity of the first injection in 1993, I start by using two different approaches; the best-fitting real-time model of Chapter 2 and a model introduced by Shapiro et al. (2010). Expanding the dataset that these models have been tested on is an important step towards Induced Seismic Hazard Assessment (ISHA). More sequences have to be tested and possibly more models should be integrated. Their respective performances is an essential input for any weighting of the models. Only this can lead to a successful development of a probability-based alarm system for future EGS projects.

The seismogenic index of the SSF sequence indicates that the activity during this sequence was significantly lower than during the Basel sequence. Additionally, the probabilities of exceeding EMS intensities I to X are also significantly lower as well. These two results both indicate that

the 1993 injection at the SSF was more suited for a successful EGS project. However, more recent injections at the SSF site showed larger magnitude events, which also were felt by the population (Cuenot et al., 2010). The seismicity induced by these injections remains to be analysed with the methods introduced here.

References

- Ake, J., Mahrer, K., Connell, D. O., & Block, L., 2005. Deep-injection and closely monitored induced seismicity at paradox valley, colorado, *Bull. Seismol. Soc. Am.*, **95**, 664–683.
- Aki, K., 1965. Maximum likelihood estimate of b in the formula $\log n = a - bm$ and its confidence limits, *Bull. Earthquake Re. Inst., Tokyo Univ.*, **43**, 237–239.
- Baria, R., Garnish, J., Baumgärtner, J., Gerard, A., & Jung, R., 1995. Recent developments in the European HDR Research programme at Soultz-sous-Forets (France), in *Proceedings of the World Geothermal Congress, 1995*, pp. 2631–2637, Florence.
- Bender, B., 1983. Maximum likelihood estimation of b values for magnitude grouped data, *Bull. Seismol. Soc. Am.*, **73**(3), 831–851.
- Conover, W. J., 1972. A Kolmogorov Goodness-of-Fit Test for Discontinuous Distributions, *Journal of the American Statistical Association*, **67**(339), 591–596.
- Cornell, C., 1968. Engineering seismic risk analysis, *Bull. Seismol. Soc. Am.*, **59**(5), 1583–1606.
- Cuenot, N., Dorbath, L., Frogneux, M., & Langet, N., 2010. Microseismic activity induced under circulation conditions at the egs project of soultz-sous-forêts (france), in *Proceedings World Geothermal Congress 2010*, pp. 1 –9.
- Cuenot, N., Charlety, J., Dorbath, L., & Hässler, H., 2006. Faulting mechanisms and stress regime at the European HDR site of Soultz-sous-Forets, France, *Geothermics*, **35**(5-6), 561–575.
- Dorbath, L., Cuenot, N., Genter, A., & Frogneux, M., 2009. Seismic response of the fractured and faulted granite of Soultz-sous-Forets (France) to 5 km deep massive water injections, *Geophys. J. Int.*, **177**(2), 653–675.
- Evans, K. F., Moriya, H., Niitsuma, H., Jones, R., Phillips, W. S., Genter, A., Sausse, J., Jung, R., & Baria, R., 2005. Microseismicity and permeability enhancement of hydrogeologic structures during massive fluid injections into granite at 3 km depth at the Soultz HDR site, *Geophys. J. Int.*, **160**(1), 388–412.

REFERENCES

- Gutenberg, B. & Richter, C. F., 1942. Earthquake magnitude intensity, energy, and acceleration, *Bull. Seismol. Soc. Am.*, **32**, 163–191.
- Jones, R., Beauce, A., Jupe, A., Fabirol, H., & Dyer, B., 1995. Imaging Induced MicroSeismicity During the 1993 Injection Tests at Soultz-sous-Forets, in *Proceedings of the World Geothermal Congress, 1995*, pp. 2665–2669, Florence.
- Kaieda, H., Kiho, K., & Motojima, I., 1993. Multiple fracture creation for hot dry rock development, *Trends in Geophysical Research*, **2**, 127–139.
- Lombardi, A. M. & Marzocchi, W., 2010. The Assumption of Poisson Seismic-Rate Variability in CSEP/RELM Experiments, *Bull. Seismol. Soc. Am.*, **100**(5A), 2293–2300.
- Mena, B. & Wiemer, S., 2011. Building robust models to forecast the induced seismicity related to geothermal reservoir enhancement, *in prep.*
- Ogata, Y., 1988. Statistical-models for earthquake occurrences and residual analysis for point-processes, *Journal of the American Statistical Association*, **83**(401), 9–27.
- Ogata, Y., 1999. Seismicity analysis through point-process modeling: a review, *Pure appl. geophys.*, **155**, 471–507.
- Schorlemmer, D., Gerstenberger, M., Wiemer, S., Jackson, D., & Rhoades, D., 2007. Earthquake likelihood model testing, *Seismol. Res. Letts.*, **87**, 17–29.
- Schorlemmer, D., Zechar, J., Werner, M., Field, E., Jackson, D., Jordan, T., & Group, T. R. W., 2010. First results of the regional earthquake likelihood models experiment, *Pure appl. geophys.*, **167**(8-9), 859–876.
- Shapiro, S. A. & Dinske, C., 2009. Fluid-induced seismicity: Pressure diffusion and hydraulic fracturing, *Geophysical Prospecting*, **57**(2), 301–310.
- Shapiro, S. A., Dinske, C., Langenbruch, C., & Wenzel, F., 2010. Seismogenic index and magnitude probability of earthquakes induced during reservoir fluid stimulations, *Leading Edge*, **29**(3), 304–9.
- Utsu, T., 1961. A statistical study of the occurrence of aftershocks, *Geophys. Mag.*, **3**, 521–605.
- Utsu, T., 1999. Representation and analysis of the earthquake size distribution: A historical review and some new approaches, *Pure appl. geophys.*, **155**(2-4), 509–535.
- Werner, M. J., Zechar, J. D., Marzocchi, W., Wiemer, S., & CSEP-Italy Working Grp, 2010. Retrospective evaluation of the five-year and ten-year CSEP-Italy earthquake forecasts, *Annals of Geophysics*, **53**(3), 11–30.

REFERENCES

- Wiemer, S. & Wyss, M., 2000. Minimum magnitude of complete reporting in earthquake catalogs: examples from Alaska, the Western United States, and Japan, *Bull. Seismol. Soc. Am.*, **90**, 859–869.
- Woessner, J. & Wiemer, S., 2005. Assessing the quality of earthquake catalogues: Estimating the magnitude of completeness and its uncertainty, *Bull. Seismol. Soc. Am.*, **95**(2), 684–698.
- Woessner, J., Hauksson, E., Wiemer, S., & Neukomm, S., 2004. The 1997 Kagoshima (Japan) earthquake doublet: A quantitative analysis of aftershock rate changes, *Geophys. Res. Lett.*, **31**.
- Woessner, J., Hainzl, S., Marzocchi, W., Werner, M. J., Lombardi, A. M., Catalli, F., Enescu, B., Cocco, M., Gerstenberger, M. C., & Wiemer, S., 2011. A Retrospective Comparative Test for the 1992 Landers Sequence, *J. Geophys. Res.*, (B05305).

Chapter 5

Reliability of the Probability-Based Magnitude of Completeness Method ¹

Corinne E. Bachmann, Danijel Schorlemmer, Jochen Woessner and Stefan Wiemer

¹In preparation to be submitted to *Bulletin of the Seismological Society of America* as C.E. Bachmann, D. Schorlemmer, J. Woessner and S.Wiemer *Reliability of the Probability-Based Magnitude of Completeness*

Abstract

The analysis of the completeness magnitude of a seismic dataset is crucial for all subsequent analysis of the data. We analyse here an approach introduced by Schorlemmer and Woessner that determines the completeness as a function of the performance of the seismic network and its stations – the probability-based magnitude of completeness (PMC) method. We analyse different aspects of this method with the example of the Northern Californian Seismic Network (NCSN). The influence of an independent subnetwork on the completeness estimate, is examined with the example of a subnetwork monitoring the Geysers geothermal field. This subnetwork operates with under its own triggering conditions, but feeds its data into the NCSN. To analyse the effect of spurious probabilities from single stations, we introduce a threshold that determines the minimum contribution on the completeness estimate of each station. This threshold affirms that no stations with negligible probabilities are included in the calculation. As the real value of the completeness can not be known, we present here our choice of parameters towards the most reliable value. We present three different maps, based on the parameters of our choice, for the NCSN, 1) the probability-based magnitude of completeness, 2) the probability to record magnitude M1 and 3) M3 events. We estimate that no magnitude M3 event should be missed within the authoritative region of the NCSN.

5.1 Introduction

The Probabilistic Magnitude of Completeness (PMC) method was introduced by Schorlemmer & Woessner (2008) as a novel approach to assess and map the monitoring capability of seismic networks in space and time based on the performance of each station in the network. Knowledge on the completeness reporting is a critical input parameters for many seismological and hazard related studies (e.g. Wiemer et al., 2009). One of the base motivations to introduce a

new method was to step away from the dependence of a finally produced earthquake catalogue of a network and to use the originally recorded, empirical data. With the latter, the space–time complexity can be addressed in more detail; however, being able to resolve more details also requires a more complex model and PMC in this case is dependent on the interplay of the network configuration and the capability of each station in the network to detect an event. In this paper we primarily attempt to resolve how this capability influences the products of the PMC method: the probability of detecting an event and its derivative, the probability-based magnitude of completeness.

PMC exploits recorded empirical data, in contrast to earthquake sample based methods. Thus, it makes use of the data at hand of a seismic network: The presence or absence of picks for a seismic station is evaluated at each station. This results in a matrix that describes the probability of detecting an event $P_D(M, L)$ of magnitude M at distance L at a particular station. Once this process is completed for all stations, the method allows to estimate detection probabilities $P_E(M, \vec{x}, t)$ for a given magnitude M and in addition the probability-based magnitude of completeness $M_P(\vec{x}, t)$ for a given probability threshold at location \vec{x} for the time t . Both, P_E and its derivative M_P , are computed for a minimum of N stations, depending on the network triggering conditions. The probabilities are derived by summing the contributions of all probability station-matrices for the respective magnitude and distance bins. As a final result, a space–time model of the probability-based magnitude of completeness at any pre-defined probability level P can be defined (Schorlemmer & Woessner, 2008).

PMC, while more resource demanding than classical approaches to estimate the completeness magnitude M_c from earthquake sample based on the assumption of a power-law scaling of magnitudes (e.g. Amorese, 2007; Mignan et al., 2011; Wiemer & Wyss, 2000; Woessner & Wiemer, 2005), is a very attractive and elegant approach, which was highlighted also as a BSSA publication. The PMC method has already been applied to various seismic networks worldwide: the Southern Californian Seismic Network (SCSN) (Schorlemmer & Woessner, 2008),

the Swiss Seismic Network (SSN) (Nanjo et al., 2010), the network of the Japan Meteorological Agency (JMA) (Nanjo et al., 2008), the Italian National Seismic Network operated by the Istituto Nazionale di Geofisica e Vulcanologia, Rome, Italy (Schorlemmer et al., 2010), the network of the Istituto Nazionale di Oceanografia e Geofisica Sperimentale in Trieste, Italy (Gentili et al., 2011), and the network of the Mponeng gold mine in Carletonville, South Africa, operated by the Japanese-German Underground Acoustic Emission Research in South Africa (JAGUARS) project (Plenkens et al., in revision). Various aspects of the method were addressed in these studies, e.g. comparison with earthquake sample based methods, implementation as a network planning tool, scenario computations for network outages, estimation of the number of undetected events, and definition of areas for testing prospective earthquake forecasts. For these applications, also time histories of probability-based magnitude of completeness maps were computed; results of these ongoing activities are presented at the dedicated web-site (www.completenessweb.org) together with software packages.

The major advantages of the PMC method are that the completeness estimate is independent of an assumption on power-law scaling of the magnitude–frequency distribution, that the model can be well extrapolated into regions of low or no seismicity, and that it allows for scenario analysis such as network planning. The probability-based magnitude of completeness M_P defines completeness at a point in space and time while the traditional, Gutenberg-Richter based, methods of estimating magnitude of completeness M_c define completeness for a spatio-temporal volume. Therefore, the values of both methods are not directly comparable; however, the PMC method can also be used to create completeness estimates for spatio-temporal volumes (Nanjo et al., 2010).

While many successful applications of PMC have been presented, some basic methodological aspects yet have not been entirely investigated. In this study we address the question how many stations are necessary to be included in the computation of $P_E(M, \vec{x}, t)$ and which criteria on the station detection probabilities may have to be used to limit the number of stations. In

simple words one could ask: Does a station located more than e.g. 100km from an M 1.5 type event need to be considered to compute earthquake detection probabilities? If so, would this station still be relevant for the estimating the completeness level? In terms of the approach, the question is more properly stated as follows: What is the lowest probability level for a station detection probability P_D that is still substantial and reliable to be used in the computation of event detection probabilities and how is it affected by internal smoothing procedures?

We address these questions by introducing a cut-off threshold value parameter, p_t , of incremental probabilities. This parameter emerges as a hidden parameter in the PMC approach, unravelled in this study targeted to the Northern Californian Seismic Network (NCSN), but also from investigating large networks like the JMA network, (Schorlemmer, 2009). For the latter, Schorlemmer (2009) limited for each point in space and time the set of stations to N_{\max} stations that have the highest detection probabilities. This maximum number was used unconditionally and was previously estimated in sensitivity tests. However, by ordering the stations by their detection probabilities, one can choose a suitable incremental probability cut-off threshold p_t . As a consequence, the probability-based magnitude becomes a function of the probability threshold P and the cut-off threshold p_t . As will be shown, choosing these values results in a trade-off between the two parameters levelled by users confidence – up-to-date, it remains a subjective choice with no real optimisation procedure available, as the true M_p is not known. This situation is well known for other highly relevant problems in seismology: for example, the earthquake location problem always suffers from not knowing the true velocity structure which in general leads to at least slightly erroneous locations (Wang et al., 2010). A fortunate side effect of limiting the amount of contributing stations with the above outlined approach is to effectively reduce computation times.

A second topic we address here is the influence of subnetworks on the entire network detection capabilities that do not follow the same triggering conditions as the main network. This is crucial for large networks collecting data also from smaller, more targeted networks. We apply the

PMC method to the Northern Californian Seismic Network (NCSN). This network includes more than 500 stations and requires five stations to trigger any event. The NCSN is a perfect target network for this study not only because of its large amount of stations but also for investigating the effect of subnetworks. We have to distinguish between two types of subnetworks:

Integrated subnetworks feed their data directly to the main operating centre where triggering and locating is based on all incoming data streams. For the operating centre, stations of such a subnetwork do not differ from stations of the main network, they are only operated and maintained by a different institution. Therefore, integrated subnetworks simply provide real-time station data of their stations to the main network, essentially becoming part of the main network. Schorlemmer & Woessner (2008) showed how strong the influence of the Anza subnetwork on the recording completeness of the SCSN in the Anza area is and how it complements the main network in this area.

Independent subnetworks run their triggering algorithm and locate events using only their stations and subsequently feed the catalogue of located earthquakes to the operational centre of the main network. Thus, these networks may record data under different triggering conditions than the main network, adapted to the needs of their region and often ignoring events outside the core region of the subnetwork. Such networks need to be considered completely separate from the main network; only the earthquake catalogue of the main network is becoming a composite catalogue, containing events from different networks.

We show how data of independent subnetworks can influence the recording probabilities of single stations and that the data of these subnetworks have to be removed prior to the analysis.

5.2 Data

All data used in this study are provided by the Northern California Seismic Network (NCSN). The NCSN combines data from several subnetworks from which we only use the integrated networks in the period 1 January 2008 to 1 January 2011. This results in a total number of 503 stations that were in operation during this period and that recorded at least one event. Table 5.1 lists all subnetworks and their respective number of stations that were used in our analysis. The NCSN comprises several independent subnetworks which do not need to be considered in completeness assessments. These are mainly local, temporary, or borehole networks. To show the effects of earthquake data coming from independent subnetworks on the detection probabilities of the stations in the main network, we analyse here the Calpine/Lawrence Berkeley Labs (BG) seismic network which is installed to monitor the Geysers Geothermal Field. The location of all stations are marked with triangles in Figure 5.1, the inset marks the independent BG network.

| Network code | Network name | No. of stations |
|--------------------------------|--|-----------------|
| NC | Northern California Seismic Network | 351 (374) |
| Integrated subnetworks | | |
| BP | Parkfield High Resolution Seismic Network | 12 (13) |
| BK | Berkeley Digital Seismic Network | 42 (46) |
| NN | UNR Broadband Network | 55 (85) |
| PG | Pacific Gas and Electric Seismic Network | 23 (29) |
| WR | California Water Resources | 17 (23) |
| Independent subnetworks | | |
| BG | Calpine/Lawrence Berkeley Labs Seismic Network | 25 (25) |

Table 5.1: Networks of the Northern California Seismic Network that we used in this analysis. The third column indicates the number of stations that were in operation on 1 January 2011 and that recorded at least one event during our study period. In brackets we report the number of stations that were in operation during the study period from 1 January 2008 to 1 January 2011 and that recorded at least one event. Detailed information about the networks is available online at <http://www.ncedc.org/ncedc/station.info.html>.

During the study period, the NCSN and its subnetworks recorded 71816 events; they are

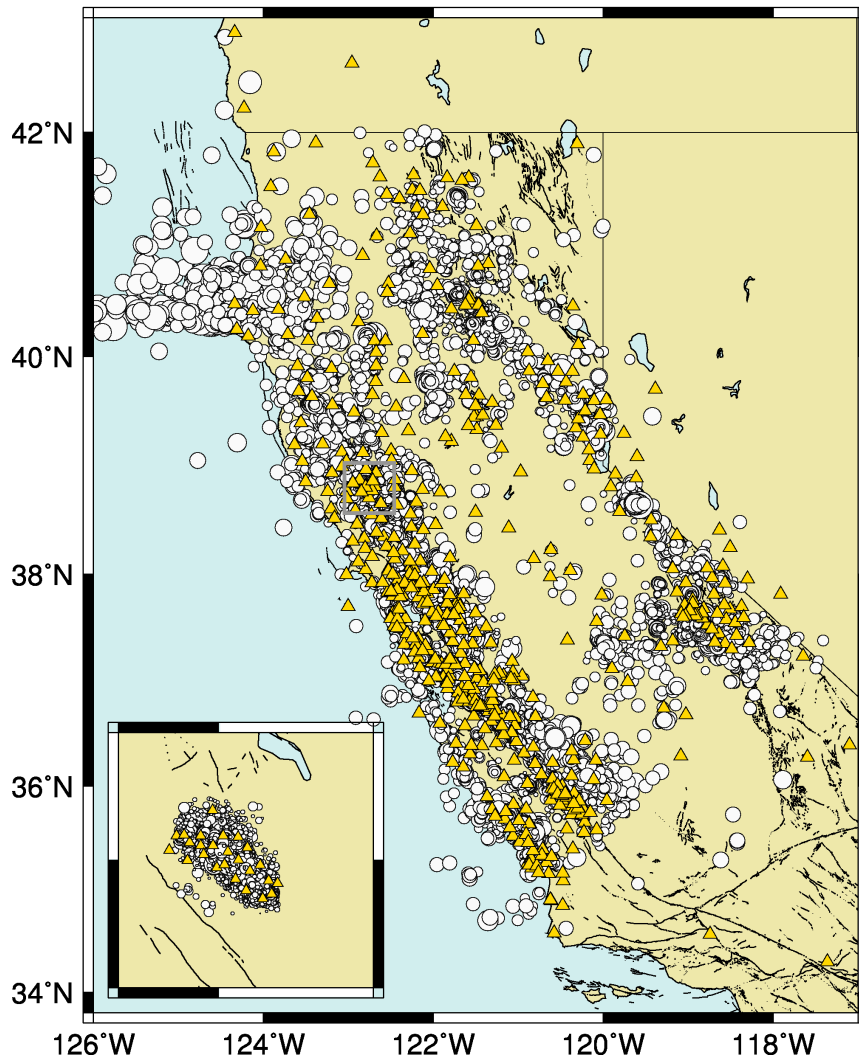


Figure 5.1: Events recorded by the Northern Californian Seismic network (white circle, sizes are scaled by magnitude), stations are marked with yellow triangles. The inset (location marked in grey) indicates the stations of the independent subnetwork BG and the events recorded by this network.

marked as white circles in Figure 5.1. The NCSN uses the local magnitude definition M_L by Eaton (1992), leading to magnitudes ranging from $M_L = 0$ to 6.5. To initiate the location procedures, P-phases on at least five stations have to be recorded.

The BG network is an independent network and is designed to only record events within the Geysers geothermal field. Events outside this field are generally removed either automatically or manually, as the locations are not reliable. However, some events remain outside the field recorded by this network. We manually remove events detected in the target region of this network as follows: From the latitude and longitude distribution of the located events, we determine the mean and standard deviation, then we remove all events that fall within the latitudes $38.81N \pm 0.09$ and longitudes $122.78W \pm 0.1$, an amount of 27515 events. The removed events are marked in the inset in Figure 5.1. They account for approximately 30% of the whole activity in Northern California and are substantially smaller than events recorded by the NC and its integrated subnetworks; 71% with $M \leq 1$ compared to 54% $M \leq 1$. Removing the events of the BG network leads to 44301 events that will be used in the subsequent analysis.

5.3 Method

Other than traditional methods to determine catalogue completeness, which assume that earthquake samples follow the Gutenberg-Richter distribution (Gutenberg & Richter, 1942), the method of Schorlemmer & Woessner (2008) is based on empirical data alone. The method requires 1) the station metadata, such as the location and the active time, 2) phase picks of each event with the information which station recorded the event and 3) the magnitude–distance attenuation relation of the network.

The analysis itself consist of two basic steps; a) derivation of station detection probabilities $P_D(M, L)$ and b) computation of either the probability of detection an event $P_E(M, \vec{x}, t, \rho_t)$ or the probability-based completeness magnitude $M_P(\rho, \vec{x}, t, \rho_t)$ at a given point in space and time.

For the derivation (a), we need to define a period for which the recording chain did not change. Such changes may include an alteration of the network triggering condition or changes in the magnitude definition. A trade-off exists between homogeneity and amount of data: longer periods lead to a larger dataset, but this is likely to be less homogeneous; shorter periods assure homogeneity but reduce the amount of data to derive detection probabilities. We import the station metadata; which includes the operation time, the station location and the subnetwork to which it belongs. The station operation time should at least partly fall within the chosen study period and the station has to be involved in triggering the automatic location as outlined above. Next, we import the P-phase information of each event, containing the information about which stations recorded the event together with its location and time. For this step, it is important to have accurate information about station down-times, as an event will be assigned as missed by the station if the station has not been recorded as offline. According to Schorlemmer & Woessner (2008), we then calculate the station detection probability $P_D(M, L)$ to detect an earthquake with a certain station at a given magnitude-distance combination.

The derivation (b) generates two primary outputs: (1) maps of the detection probability $P_E(M, \vec{x}, t, p_t)$ for magnitude $M(\vec{x}, t)$ at each location and time and (2) maps of the probability-based magnitude of completeness $M_P(P, p_t, \vec{x}, t)$ for a selected probability threshold P . Both maps are calculated using basic combinatorics. The NCEDC triggers an event after five stations record a signal. To determine the probability $P_E(M, \vec{x}, t)$ that five stations or more record an event with magnitude M at the location \vec{x} at time t , we calculate 1 minus the probability that either 0, 1, 2, 3 or 4 stations have triggered the event. This means sampling 0, 1, 2, 3 or 4 stations out of the total number of stations with a probability to record M at location \vec{x} higher than 0. The possible amount of combinations is equal to the sum of the binomial coefficients $C(n, k)$ where n is the number of involved stations and k is 0 to 4. Figure 5.2 illustrates the increasing number of possible combinations with the increasing number of involved stations. It also highlights the difference if either four or five stations are involved in the triggering. The difference in

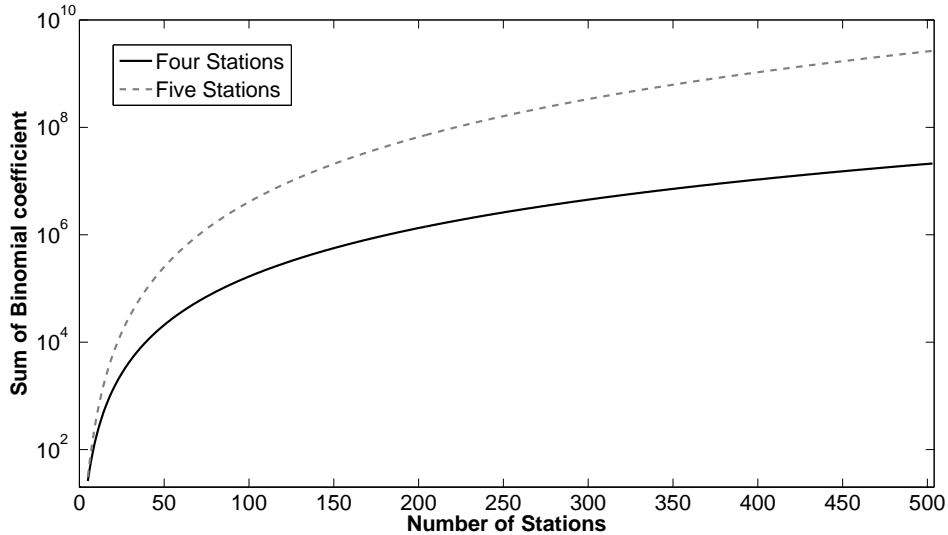


Figure 5.2: Sum of binomial coefficients $C(n,k)$, where n is the number of involved stations and k is 0 to 3 for four station triggering and 0 to 4 for five station triggering. The difference in possible combinations for four stations and five stations triggering increases exponentially.

the possible combinations increases exponentially with the number of involved stations and is a factor of 100 higher for five station triggering when the maximum possible number of 503 stations are used.

We now introduce a different way of the sampling for the synthesis: First we sort all stations by their detection probabilities in descending order. During each completeness-magnitude computation, we calculate the contribution Δp of each station from the sorted list to the resulting detection probability P_E of the network. If the contribution of a stations falls below the predefined threshold p_t , we stop the computation. No additional stations are then considered to calculate the resulting completeness magnitude M_P . Setting this threshold to very small values prevents from including stations with insignificant detection probabilities in the computation; at $p_t = 0$, all stations are used resembling the original approach. The larger p_t , the fewer stations will be considered.

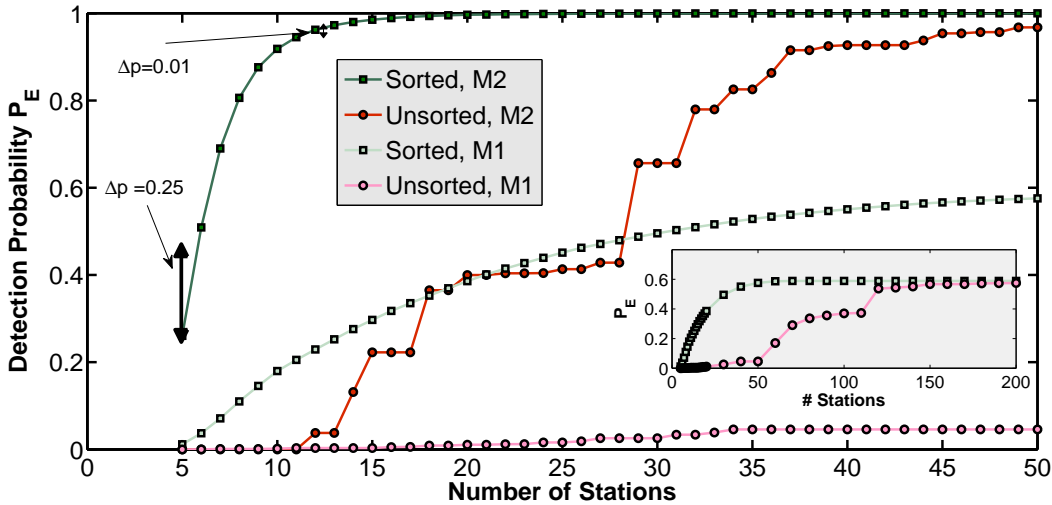


Figure 5.3: Increase of the probability to detect an event of magnitude M 1 and 2 with increasing station numbers: 1) sorted by distance (red) and 2) sorted by probabilities (green). The arrows indicate the increase in the combined probability Δp for two cases.

As a visual reasoning for the new method, we display the difference of the two approaches when either selecting according to distance or according to probabilities for an arbitrarily chosen location and two magnitudes $M=1$ and $M=2$ from our study region. We plot the detection probability P_E at this location (x,y) as a function of increasing number of contributing stations (Figure 5.3). While the curves increase monotonically for the probability-sorted approach (green lines), the probabilities increase in jumps for the distance-sorted case (red lines). The two approaches converge to the same probability level for $M=2$ after 50 contributing stations, however, it takes over 120 stations for $M=1$ until both converge (see inset in Figure 5.3).

For the probability-sorted approach, the first five stations have probabilities of $P(M = 2, \vec{x}) = [0.90 \mid 0.81 \mid 0.80 \mid 0.70 \mid 0.64]$ leading to the combined probability of $P_E = 0.26$. The sixth station has $P(M, \vec{x}) = 0.60$, leading to $P_E = 0.51$, thus adding $\Delta p = 0.25$ (black arrow in Figure 5.3) to the detection probability P_E . The eleventh station in the example shown in Figure 5.3 has $P(M, \vec{x}) = 0.40$, the increase in P_E however is only $\Delta p = 0.01$, leading to $P_E = 0.97$. We

do not increase the station number if $\Delta p < p_t$. By comparing this process with the increase in the distance-sorted case (red curves in Fig. 5.3), we see that the probability P_E would first of all be reached much later and a criteria would be impossible to define as ΔP is not at all a function of the number of stations in this case. Figure 5.3 thus highlights that the proposed sorting approach optimises the computation and enables to define p_t .

5.4 Results

5.4.1 Station detection sensitivity distribution

Determining the detection probability P_E depends on the specific magnitude of the event and the location in the study area. To visualise the magnitude sensitivity of this step, we illustrate the probability of detecting an event with $M=(1.5,2.5)$ as a function of the station-to-node distance for all stations used in this study (Figure 5.4a and b, respectively). These function are equal to vertical columns in the station probability matrices P_D . Figure 5.4d and e illustrate two typical examples, the functions for station AFD (blue) and GZY (red) are added in Figures 5.4a and b and the selected vertical columns are highlighted in Figures 5.4d and e. The probabilities decrease with distance, a intentional result of the applied smoothing procedure; however the distribution of probability values from each station (indicated with light grey lines) is quite high and exceeds two standard deviations (green lines). The two highlighted stations GZY and AFD are considered good, based on a visual inspection of Figure 5.4d and e. However, the contribution to detect an different magnitude events varies strongly between the two stations: While AFD performs slightly better for larger magnitude events, GZY performance is better overall, especially for smaller magnitude events. Both fall well within the 2σ bounds of the entire distribution, yet they are different from a mean model of a station probability detection.

We can also summarise the uncertainty behaviour of $\sigma(P_D)$ as a function of the distance to

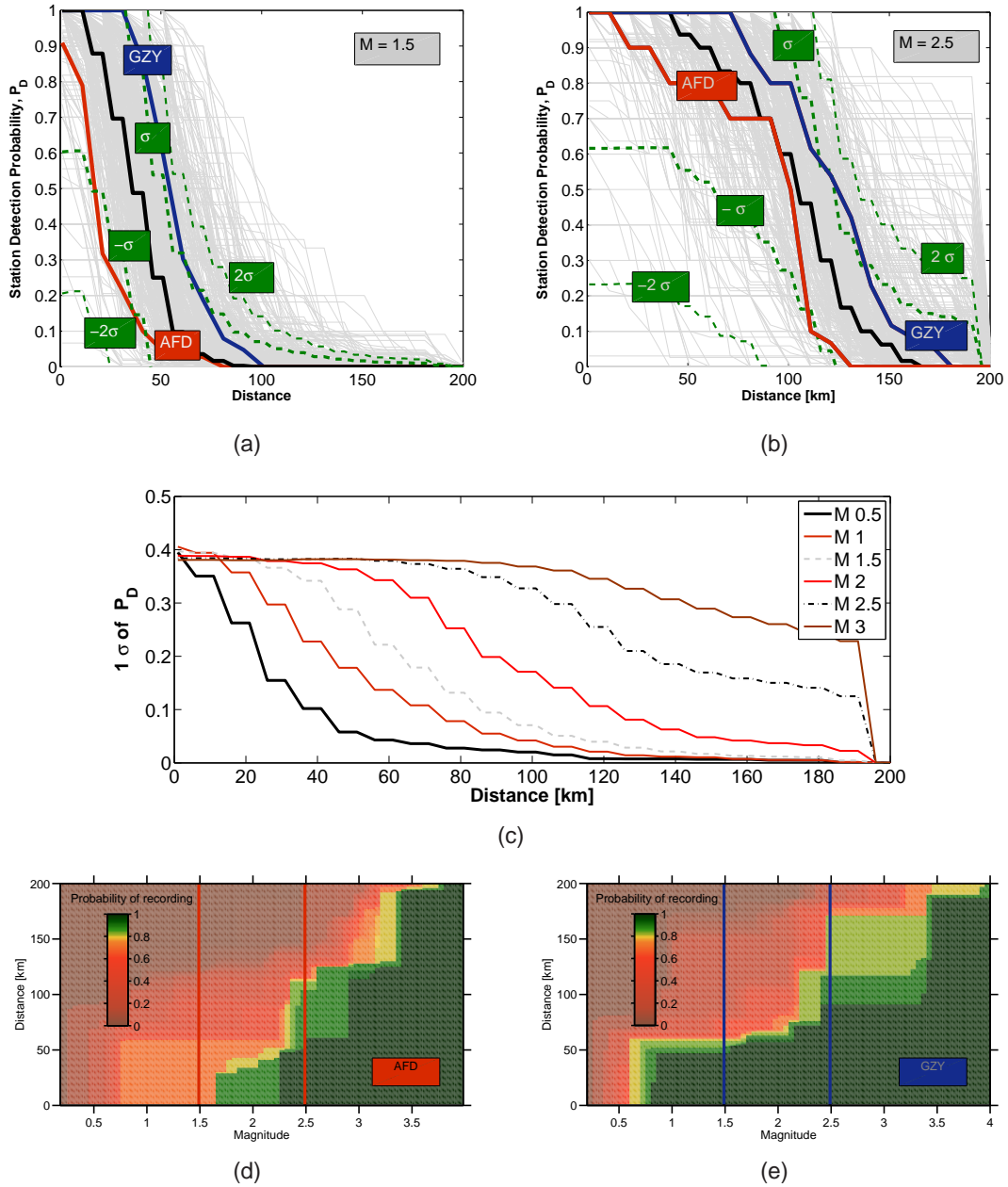


Figure 5.4: a) and b) Station detection probabilities P_E with distance for $M=1.5$ and $M=2.5$. The mean behaviour and one and two σ are indicated. c) One standard deviation σ of P_E for magnitude 0.5 to 3. d) and e) Example stations AFD and GZY, marked in blue and red in a and b.

the nodes (Figure 5.4c). We find consistently a decrease of $\sigma(P_D)$ with increasing distance, however, the decrease is strongly magnitude dependent. The smaller the magnitude, the faster the decrease of $\sigma(P_D)$. This varying uncertainty behaviour is likely a consequence of available data and the smoothing procedure as more uncertainties are mapped in the higher magnitude range due to less available data than compared to the small magnitude range.

5.4.2 Sensitivity to P and p_t

In the original approach by Schorlemmer & Woessner (2008) to compute M_P , only the probability threshold P needed to be selected; now, the additional cut-off parameter p_t needs to be defined when searching for the lowest magnitude detected with probability P at each node. Searching through all probabilities for one combination leads to a map of the probability-based magnitude of completeness $M_P(P, p_t, \vec{x}, t)$. Having two parameters available, the challenge is either to optimise for a best combination or to find an appropriate choice. Optimisation is not achievable as the true M_P is not known thus it remains in the end a decision to the user of the method.

We compute maps for the probability-based magnitude of completeness at the threshold level $P = 0.99$ and several levels of $p_t = 0(0.001, 0.01, 0.1)$. We then determine the difference in $\Delta(M_P)$, for $M_P(0.99, 0) - M_P(0.99, 0.001)$, $M_P(0.99, 0.001) - M_P(0.99, 0.01)$ and $M_P(0.99, 0.01) - M_P(0.99, 0.1)$ (Figure 5.5). The maps show an irregular pattern overall and they indicate that for $P = 0.99$ the differences increase with p_t approaching a value of $1 - P$. In addition, the maps point to locations that constantly show smaller and larger differences (black stars in Figure 5.5a-c). We select these spots and refine the computations by additionally varying the probability levels P . In Figure 5.6, we display the difference in calculated M_P colour-coded as a function of the two parameters at hand. The difference $\Delta(M_P)$ is computed with reference to $M_P(P = 0.9, p_t = 0)$. For all sub-plots, the difference $\Delta(M_P) = M_P(P = 0.9, 0) - M_P(P = x, p_t = y)$ increases with increasing P and p_t . We find that the differences in $\Delta(M_P)$ become largest in the

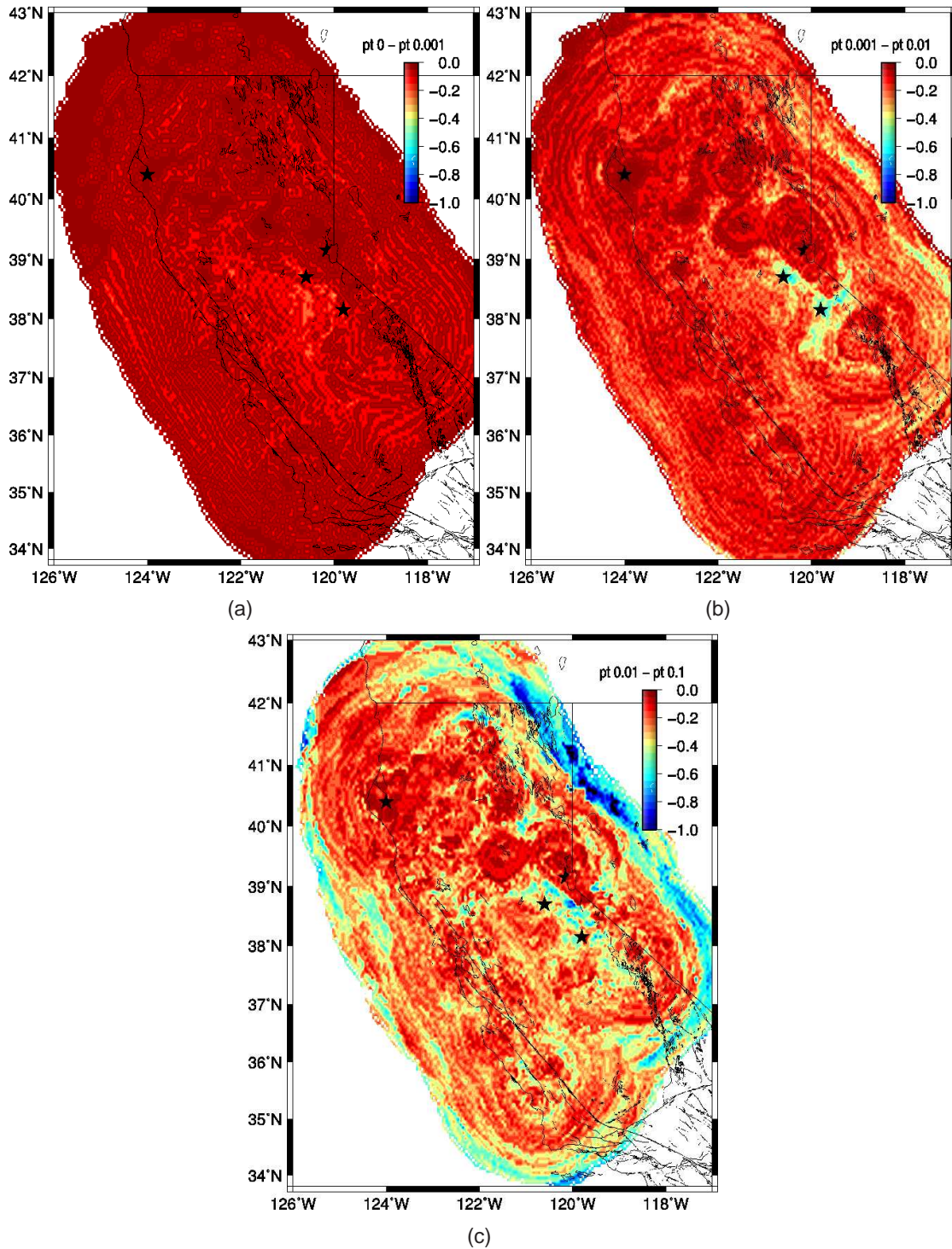


Figure 5.5: Differences in $\Delta(M_P)$ for a) $M_P(0.99, 0) - M_P(0.99, 0.001)$, b) $M_P(0.99, 0.001) - M_P(0.99, 0.01)$ and c) $M_P(0.99, 0.01) - M_P(0.99, 0.1)$. Stars mark the location of the detailed analysis in Figure 5.6

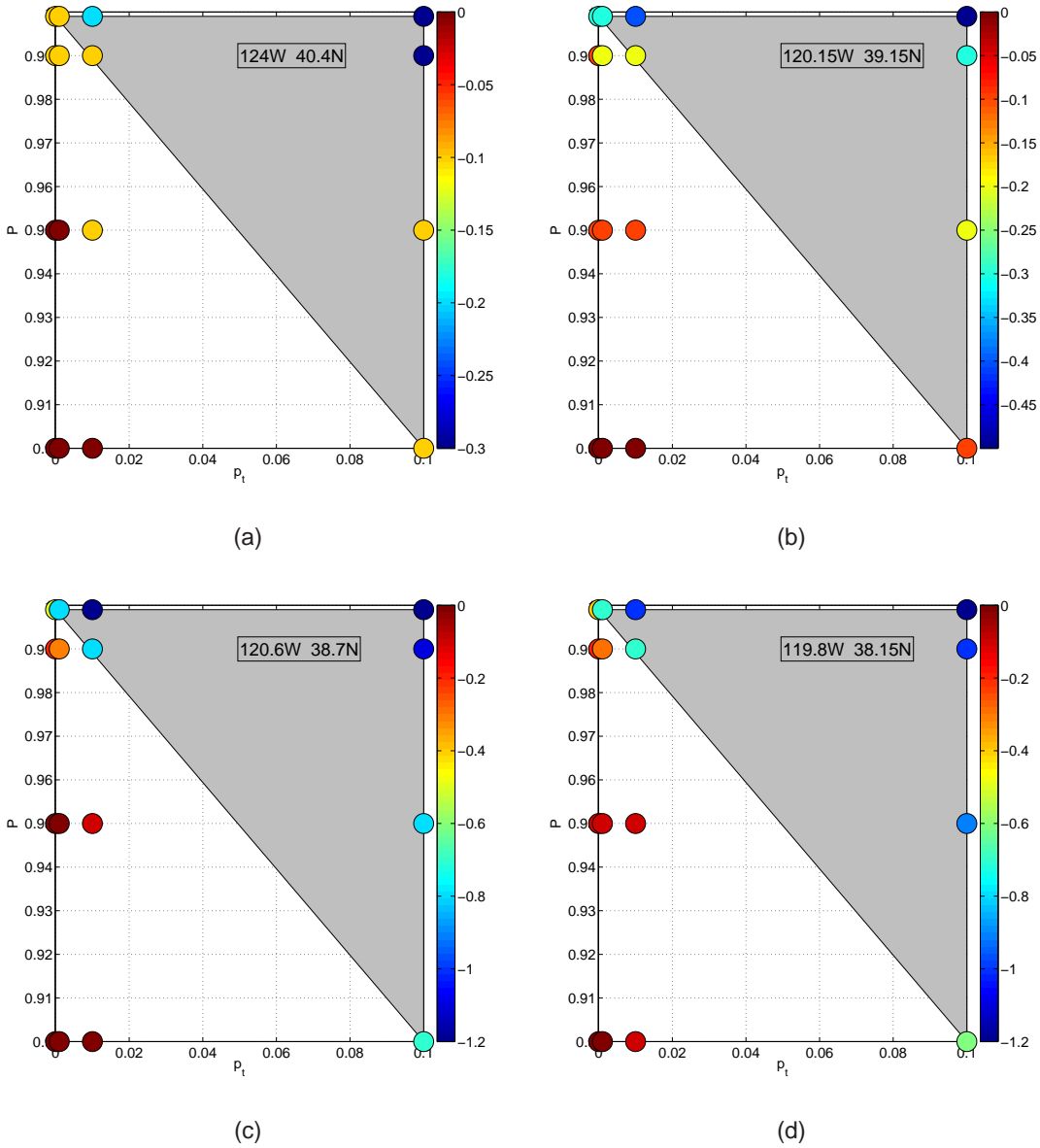


Figure 5.6: Relation between P and p_t for four different locations, marked by stars in Figure 5.5. The colour bar denotes the difference relative to $M_P(0.9, 0)$. While two locations (a and b) show relatively low differences for all combinations of P, p_t , the differences in c and d reach values up to $1.2 \Delta M_P$.

case of $p_t > 1 - P$, the shaded regions in the panels of Figure 5.6. We therefore suggest to use values of $p_t \leq 1 - P$.

5.4.3 Data Analysis – Removing data from a independent subnetwork

We remove events recorded by the Calpine/Lawrence Berkeley Labs Seismic Network (BG) as they are not recorded according to the triggering conditions of the NCSN. Figure 5.7 illustrates the effect of these events with the example of the data collected at the station KIP; recorded events are marked with green circles, missed events with red squares. The BG events (indicated with black crosses) are limited to a narrow distance band in Figure 5.7a. Removing these events and recalculating the station detection probabilities P_D (Figure 5.7c) leads to higher P_D within the affected distance range. Figure 5.7c indicates differences up to $\Delta(P_D) = 0.25$. This is not only the case for the station KIP, which is used here as an example. As we calculate the station detection probabilities P_D for a distance range up to 200km, all stations within this distance of the Geysers geothermal field are affected.

We find a mean difference of $\Delta M_p = 0 \pm 0.03$ with a maximum of 0.2 and a minimum of -0.3. A total of 1785 nodes show a difference $\Delta M_p \neq 0$ (Figure [refpic:kipd](#)); these nodes are distributed randomly over the area, indicating that there is no systematic difference. This emphasises the importance of removing these events, as they introduce an unnecessary error on the estimate of the probability-based magnitude of completeness.

5.4.4 Probability-based magnitude of completeness for Northern California – Our choice

We present maps showing separate aspects of the completeness of the Northern California Seismic Network (NCSN). They are calculated with the station configuration on 1 January 2011

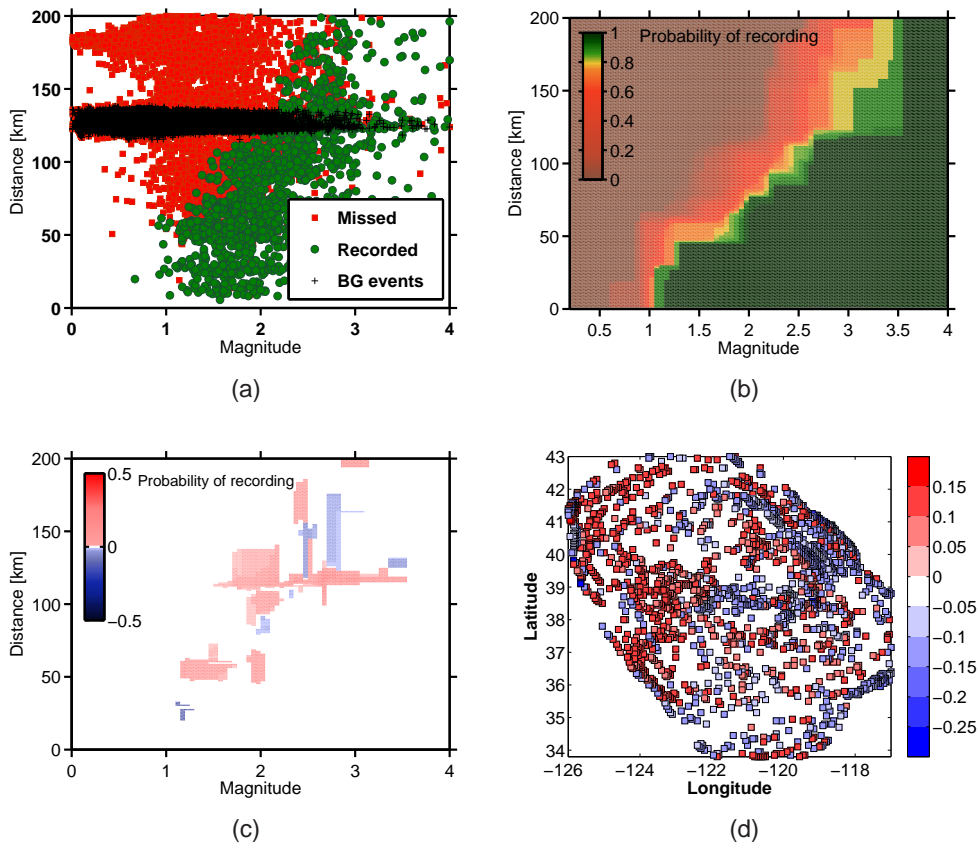


Figure 5.7: Illustration of the effect of an independent subnetwork, with the example of the station KIP. a) Recorded (green) and missed (red) events at this station with black crosses indicating data from the subnetwork BG. b) Resulting station detection probabilities P_D , when BG events are removed and c) difference in P_D . d) Nodes showing a difference $\Delta M_P \neq 0$ for $M_P(0.99, 0.001)$ based on all events and $M_P(0.99, 0.001)$ without the BG events.

with a total of 503 active stations. They represent a snapshot for this day as a different station configuration will lead to a different result. All maps are based on the threshold $p_t = 0.001$. We use the threshold $P = 0.99$ here; this is lower than previously used thresholds, it is a consequence of the NCSN policy to require 5 stations to trigger automatic locations.

First, we introduce the distribution of the probability-based magnitude of completeness M_p (P, \vec{x}, t) on a $P = 0.99$ probability level in Figure 5.8a. The probability-based magnitude of completeness, M_p varies from 0.3 to 3.9. It is highest at the network border regions, in offshore regions and in the north-western corner where the authoritative region overlaps with Oregon. There are three main regions with a significantly lower M_p : (1) along the San Andreas Fault, (2) the volcanic field north of Lake Tahoe and (3) the volcanic field at Mammoth Lakes. These regions have high station density is high with a station spacing of about 5 to 10 kilometres (compare Fig. 5.1). The station coverage in the Central Valley is comparatively worse which leads to a higher M_p in this region. The values of M_p range from 0.3 to about 1 in regions with a dense station coverage and from 1 to about 1.7 in region with a sparse coverage. Higher values of $M_p = 2$ and above are found outside the main station coverage.

Secondly, we introduce maps of detection probabilities $P_E(M, \vec{x}, t)$ for $M = 1$ and $M = 3$ in Figure 5.8b and c. These maps mark the probabilities with which each magnitude can be detected. The probability to detect an event with magnitude 1 reaches $P_E = 1$ in areas with a dense station coverage, among the San Andreas Fault and in the volcanic fields around Lake Tahoe and Mammoth Lakes. The probabilities are much smaller in the Central Valley and to the edges of the network. Probabilities to detect a M3 type event reach $P_E = 1$ for basically the whole authoritative region of the NCSN (outlined in black in Figure 5.8), with the exception of a small offshore region to the north.

Figure 5.8a, introduces the results for $p_t = 0.001$, however, we also calculated the results with $p_t = 0.01$ and $p_t = 0.1$. Table 5.2 lists the main differences to the calculation with all stations ($p_t = 0$) for $p_t = 0.1$, $p_t = 0.01$ and $p_t = 0.001$. While the mean number of stations is significantly

CHAPTER 5. RELIABILITY OF THE PMC METHOD

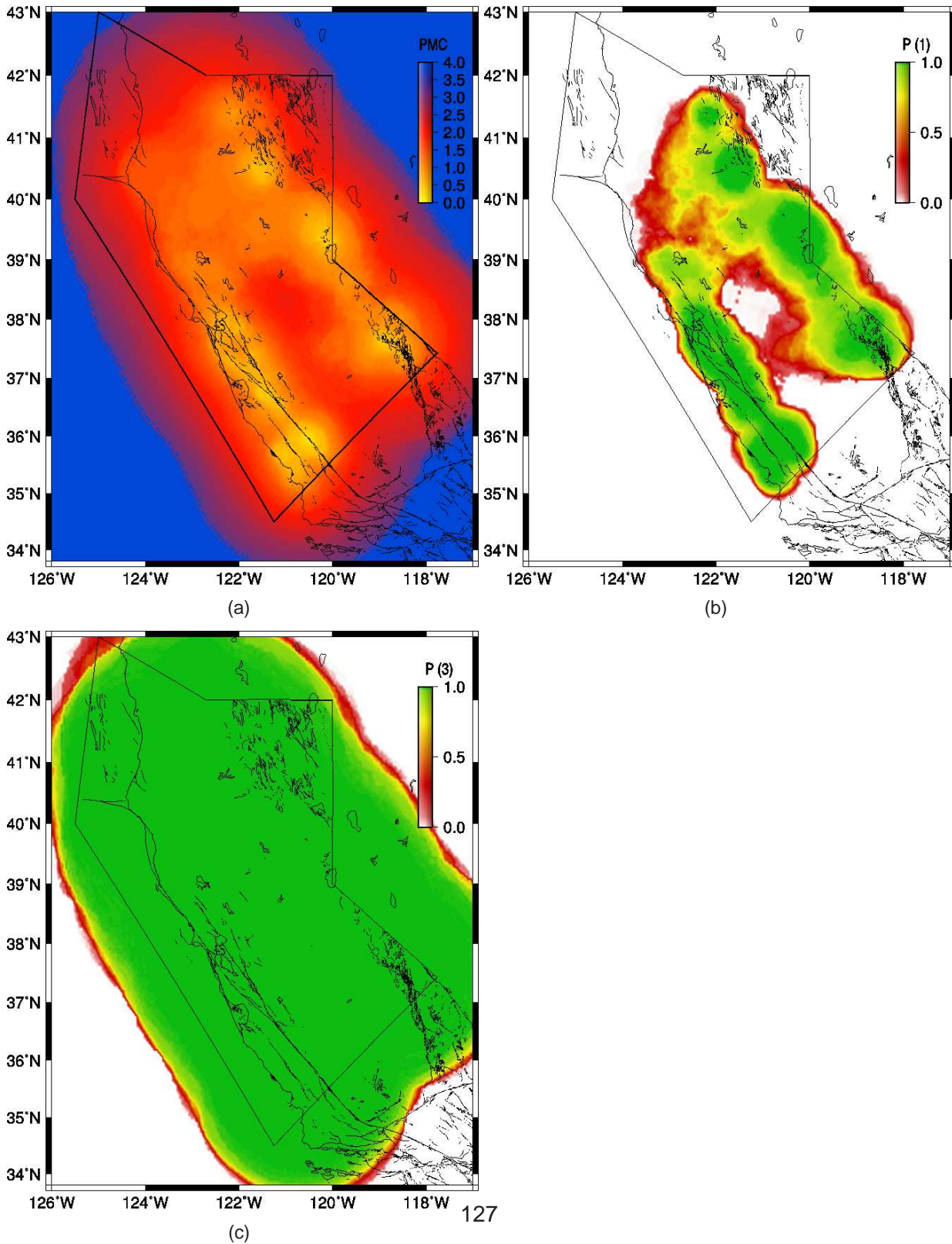


Figure 5.8: a) Map of $M_P(0.99, 0.001)$, b) Map of $P_E(M = 1, 0.001)$ and c) Map of $P_E(M = 3, 0.001)$. All three maps are calculated based on the station configuration on 1 January 2011.

decreased for all thresholds, the difference ΔM_p only changes significantly for $p_t = 0.1$ and $p_t = 0.01$, but not for $p_t = 0.001$. We see that the value of p_t has to be small in comparison to P to obtain a stable result of the probability-based magnitude of completeness. In case p_t it is too small, no significant change in the station number may be achieved, implying that the calculation time will not be reduced.

| p_t | ΔS | max ΔS | ΔM_p $\delta[5\%, 50\%, 95\%]$ | max ΔM_p | max S | max comb | mean S |
|-------|-------------|----------------|---|------------------|-------|--------------|-------------|
| 0 | - | - | - | - | 148 | $1.9 * 10^7$ | 42 ± 25 |
| 0.1 | 25 ± 27 | 141 | $[-0.9, -0.5, -0.2]$ | -1.4 | 10 | 386 | 5 ± 3 |
| 0.01 | 36 ± 25 | 136 | $[-0.4, -0.2, 0]$ | -0.7 | 15 | 1941 | 10 ± 1 |
| 0.001 | 28 ± 23 | 127 | $[-0.1, 0, 0]$ | -0.3 | 39 | $9.2 * 10^4$ | 19 ± 5 |

Table 5.2: Influence of the threshold p_t on the calculation of M_p , where S stands for number of stations and Δ marks the difference between the calculation with $p_t = 0$. The maximum number of stations determines the maximum possible combinations to determine the joint probability that five or more stations pick an event (compare Fig. 5.2).

5.5 Discussion and Conclusion

Besides the successful application of the PMC method to various seismic networks around the world, some of the basic ingredients of the method were so far not explored. We address important questions of the methodological design of the approach: How sensitive are probability-based magnitude of completeness results to spurious probability contributions from single stations? Can we define a threshold to cut these contributions objectively and what are the effects and the sensitivity to this cut-off. Furthermore we investigate how to deal with large seismicity clusters recorded by various subnetworks of a combined network such as the NCSN and show the effects on the final M_p values. Finally we provide an estimate of the current detection probabilities of the NCSN network for $M_p(P = 0.99, p_t = 0.001)$ based on which we argue

that the NCSN does not miss any M=3 type event within its authoritative region.

The major implication of this study is that not knowing the true completeness magnitude M_P , PMC does not provide any means to optimise for a best value set of the two parameters that have to be defined for a search of the completeness magnitude: the probability threshold P and the station cut-off threshold p_t . As described, both parameters remain in a common stress field and result in some trade-off depending on their choice (Figure 5.6). It is essential to state these values in future applications of the method and provide the reasons for their choice. We provide the methodological improvement to make the choice and to do the computation using the new sorting approach of the station detection probabilities P_D .

Earlier PMC results have not included this approach as these have used constant distance cut-offs (Schorlemmer & Woessner, 2008; Schorlemmer et al., 2010). The importance of our findings here needs to be analysed for these networks. However, not all studies will be affected in the same way, as the network configuration, the single station performances and the number of stations are contributing to the entire picture in a complex combination. We remain optimistic that the overall values provided are realistic, yet may be revised by future analyses. The threshold p_t has to be defined in relation to the threshold P . For Northern California, we choose $p_t = 0.001$ and $P = 0.99$ and as approximation we recommend $p_t < 1 - P$ for future studies.

The data analysis including the subnetworks of the NCSN leads us to conclude that strong clusters and data from subnetworks that are not part of the general triggering policy of the larger network should not be included in the preparation of the station detection probability matrices P_D (Figure 5.7). Strong overestimation of the detection capabilities may result when including such data and should therefore be disregarded, a process that in general is relatively easy to achieve with good expertise on the given seismicity. Essentially strong aftershock sequences and swarms should be removed since the temporal resolution of PMC works on the large network scale.

5.6 Data and Resources

Station data are taken from <http://www.ncedc.org/ncedc/station.info.html>. We use all stations that were in operation between 1 January 2008 to 1 January 2011. Phase data for the same period are taken from <http://www.ncedc.org/ncedc/catalog-search.html>. The format is described by Klein (2006).

References

- Amorese, D., 2007. Applying a change-point detection method on frequency-magnitude distributions, *Bull. Seismol. Soc. Am.*, **97**(5), 1742–1749.
- Eaton, J., 1992. Determination of amplitude and duration magnitudes and site residuals from short-period seismographs in Northern California, *Bull. Seismol. Soc. Am.*, **83**(2), 533–579.
- Gentili, S., Sukan, M., Peruzza, L., & Schorlemmer, D., 2011. Probabilistic completeness assessment of the past 30 years of seismic monitoring in northeastern Italy, *Phys. Earth Planet. In.*, **186**, 81–96.
- Gutenberg, B. & Richter, C. F., 1942. Earthquake magnitude intensity, energy, and acceleration, *Bull. Seismol. Soc. Am.*, **32**, 163–191.
- Klein, F., 2006. Y2000 shadow format and NCSN data codes, Available online at: <http://www.ncedc.org/ftp/pub/doc/ncsn/shadow2000.pdf>.
- Mignan, A., Werner, M. J., Wiemer, S., Chen, C.-C., & Wu, Y.-M., 2011. Bayesian Estimation of the Spatially Varying Completeness Magnitude of Earthquake Catalogs, *Bull. Seismol. Soc. Am.*, **101**(3), 1371–1385.
- Nanjo, K. Z., Tsuruoka, H., Hirata, N., Ishigaki, Y., & Schorlemmer, D., 2008. Initial report on the completeness magnitude for Japan: A GR-based application to the JMA catalog data (abstract), *Statsei 6 Meeting, 2008 Tahoe City*.
- Nanjo, K. Z., Schorlemmer, D., Woessner, J., Wiemer, S., & Giardini, D., 2010. Earthquake detection capability of the Swiss seismic network, *Geophys. J. Int.*, **181**(3), 1713–1724.
- Plenkens, K., Schorlemmer, D., Kwiatek, G., & the JAGUARS Group, in revision. On the probability of detecting picoseismicity, *Bull. Seismol. Soc. Am.*.
- Schorlemmer, D., 2009. Probabilistic seismic network completeness: Theory, application, and results (abstract), *Seismol. Res. Letts.*, **80**(2), 298.
- Schorlemmer, D. & Woessner, J., 2008. Probabilistic magnitude of completeness, *Bull. Seismol. Soc. Am.*, **98**, 2103–2117.

REFERENCES

- Schorlemmer, D., Mele, F., & Marzocchi, W., 2010. A completeness analysis of the National Seismic Network of Italy, *J. Geophys. Res. - Solid Earth*, **115**.
- Wang, Y., Husen, S., & Woessner, J., 2010. Assessing location uncertainties in non-linear probabilistic earthquake location, *Bull. Seismol. Soc. Am.*, **in prep**.
- Wiemer, S. & Wyss, M., 2000. Minimum magnitude of complete reporting in earthquake catalogs: examples from Alaska, the Western United States, and Japan, *Bull. Seismol. Soc. Am.*, **90**, 859–869.
- Wiemer, S., Giardini, D., Fäh, D., Deichmann, N., & Sellami, S., 2009. Probabilistic seismic hazard assessment for Switzerland: best estimates and uncertainties, *J. of Seismology*, **13**(4), 449–478.
- Woessner, J. & Wiemer, S., 2005. Assessing the quality of earthquake catalogs: Estimating the magnitude of completeness and its uncertainties, *Bull. Seismol. Soc. Am.*, **95**(2).

Chapter 6

Conclusions

The main goals of this thesis are (1) to introduce Induced Seismicity Hazard Assessment (ISHA), a time-varying seismic hazard associated with human activity, (2) to introduce a real-time probability-based alarm system for Enhanced Geothermal Systems, (3) to better understand the ongoing processes during fluid injections in the underground and (4) to improve the reliability of the probability-based magnitude of completeness estimation introduced by Schorlemmer & Woessner (2008). While the data is analysed on a small scale of less than 2km for the first three objectives, the fourth study concentrates on data from an entire seismic network, spanning several hundreds of kilometres. All four objectives have in common that I apply a combination of novel and standard approaches for statistical seismology.

The statistical analysis of seismicity associated with fluid injections can be performed using the same procedures as for naturally occurring seismicity. Models that describe aftershock sequences can be adapted to the setting of induced seismicity and be used to develop a real-time approach to forecast the ongoing seismicity (Chapter 2). A new focus-centred mapping technique allows analysis of the small-scale spatial distribution of the b -value of the Gutenberg-

Richter frequency–magnitude distribution. With a model that links the pore pressure evolution with the observed event-size distribution, the observed b -value patterns can be related to the applied pore pressure (Chapter 3). I introduce these concepts based on the seismic sequence of an EGS in Basel, Switzerland (Chapters 2 and 3) and confirm their general validity with a sequence from Soultz-sous-Forêts, France (Chapter 4) .

To analyse the probability-based magnitude of completeness method (PMC), introduced by Schorlemmer & Woessner (2008), I examine two aspects that influence the completeness estimate: (1) spurious probabilities from single stations and (2) independent subnetworks (Chapter 5). Using the Northern Californian Seismic Network as an example, I analyse various combinations of model parameters and introduce a map of the probability-based completeness estimate based on my choice of parameters.

6.1 Summary of Results

6.1.1 Statistical analysis of fluid induced seismicity

Chapters 2 to 4 analyse the seismic sequences induced by two EGS projects in Basel, Switzerland in 2006 and Soultz-sous-Forêts (SSF), France in 1993. For both sequences, I determine the spatio-temporal variations of the Gutenberg-Richter parameter b and the magnitude of completeness M_c . The values of the recording completeness vary for both sequences; $M_c(\text{Basel}) = 0.5 - 0.9$ and $M_c(\text{SSF}) = -1.7 - -1$. This would appear to imply that the data in Basel is much less complete; however, the magnitude definitions of both sequences are significantly different. This precludes a direct comparison of M_c values. A recent study by Bethmann et al. (2011) indicates that the scatter between M_L and M_w is relatively large for small magnitudes and that the conversion from one magnitude to the other is not linear. Using the conversion of the Swiss

Seismological Service (2011), I obtain values of $ML_c(\text{Basel}) = -0.8 - -0.1$, which are closer to the range of the SSF sequence. A consistent magnitude definition is crucial if the hazard estimation from one region has to be compared to the estimation for another region.

Similar to the completeness estimates, the absolute values of b are different for both sequences, while the values for the Basel sequence range from $b(\text{Basel}) = 0.8 - 3$, the values for SSF vary between $b(\text{SSF}) = 0.5 - 2$. In spite of this, the b -value distributions at both sites show similar spatio-temporal behaviour: high b - values are 1) associated with fluid injections and 2) found close to the openhole section, lower values are found 1) later into the sequence, and 2) further away from the injection point. Chapter 3 introduces a model that simulates the propagating pore pressure front and incorporates the event-size distribution via the modelled differential stress. The fact that this model is able to capture the observed spatiotemporal b -value distribution shows that changes in b can be explained with relative changes in the pore pressure. While high pressures – close to the injection points – induce events of all sizes, small events are especially common and thus higher b -values are observed. Further away from the borehole, changes of the pore pressure are only moderate and thus events in the range of the naturally occurring event sizes are observed, with b -values close to the regional average.

The implication of these findings on the probabilities for an event with a larger magnitude are that they increase with increasing distance from the injection point, as the stimulated volume increases and the b -value decreases. The model does not exclude the occurrence of a large magnitude event close to the injection point and early into the sequence – the probability for this, however, is small.

By analysing the statistical parameters of the Basel and the SSF sequences, I find that the decay of these sequences behaves similarly as natural seismicity, and can be described by the modified Omori-Utsu law (Ogata, 1999; Utsu, 1961). The time of the mainshock is assumed to be equivalent to the termination of the fluid injection. While the decay of the SSF sequence was

interrupted by new injections in the following months (and years), I find a time of 31 +29/-14 years for the Basel sequence until the seismicity reaches the background rate for magnitudes $M \geq 0.9$.

In both experiments the ongoing seismicity is monitored by a dense borehole network and alarm systems were used to determine the action if large events were recorded. The EGS in Basel used the so-called traffic light system, introduced first for the Berlin geothermal project in El Salvador by Bommer et al. (2006). This system was based on three components: 1) Public response, 2) observed local magnitude and 3) peak ground velocity (PGV). It had four possible stages where the injection rates would either be 1) continued as planned (green), 2) continued but not increased (yellow), 3) stopped and bleed-off stimulation pressure started (orange) or 4) stopped and bleed-off to minimum wellhead pressure started (red), where bleed-off involves actively pumping water out of the borehole (Håring et al., 2008). The aim of my study was to define a more quantitative alternative to this alarm system. For this I used two models that were originally introduced to model aftershock sequences (Chapter 2) and one model that was introduced to describe induced seismicity (Chapter 4). To test the validity of these models, standard procedures are used that were presented within the Collaboratory for the Study of Earthquake Predictability (CSEP, <http://www.cseptesting.org/>) framework. Either the best-fitting model, or a combination of all well-suited models can then be used to forecast the seismicity in real-time. Such a system has several advantages over a traffic-light type system as the whole magnitude range, rather than isolated events above a certain magnitude, is used to forecast seismicity. In addition, the system produces hazard estimates that can easily be implemented in the decision making process. An important part of the models is also that the fluid injection rate is incorporated, such that they allow calculation of scenarios for different pumping regimes.

6.1.2 Analysis of the probability-based magnitude of completeness method

The magnitude of completeness is an important input in any analysis of an earthquake catalogue. Schorlemmer & Woessner (2008) introduced a novel approach for determining the completeness based on the performance of the seismic stations and determining a probability-based completeness estimate. I introduce two additional steps in the synthesis of the probability-based magnitude of completeness (PMC).

First, I emphasise the importance of an in-depth analysis of the network and its subnetworks prior to the analysis of the data. Independent subnetworks that feed data into the seismic catalogue without matching the triggering conditions of the main network should not be included in the analysis of the PMC. I show that leaving such data in the catalogue substantially influences the completeness estimates, with single nodes showing differences of up to 20% in the probability-based completeness M_P . As basic knowledge about the seismic network is generally required for the PMC analysis, it should be feasible in future work to detect independent subnetworks and isolate their data.

Second, I analyse the sensitivity of the method to spurious probability contributions from single stations. To limit the number of stations involved in the completeness estimate, a cut-off criterion is introduced. This threshold p_t stipulates the minimum contribution of a station to the probability of detecting an event, $P_E(M, \vec{x}, t)$. This excludes stations with negligible detection probabilities. The choice of p_t is correlated to the choice of the probability level P at which the completeness estimates is determined. However, as the true value of the completeness magnitude M_P is not known for any network, it is impossible to optimise the PMC method – and thus the choice of p_t and P – towards this value. Thus I determine the sensitivity of the completeness estimate to the choice of p_t and P and argue for the choice I make for this study.

I present three different maps for the Northern Californian Seismic Network (NCSN), based on

the parameters of my choice: 1) a map of the probability-based magnitude of completeness, 2) a map of the detection probability P_E for magnitude 1 and 3) for magnitude 3. I conclude that the completeness is spatially highly variable and is lowest in regions with the densest station coverage. No events with magnitudes 3 should be missed in the authoritative region of the NCSN.

6.2 Future Perspectives

One limitation of this thesis is that so far only three different kind of models have been analysed with the data of two induced seismic sequences. These models only cover the stimulation phase of EGS projects; it remains to be solved how to assess the hazard during the operational and the post-operational phase. For future Induced Seismic Hazard Assessment (ISHA), it is crucial to integrate more models and test them in a pseudo-prospective way on additional sequences. For a probability-based alarm system, a compound model must be built, using Akaike weights (e.g. Gerstenberger et al., 2005) for each model. Thresholds for the forecast probability of exceeding EMS levels must be decided on beforehand, by the operators of an EGS experiment and by the regulatory bodies. Only then can a probability-based alarm system be used in a future EGS project.

The models introduced in this study only forecast temporal changes in the seismicity. In Chapter 3, it is indicated that the spatial distribution of b -values can be used to determine the location of large magnitude events. The goal therefore has to be to construct a model that involves both spatial and temporal evolution of the seismicity.

In this study, there is no distinction between induced and triggered seismicity, where induced seismicity occurs within the stimulated rock mass and triggered seismicity occurs on previously critically stressed nearby-faults. Neither of the models implies any knowledge of the regional fault structures, and thus the potential of triggering an event on such faults is neither included nor

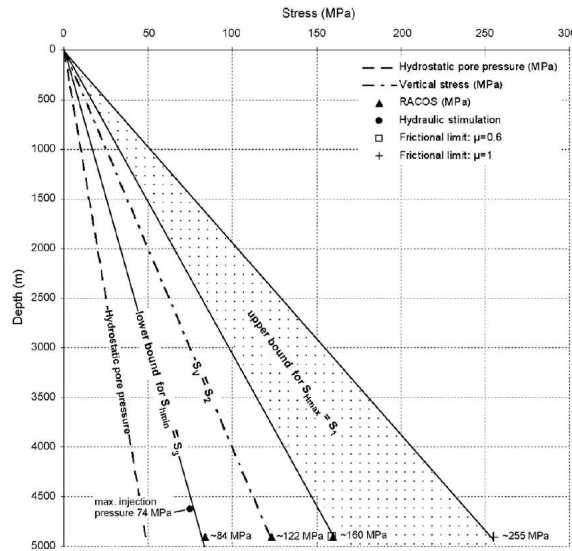
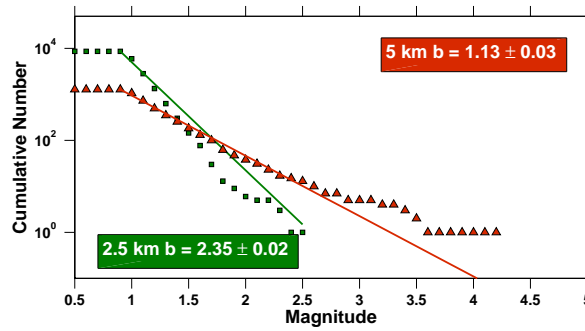


Figure 6.1: Constraints on the minimal and maximum horizontal stress values, determined by Häring et al. (2008).

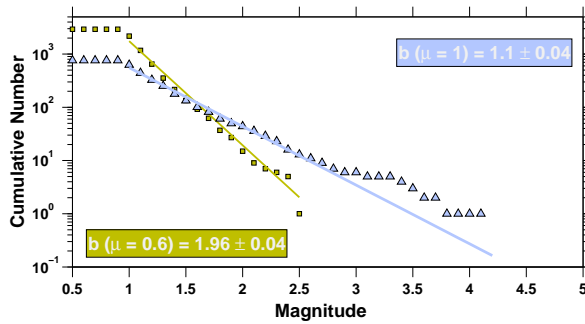
excluded specifically. All models rely on the recorded seismicity alone. A model that incorporates basic knowledge of the geological structures should be incorporated within the compound model, and its performance relative to the standard model tested.

The model presented in Chapter 3 is calculated for the setting for the Basel sequences where: 1) the pore pressure diffusion follows the model by Dinske & Shapiro (2010), 2) the bounds of the minimal and the maximum horizontal stress σ_1 and σ_3 are representing an intermediate crust, with the values determined by Häring et al. (2008), 3) the coefficient of friction μ is that of an intermediate crust and 4) 300,000 seed faults are used.

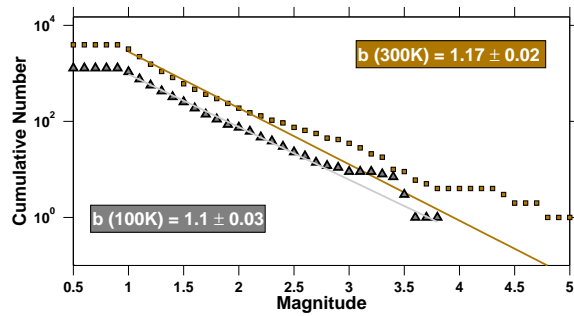
Changing any of these setting will influence the outcome of the simulation. This allows for future applications of the model to simulate various crustal settings. The bounds of σ_1 and σ_3 are a function of the depth (Figure 6.1), thus narrower bounds are found in shallower depths. Model simulations where σ_1 and σ_3 both have been reduced by 50% – i.e. the simulation has been moved to around 2,500m depth (Figure 6.1) – indicate a significant increase of the number of triggered seed faults and in the overall b -value (Figure 6.2a). Changing the coefficient of friction



(a)



(b)



(c)

Figure 6.2: a) Frequency–magnitude distribution for 5 km depth (red) and 2.5 km depth (green); the activity is higher in lower depths, so is the observed b -value for the overall simulated sequence. b) FMD for $\mu = 1$ (light blue) and $\mu = 0.6$ (light green); the activity and the b -value is significantly higher for lower values of μ . c) FMD for 300,000 seed faults (brown) and 100,000 seed faults; while the b -value does not change, the activity is significantly higher with a larger number of seed faults. While (a) is based on 300,000 seed faults, (b) is based on only 100,000.

μ in the simulation also significantly influences the number of triggered events, increasing μ – i.e. increasing the rock strength – reduces the number of triggered events and vice versa (Figure 6.2b). These two findings have to be evaluated further as they indicate that various geological setting will lead to a different number of induced events, which is an important indication for the choice of the location for future EGS projects.

While the model in Chapter 3 only presents the simulation based on the pore pressure diffusion by Dinske & Shapiro (2010), the influence of different pumping regimes on the number of triggered events, remains to be tested. The number of seed faults directly correlates with the number of triggered events and can thus be used to scale the model to match the observed seismicity (Figure 6.2c) . Additionally, the minimalistic model can be further improved by extending it to a three dimensional simulation.

For future applications of the PMC method, it is important to analyse the networks beforehand and exclude any data from independent subnetworks. As the method has already been applied to several networks worldwide, e.g. Southern California (Schorlemmer & Woessner, 2008), Japan (Nanjo et al., 2008), Switzerland (Nanjo et al., 2010) or Italy Schorlemmer et al. (2010), it has to be analysed if such subnetworks might have had an influence on their results.

For future applications, a careful choice of the probability threshold P and cut-off threshold p_t is required. In this study I conclude that a choice of $p_t < 1 - P$ is most stable. However, the sensitivity of the completeness estimate M_P to these parameters has to be analysed over several networks before this can be established.

References

- Bethmann, F., Deichmann, N., & Mai, P. M., 2011. Scaling Relations of Local Magnitude versus Moment Magnitude for Sequences of Similar Earthquakes in Switzerland, *Bull. Seismol. Soc. Am.*, **101**(2), 515–534.
- Bommer, J. J., Oates, S., Cepeda, J. M., Lindholm, C., Bird, J., Torres, R., Marroquin, G., & Rivas, J., 2006. Control of hazard due to seismicity induced by a hot fractured rock geothermal project, *Engineering Geology*, **83**(4), 287–306.
- Dinske, C. & Shapiro, S., 2010. Interpretation of microseismicity induced by time-dependent injection pressure, *SEG Expanded Abstracts*, pp. 2125–2129.
- Gerstenberger, M. C., Wiemer, S., Jones, L. M., & Reasenber, P. A., 2005. Real-time forecasts of tomorrow's earthquakes in California, *Nature*, **435**(7040), 328–331.
- Häring, M. O., Schanz, U., Ladner, F., & Dyer, B. C., 2008. Characterisation of the Basel 1 enhanced geothermal system, *Geothermics*, **37**(5), 469–495.
- Nanjo, K. Z., Tsuruoka, H., Hirata, N., Ishigaki, Y., & Schorlemmer, D., 2008. Initial report on the completeness magnitude for japan: A GR-based application to the JMA catalog data (abstract), *Statsei 6 Meeting, 2008 Tahoe City*.
- Nanjo, K. Z., Schorlemmer, D., Woessner, J., Wiemer, S., & Giardini, D., 2010. Earthquake detection capability of the swiss seismic network, *Geophys. J. Int.*, **181**(3), 1713–1724.
- Ogata, Y., 1999. Seismicity analysis through point-process modeling: a review, *Pure appl. geophys.*, **155**, 471–507.
- Schorlemmer, D. & Woessner, J., 2008. Probabilistic magnitude of completeness, *Bull. Seismol. Soc. Am.*, **98**, 2103–2117.
- Schorlemmer, D., Mele, F., & Marzocchi, W., 2010. A completeness analysis of the National Seismic Network of Italy, *J. Geophys. Res. - Solid Earth*, **115**.

REFERENCES

Swiss Seismological Service, S., 2011. Earthquake Catalogue of Switzerland – Release 201, Tech. rep., ETH Zurich.

Utsu, T., 1961. A statistical study of the occurrence of aftershocks, *Geophys. Mag.*, **3**, 521–605.

List of Tables

| | | |
|-----|--|-----|
| 2.1 | Summary of the models and updating strategies used in the study. Model names are used in the text, the type indicates the base model. Main differing assumptions are indicated together with fixed / initial parameter values and free parameter values estimated from the sequence. | 39 |
| 2.2 | Quantitative evaluation of model forecasts: Model name, model type, fraction of rejected time bin in N-Test, fraction of rejected time bins in L-Test, and joint log-likelihood of the each model. | 43 |
| 4.1 | Quantitative evaluation of model forecasts: Model name, model type, fraction of rejected time bin in N-Test, fraction of rejected time bins in L-Test, and joint log-likelihood of the each model. The joint log likelihoods in the brackets indicate the corrected values, where bins containing no data are excluded. | 99 |
| 5.1 | Networks of the Northern California Seismic Network that we used in this analysis. The third column indicates the number of stations that were in operation on 1 January 2011 and that recorded at least one event during our study period. In brackets we report the number of stations that were in operation during the study period from 1 January 2008 to 1 January 2011 and that recorded at least one event. Detailed information about the networks is available online at http://www.ncedc.org/ncedc/station.info.html | 113 |
| 5.2 | Influence of the threshold p_t on the calculation of M_p , where S stands for number of stations and Δ marks the difference between the calculation with $p_t = 0$. The maximum number of stations determines the maximum possible combinations to determine the joint probability that five or more stations pick an event (compare Fig. 5.2). | 128 |

List of Figures

| | | |
|-----|--|----|
| 1.1 | Schematic figure explaining the EGS principle. 1) reservoir, 2) pump house, 3) heat exchanger, 4) turbine hall, 5) production well, 6) injection well, 7) heated water for district heating, 8) porous sediments, 9) observation well and 10) crystalline bedrock. ©M. Haering, Geothermal Explorers Ltd, 2007 | 3 |
| 1.2 | Seismicity rates, wellhead pressure and injection rate for a) Basel in 2006 and b) Soultz-sous-Forêts in 1993. The earthquakes are clearly driven by the injection, they start when the injection is started and decay rapidly after no additional fluid is injected. | 5 |
| 1.3 | Overview of the Basel site. The locations of the borehole and the seismic network are indicated. The grey shading indicates the population density. | 7 |
| 1.4 | a) Overview of the Soultz-sous-Forêts site with the closest cities. The site lies within the upper Rhine graben. b) Overview over boreholes in Soultz-sous-Forêts and the measured seismicity associated with injections into these boreholes. While EPS1 is fully cased, injection test were conducted at different depths for GPK 1 – 4. The numbered boreholes refer to abandoned boreholes within which the seismic network was installed. Figure taken from Cuenot et al. (2008). | 8 |
| 1.5 | Probability of exceeding of EMS intensities, according to the Serianex Risk study (Baisch et al., 2009), for a) a 12 day injection period and b) a 30 years operation period. These hazard estimates only present snapshots and are based on average seismicity rates, determined after the termination of the project. ©Serianex | 10 |
| 2.1 | Overview of the study region with all seismic stations. Different symbols show borehole and strong motion stations maintained by either Geothermal Explorers or the Swiss Seismological Service. The inset indicates the location of all seismic stations in Switzerland with the high density of stations around Basel | 22 |

LIST OF FIGURES

2.2 Distribution of the events in plane view (top left) and as depth distributions (EW lower panel and NS right panel). Circle sizes are scaled by magnitude; events with magnitudes above 3 are highlighted with darker colours. Events in black occurred during the injection and events in grey after water injection was terminated. The borehole is indicated; the darker part is cased and the lighter part is open. 24

2.3 Completeness and time evolution of the (a) whole catalogue and the (b) first ten days. The black solid line indicates the variation of the completeness of this catalogue over time; it varies the most during the first days and then becomes constant. We did not determine the completeness after June 2007, as the seismicity becomes too sparse. 29

2.4 Gutenberg-Richter frequency–magnitude relation for two different sequences. Darker triangles show events during the injection, lighter squares mark events after the termination of water injection. Gutenberg-Richter parameters are indicated for each sequence. 31

2.5 Decay of the sequence after the termination of the water injection. A modified Omori-Utsu law is fitted to the sequence to determine its duration; circles represent the data. We only fit the first 200 days of data (dark circles); events after this time (grey circles) fall within the uncertainty. The background of this region and the uncertainty are indicated at the bottom of the figure. Where they intercept with the model, we find the duration of the sequence. The black box indicates the uncertainty and the black star the best fit. We find a duration of $31 +29/-14$ years. 32

2.6 Summary of all eight models; (a) three models based on the Reasenberg & Jones approach, (b) two models based on ETAS approach without flow rate and (c) three models based on ETAS approach with flow rate. In all three panels, the observed rates within the next six hours is indicated with a bold black line and circles. The time of the shut in and the two largest events that led to actions within the traffic light system are indicated. 34

2.7 Log-likelihood values of the L-test for model E5 as a function of time. The panels display the mean and the 97.5 and 2.5 percentiles (grey dot and bars); days on which a log-likelihood value $LLS(t)$ is accepted are indicated with black squares; if the model is rejected, we indicate this with grey squares. 41

2.8 Probabilities for events within the next six hours for magnitudes \geq to 2, 3 and 4 with time, based on model E5. Observed events above magnitude 2 are indicated in the lower panel. 44

LIST OF FIGURES

2.9 Hazard curves based on model E5. (a) Probabilities of exceeding EMS Intensities I to X for three different times, (1) day three, (2) day six and (3) day twelve after the start of water injection. All three curves are based on $M_{max} = 5$. (b) Probabilities of exceeding EMS intensities III, IV and V within the next six hours for the first 15 days. Indicated are also the times of the two largest events during the first 15 days and the time of the termination of water injection. 45

2.10 (a) Effect of different maximum magnitudes with (1) $M_{max} = 3.7$, (2) $M_{max} = 5$ and (3) $M_{max} = 7$. Higher probabilities show the probabilities of exceeding EMS intensity III, lower probabilities the exceedance probabilities for EMS V. The inset marks a hazard snapshot for day three (indicated by a light grey dashed line). (b) Effect of different b -values on the hazard integration with (1) $b = 0.9$, (2) $b = 1$ and (3) $b = 1.58$ for co-injection and 1.15 for post-injection events. The inset shows again a hazard snapshot for day three. 52

3.1 **Overview:** a) Overview of the experiment showing the depth (a.s.l.) of the events (circles) and the location of the seismic stations (triangles). The red plane marks the top of the crystalline basement, within which all events occurred. The color-scale indicates the recording completeness ranging from M_c 0.7 to 1. b) Close-up of the events with the overall b -value distribution. While values range from 0.8 to 3, the colorbar is limited from 1 to 2 for a clearer visibility. 64

3.2 **Time Evolution:** a) Radial distance vs from the injection point. The inset marks the frequency-magnitude distribution of the co- and post-injection period separately. The values are $b_{co} = 1.57 \pm 0.06$ (brown) and $b_{post} = 1.14 \pm 0.06$ (green). b) Equivalent figure for the simulated events, we find $b_{mco} = 1.30 \pm 0.02$ (brown) and $b_{mpost} = 1.08 \pm 0.06$. The contours represent the pressure based on a linear diffusion model and linearly increasing wellhead pressure(Dinske & Shapiro, 2010). 66

3.3 **b -value Distribution:** a) and b), cross section along the N-S axis, with b -value distribution based on co-injection and post-injection events, c) Frequency–magnitude distribution for two sampled areas with a high b -value of 2.93 ± 0.40 (red) and a low b -value of 0.83 ± 0.1 (blue). d) to f) Equivalent plots to a) to c) with the simulated events. The sample volumes in f) show b -values of 2.31 ± 0.30 (red) and 1.00 ± 0.10 (blue). The b -values range from 1 to 2 in all subplots. 68

3.4 **Time and Distance:** b -values against radial distance from the injection point for a) observed events and b) simulated events. The b -value decays with distance from the injection point starting around 200 m for the data and the simulated events. Events are separated in co- and post-injection periods (brown and green, respectively). 69

LIST OF FIGURES

3.5 **Figure 3.5: Model:** a) Mohr-Coulomb plot for the 2D model. Points denote the points closes to failure for all 300,000 seed faults. Increasing the pore pressure (ΔP) shifts the potential seed to the left; an event is triggered if the Mohr-Coulomb circle (dashed black circle) touches the failure envelope. The arrow indicates the minimum pore pressure change needed to trigger a seed fault. The b -value and the differential stress σ_D are inversely correlated, leading to an event-size for each seed fault drawn from a power-law with the respective b -value. b) Result of one simulation of the model, a total of 3,921 seed faults were triggered. The b -values for events triggered with high ΔP (green rectangle) and low ΔP (red rectangle) are significantly different, $b_{highP} = 1.33 \pm 0.03$ (green) and $b_{lowP} = 1.08 \pm 0.02$ (red) (indicated by the FMD inset). c) and d) equivalent plots for a narrower stress range at a shallower depth where only 532 events with a high overall b -value of 2.46 ± 0.1 are triggered. 71

3.6 **Figure 3.6: Probability for Large Magnitude Events:** Occurrence probability of M 4 event, varying with a) time and b) radial distance from the injection point for a varying b -value (white) and a constant b -value (gray). The errorbar denotes the standard deviation based on 100 simulations of the geomechanical model. The dashed line in a) marks the shut-in time and in b) the location of the largest observed Basel event. 75

4.1 Overview of the geological setting of Soultz-Sous-Forêts site. The site lies within the Upper Rhine graben. The cross-section marks the granite (cross-pattern, dark grey in plan view), Mesozoic sediments (light grey) and the Oligocene and Miocene sediments (white). Figure taken from Evans et al. (2005) 83

4.2 Map showing the region of the Soultz-Sous-Forêts Site with the closest settlements. GPK1, EPS1 and GPK2 denote three wells. the numbered wells are abandoned oil wells, hosting the seismic network. Figure taken from Evans et al. (2005) 85

4.3 Injection rate, wellhead pressure and observed seismicity rate during the 1993 injection test at the SSF site. The colours of the seismicity correspond to the six different stages of the seismicity associated with the six different co-injection and post-injection periods (compare Figure 4.4). Holes in the seismicity rate indicate three different periods (4.75d, 9.2d and 10d) where no data was recorded due to technical difficulties. 86

LIST OF FIGURES

4.4 Illustration of the seismicity during the six different stages. a) First injection in the open hole section from 2850 to 3400m, during first 15 days, b) decay after the first injection from 15 days up to 29 days, c) injection into a fracture zone at 3485 depth for two days, during which the borehole was sealed with a double-packer above and below 3845 m depth d) decay after the double-packer injection from 32 up to 39 days, e) third large scale injection from 2850m down to the bottom of the borehole at 3600m, f) decay after the last injection. The borehole is marked in black in all panels, the respective open hole sections in red. The colours of the seismicity corresponds to the colours in Figure 4.3. 87

4.5 Time versus distance for the two main injections and their post-injection events. For a) the distance against the casing shoe at 2850 m depth is measured, for b) the distance from the newly open part of the borehole at 3400m is measured. While there is a typical increase with distance for the first injection, the seismicity is concentrated in the previously unstimulated part for the third injection. The colours correspond to Figures 4.4 and 4.3 88

4.6 Statistical parameters of the seismic sequence with time for a) completeness magnitude and b) *b*-value with one standard deviation. 89

4.7 Frequency–magnitude distributions for four out of six stages (see Figure 4.4). While the first (blue) and the fifth (purple) stage are associated with fluid injections, the second (red) and the sixth (brown) stage show the decay after the two longterm injections. Values of *b* associated with fluid injections are substantially higher. 90

4.8 Three dimensional *b*-value distribution for four out of the six stages (see Figure 4.4). Stages 1 and 5 are associated with fluid injections, stages 2 and 6 show the decaying seismicity after the injections. Higher *b*-value are found during the injections, close to the openhole sections. Lower values are found further out, from the decaying sequences. The three dimensional distribution of stage 1 is shown in more detail in Figure 4.9. 91

4.9 Three dimensional *b*-value distribution of the first stage, divided into areas with $b \geq 1.2$ and $b \leq 0.9$, shown as cross section (a, b) and mapview (c, d). The cross sections highlight that higher *b*-values are found closer to the injection point and lower values further out. The mapview emphasises the extension of the areas with high, respectively low *b*-values. Lower *b*-values are found further out than higher values. 92

4.10 Comparison of the frequency–magnitude distribution (FMD) of the SSF and the Basel sequence. As the magnitude definitions are substantially different, a direct comparison between both FMDs is not possible. 93

LIST OF FIGURES

4.11 Decay after the two major injections; a) from 15.4 to 29.2 day and b) after 43.9 days. The decay between the first injection and the double packer injection (a) can not be fit with the modified Omori-Utsu law, however the decay after no additional injections follow (b) can be well fit with this law. 95

4.12 Modelling results of the SSF sequence for Shapiro’s model (pink) and the ETAS E5 model (green), the observed data is indicated in black. Technical difficulties led to data gaps at 4.75 and 10 days, which are shown as bins with 0 observed events. 98

4.13 Hazard curves based on model SR. Probabilities of exceeding EMS Intensities I to X for the maximum observed values for Basel (blue) and the Soultz-sous-Forêts sequence (red). 100

4.14 Evolution of seismogenic index Σ with time for a) Basel, b) the first injection in SSF and c) the third injection in SSF. The respective shut in is indicated in all three panels. The starting value is 0.5 for all three sequences. 101

5.1 Events recorded by the Northern Californian Seismic network (white circle, sizes are scaled by magnitude), stations are marked with yellow triangles. The inset (location marked in grey) indicates the stations of the independent subnetwork BG and the events recorded by this network. 114

5.2 Sum of binomial coefficients $C(n,k)$, where n is the number of involved stations and k is 0 to 3 for four station triggering and 0 to 4 for five station triggering. The difference in possible combinations for four stations and five stations triggering increases exponentially. 117

5.3 Increase of the probability to detect an event of magnitude M 1 and 2 with increasing station numbers: 1) sorted by distance (red) and 2) sorted by probabilities (green). The arrows indicate the increase in the combined probability Δp for two cases. 118

5.4 a) and b) Station detection probabilities P_E with distance for $M=1.5$ and $M=2.5$. The mean behaviour and one and two σ are indicated. c) One standard deviation σ of P_E for magnitude 0.5 to 3. d) and e) Example stations AFD and GZY, marked in blue and red in a and b. 120

5.5 Differences in $\Delta(M_P)$ for a) $M_P(0.99, 0) - M_P(0.99, 0.001)$, b) $M_P(0.99, 0.001) - M_P(0.99, 0.01)$ and c) $M_P(0.99, 0.01) - M_P(0.99, 0.1)$. Stars mark the location of the detailed analysis in Figure 5.6 122

5.6 Relation between P and p_t for four different locations, marked by stars in Figure 5.5. The colour bar denotes the difference relative to $M_P(0.9, 0)$. While two locations (a and b) show relatively low differences for all combinations of P, p_t , the differences in c and d reach values up to $1.2 \Delta M_P$ 123

LIST OF FIGURES

5.7 Illustration of the effect of an independent subnetwork, with the example of the station KIP. a) Recorded (green) and missed (red) events at this station with black crosses indicating data from the subnetwork BG. b) Resulting station detection probabilities P_D , when BG events are removed and c) difference in P_D . d) Nodes showing a difference $\Delta M_P \neq 0$ for $M_P(0.99, 0.001)$ based on all events and $M_P(0.99, 0.001)$ without the BG events. 125

5.8 a) Map of $M_P(0.99, 0.001)$, b) Map of $P_E(M = 1, 0.001)$ and c) Map of $P_E(M = 3, 0.001)$. All three maps are calculated based on the station configuration on 1 January 2011. 127

6.1 Constraints on the minimal and maximum horizontal stress values, determined by Häring et al. (2008). 139

6.2 a) Frequency–magnitude distribution for 5 km depth (red) and 2.5 km depth (green); the activity is higher in lower depths, so is the observed b -value for the overall simulated sequence. b) FMD for $\mu = 1$ (light blue) and $\mu = 0.6$ (light green); the activity and the b -value is significantly higher for lower values of μ . c) FMD for 300,000 seed faults (brown) and 100,000 seed faults; while the b -value does not change, the activity is significantly higher with a larger number of seed faults. While (a) is based on 300,000 seed faults, (b) is based on only 100,000. . . 140

Acknowledgements

First I would like to thank Stefan Wiemer for giving me the opportunity to work on this thesis. His constant enthusiasm was always very contagious and he supported me in many ways throughout this work. He provides an pleasant work environment in his group, where discussions are always encouraged, especially if they involve croissants. Many thanks also to Jochen Woessner for helping me solve many scientific challenges. He often gave me the input I needed and allowed me to see problems in a new light. I also want to thank Domenico Giardini for providing the scientific environment that so many people profit from. He is constantly working to assure that the Seismological Service of Switzerland and the Institute of Geophysics stay on top. Many thanks to Sebastian Hainzl and Danijel Schorlemmer for their collaborations and for giving me deeper insights into their codes. I enjoyed the time I spend in Potsdam with each of them.

Thanks go to the GEOTHERM group at ETH that allowed me to get to know new aspects of geothermal energy that I had not considered before. Many successful meetings involved very interesting discussions. I would also like to thank all the past and present members of the statistical seismology group, Annemarie, Arnaud, Banu, Bettina, Fabian, David, Georgia, Jeremy, Kazu, Marta, Matteo, Max, Men, Silvio, Stefan H., Thessa and Thomas. I profited a lot from all our scientific discussions and the several BBQ were always fun. Thanks to all the members of the institute, especially to the people without whom nothing would work in our Institute, André,

ACKNOWLEDGEMENTS

Elisabeth, Sabine and Monika. All the work you do is very appreciated.

Thanks to my changing office mates, Marta, Matteo, Julia, Julie, Steve, Thessa and Men for the often needed distraction from staring into the computer screen all day. Thanks to everybody at Friday beer; scientific discussions are always better with a beer in the hand – so are non-scientific discussions. Thanks to Michael for providing me with music and for giving me feedback about this thesis. Thanks to Valerio for interrupting my work and for reminding me to relax. Thanks to Janne, Jess, Marion and Steffi for all their (costume) parties. Thanks to Christoph, Anne and Jeff for accepting me as their quasi-flatmate. Thanks to Jonas for letting me beat him at boules. Thanks to all the people that made life at the institute so much more fun, Tobi, Sabrina, Pinar, Toni, Teo, Matt, Pietro, Olivier, Alice, Peter, Alain, Falko, Florian, Ingo, Thomas, Diana, Kees, Magali, Thibault, Dave(s), Illaria, Kerry, Asia, Ulrik, Ruth and Gabriel. I will miss you all once I leave (or I miss you already if you have left before me).

Thanks to my friends Joëlle, Nicole and Dony – Merci für alli feine Znacht, für super Cocktails, cooli Konzert und alli suschtigi schöni Öbig – ich hoffe natürlig uf villi meh. Thanks to my family for all the support over the years – ohni eu hetti das nöd chöne.

Last, but of course not least, a million thanks to Greg – you know that this would not have been possible without you.

Curriculum Vitae

PERSONAL INFORMATION:

Surname/First names: Bachmann Corinne Elisabeth
Address: Goldbrunnenstrasse 145, 8055 Zurich, Switzerland
E-mail: bachmann@sed.ethz.ch
Nationality: Swiss
Date of birth: 18.01.1982

EDUCATION:

1996-2001: Mathematisch - Naturwissenschaftliches Gymnasium Rämibüehl Zurich
2001-2007: ETH Zurich
2003: Vordiplom in Earth Science at ETH Zurich
2007: Master Thesis at ETH Zurich.
Thesis Title: Probabilistic Magnitude of Completeness of the Northern Californian seismic Network
2004-2005: Universiteit Utrecht, The Netherlands
2007-2011: Doctoral Student, Swiss Seismological Service, ETH Zurich, Switzerland.
Expected Degree: Doctor of Science